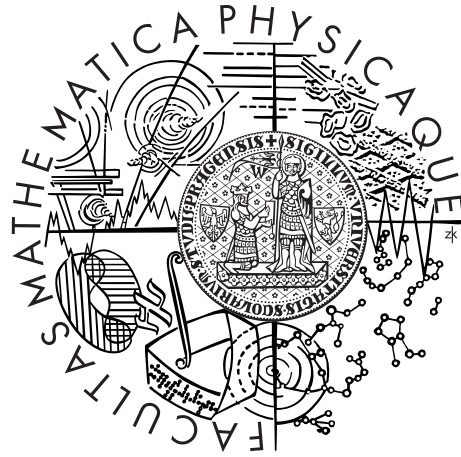Charles University in Prague

Faculty of Mathematics and Physics

MASTER THESIS

Michael Hakl

Study of electric field in radiation detectors by Pockels effect

Department of Material Research

Supervisor of the diploma thesis: Prof. Ing. Jan Franc, DrSc.

Study programme: Solid state physics

Specialization: Physics of real surfaces

Prague 2014

Acknowledgements

I would like to express my deepest gratitude to the thesis supervisor, Prof. Jan Franc, for his excellent guidance, endless patience, productive critics, sincere comments and personal attitude.

I heartily acknowledge colleague Dr. Václav Dědič who introduced me to the Pockels-effect measurements and taught me everything I know about the issue. The provided cooperation and training were important for me particularly in the beginning. I also appreciate his inspirative ideas and challenging suggestions. His advices and understanding were obviously above the required framework. I cannot imagine the elaboration of the thesis without his help.

I am grateful to Assoc. Prof. Pavel Hlídek for assistance during luminesce measurement and interpreting the data. His experience and abundant suggestions for improvement of Pockels experimental set-up and optical adjustment of the apparatus were invaluable.

Thanks belong to all of them for correction of my writing.

I am thankful to the fellowship of students Jakub Zázvorka, Martin Rejhon, Jakub Pekárek for providing a friendly atmosphere and especially to Lukáš Šedivý who conducted me throughout specimens preparation and characterization.

I am indebted to Jan Ulrych for time-consuming and laborious optical polishment of crystals, to Assoc. Prof. Roman Grill for theoretical explanations and recommendations and to Assoc. Prof. Stanislav Daniš for crystallographic orientation of specimens.

Finally, the author conveys thanks to the group of stuff in the Department of semiconductor physics and opto-electronics for their contribution, permission to use laboratory facilities and financial support funded by the project SVV-2010-265306 and GAČR 102/13-13671S.

This work is dedicated to the scientific and technical progress on the field of X-ray imaging and detection.

Honorable Declaration

I declare that I carried out this master thesis independently, and only with the cited sources, literature and other professional sources.

I understand that my work relates to the rights and obligations under the Act No. 121/2000 Coll., the Copyright Act, as amended, in particular the fact that the Charles University in Prague has the right to conclude a license agreement on the use of this work as a school work pursuant to Section 60 paragraph 1 of the Copyright Act.

In Prague 2014   signature of the author

Title: Study of electric field in radiation detectors by Pockels effect

Author: Michael Hakl

Department: Material Research

Supervisor: Prof. Ing. Jan Franc, DrSc. (franc@karlov.mff.cuni.cz)

Abstract: Cadmium Telluride (CdTe) is a convenient candidate for room temperature detection of X-ray and gama radiation due to 1.5 eV band-gap energy and high atomic mass. Since CdTe has the highest linear electro-optical coefficient among II-VI compounds, the detector represents a Pockels cell. Transmittance of the crystal is modulated by the internal electric field. Processing of infrared camera photographs results in an electric field profile between biasing electrodes. The electric field in semi-insulting CdTe is influenced with deep level traps causing charge polarization under the electrodes. Occupation of traps is dependent on metal-semiconductor interface. Relation of charge accumulation and band bending for gold and indium contacts was studied. Repolarization/depolarization induced by additional illumination with sub/above bandgap excitation laser was observed and exploited for determination of the deep level energy. Results obtained by the Pockels-effect method were supported with luminescence measurements. Correlation between the occurrence of deep levels and surface point defects was discovered.

Keywords: CdTe, Pockels effect, electric field, deep level, Schottky contact

Název práce: Studium elektrického pole v detektorech záření pomocí Pockelsova jevu

Autor: Michael Hakl

Katedra: Fyzika kondenzovaných látek a makromolekul

Vedoucí diplomové práce: Prof. Ing. Jan Franc, DrSc.

Abstrakt: Kadmium telurid (CdTe) se zdá být vhodným kandidátem pro detekci rentgenového a gamma záření za pokojové teploty díky gapové energii 1.5 eV a vysokému atomovému číslu. CdTe ve své podstatě představuje Pockelsovu celu, neboť vykazuje vysoký elektro-optický koeficient. Propustnost krystalu je modulována vnitřním elektrickým polem. Zpracováním obrázků pořízených IČ kamerou získáme profily elektrického pole rozprostřeného mezi elektrodami. Pole ve vysokoodporovém CdTe je ovlivněno pastmi položenými hluboko v zakázaném pásu, jež způsobují hromadění náboje v blízkosti elektrod. Obsazení těchto pastí je závislé na rozhraní mezi kovem a polovodičem. Vztah mezi polarizací detektoru a zahnutím pásu byl podroben studiu pro zlatý a indiový kontakt. Byla pozorována repolarizace resp. depolarizace pole po osvětlení podgapovým a nadgapovým excitačním laserem. Tento efekt byl využit pro stanovení energie hluboké hladiny. Výsledky z měření Pockelsovou metodou byly porovnány se spektry z luminiscenční spektroskopie, kde se zjistila korelace mezi přítomností hlubokých pastí a bodových defektů na povrchu.

Klíčová slova: CdTe, Pockelsův jev, elektrické pole, hluboké hladiny, Schottkyho kontakt

Contents

Table 1: Abbreviations

Table 2: Luminescence nomenclature

CdTe	Cadmium Telluride
DL	Deep Level
E-field	Electric field
e-h	electron-hole
FL	Fermi Level
Gap light	light with photon energy $\mathsf{E} > \mathsf{E}_G$
IR	Infra Red
QFL	Quasi-Fermi Level
IV	Current-Voltage
M-S	Metal-Semiconductor
MAC	Mass Attenuation Coefficient
NIR	Near Infra Red
PL	Photo-Luminescence
PVD	Physical Vapour Deposition
SRH	Shockley-Read-Hall
RMS	surface roughness Root Mean Square
SCD	Semiconductor Detector
Subgap light	light with photon energy $\mathsf{E} < \mathsf{E}_G$
WF	Work Function

|	
FX	Free exciton
A-X	Exciton bounded to acceptor
D-X	Exciton bounded to donor
DAP	Donor-Acceptor Pair
C-line	In dopant line
Y-line	Dislocation line
A-center	Negative vacancy-donor complex
LO	Longitudinal Optical phonon
n LO-Z	n-th LO replica of Z
ZPL	Zero Phonon Line

Table 3: List of selected symbols

d	Detector thickness
$\boldsymbol{D}, D$	Electric field displacement
$\boldsymbol{E}, E$	Electric field
E_C	Cathode electric field
E	Energy
E_A	Activation energy
E_c	Energy of the conduction band edge
E_v	Energy of the valence band edge
E_G	Energy gap
E_t	Energy of a deep trap
F	The Fermi level
I	Light power intensity
$\boldsymbol{J}$	Jones polarization vector
n	Refractive index
N_t	Density of deep level traps
R_{ijk}	Three-suffix Pockels coefficients
r_{ij}	Two-suffix Pockels coefficients
R	Reflectance
T	Transmittance
T	Temperature
U	Bias voltage
V	Electric potential
Q	Configurational coordinate
α	Absorption coefficient/Pockels renormalization factor
δ	Phase development of a wave
ε	Permittivity
Φ	Work function
η	Impermittivity/PL Efficiency
μ	Carrier mobility
τ	Detrapping time/Carrier lifetime

1. Introduction

1.1 Foreword about CdTe detector

A CdTe detector is a semiconductor device designed to detect X-ray, gamma and other ionizing radiation. It is able to directly convert every above-bandgap photon into a cloud of electron-hole pairs that can be further processed as a signal event. The concept of the device is based upon a cuboidal capacitor with cadmium telluride as an insulting dielectric. In its simplest form, the block of the CdTe detector is covered on the opposite sides with two thin-film metallic electrodes (Fig. 1.1). High energy photon generates charged cloud of electrons and holes that are separated in an applied electric field and collected at electrodes. Charge at the auxiliary capacitor C_A is proportional to the photon energy. As capacitor C_A discharges, its voltage is amplified and passed to the oscilloscope. After exposition of the detector to the radiation, a histogram - number of photon events versus voltage channel is acquired. In the case of monochromatic illumination, an uncertainty of maximum amplifier voltage V_{max} gives FWHM of the peak. The detector works in a photoconductive regime, low dark current in inter-event time is determined by high resistivity of semi-insulting monocrystal $(0.5 - 5\,\mathrm{G\Omega})$.

Figure 1.1: CdTe detector scheme.
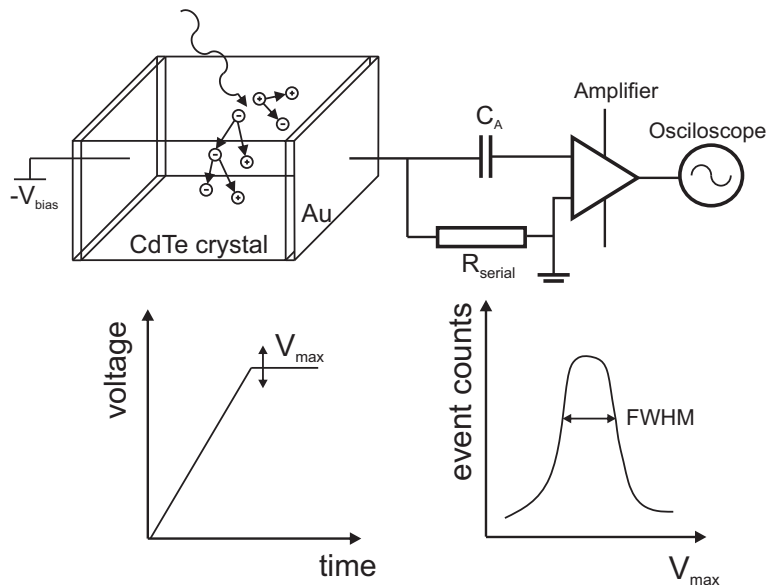
The significant merit of semiconductor detector (SCD) is its high sensitivity, time and spectral resolution due to the direct conversion. High atomic-mass detector material can serve as a protective shield with high radiation-damage resistance. Integration of detectors to a pixel array gives feasibility of spatial resolution. There are in general three types of gamma photon interactions in a crystal: inner photo-effect, Compton

3

scattering and electron-positron generation. The effective cross-section of photo-effect strongly increases with atomic mass of material and falls with photon energy. An important parameter describing charge collection efficiency of the photoresistor is a gain factor z defined as a ratio of the signal current J to the charge carrier generation G. The gain factor could be expressed in following sequence

$$z = \frac{J}{G} = \frac{q\Delta n \mu_e E A}{qgAd} = \frac{qg\tau_e \mu_e E A}{qgAd} = \frac{\mu_e \tau_e E}{d} = \frac{\lambda_e}{d} \qquad (1.1)$$

where q is the elemental charge, Δn electron concentration excess, μ_e the electron mobility, E the electric field, A the electrode area , d the inter-electrode distance, g the volume generation rate, τ_e the mean electron lifetime, $\lambda_e = \tau_e.(\mu_e E)$ means the electron drift distance. The last expressions in (1.1) say that high a $\mu\tau$ product means a better detector performance. The gain factor is dependent only upon carrier drift distance and detector thickness [1].

1.2 Motivation for the research

Figure 1.2: CdTe detector prepared for the purpose of this study (ID: B39UB1). Crystal dimensions $8 \times 5 \times 1.5\,\mathrm{mm}^3$. Contact metals Au/Au made by PVD.
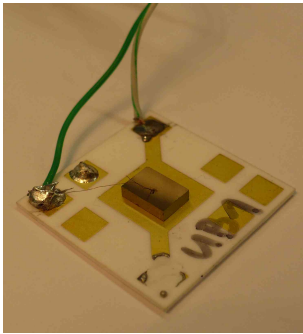
Market leading corporation Acrorad, Ltd. [4] presents two types of detectors. Firstly, it is Schottky type, high resistive, rectifying, with a low leakage current, biased to several hundreds of volts, with energy resolution <4-5% at 100 keV. The second type is ohmic, operating with bias up to 60 V, with energy resolution 5-7% at 100 keV, good time stability, higher leakage. Their latest product is a CdTe-CMOS panel sensor with 30k pixels, 100 μm pitch, 50 frames per seconds, applicable for X-ray fluxes generated up to 5 mA tube current. In the future of X-ray detection it replaces the rival architecture of scintillator-CCD. The main applications of CdTe detectors are for X-ray imaging in medicine, non-destructive testing in industry and security.

Contemporary bottle-neck of mainly Shottky-type CdTe detectors is a charge polarization causing a screening of the electric field. The generated charge is not perfectly collected. Residual charge is trapped in proximity of electrodes where carriers occupy states in the vicinity of the mid-gap (i.e. deep levels). Such region of spatial charge deforms the electric field profile and leads to the occurrence of dead layer where carriers movement is driven only by diffusion process. Detector operation could be recovered by diminishing of the accumulated charge. Charge vanishes for example by periodical switching-off the bias voltage for a short time (Fig. 1.3 and 1.4).

Another way of the restoration is based upon carrier detrapping induced by photoeffect after illumination with the wavelength corresponding to the energy of deep

levels [3]. One of the goal of this study is to survey capabilities and limitations of the mentioned idea for combination of rectifying and ohmic metal contacts gold-indium and gold-gold. Moreover, we will be interested in conditions of contact preparation and preceding surface treatment. Particularly, our objective will be focused on a difference between etching and polishing of the surface. The internal electric field will be studied using the Pockels electro-optical effect. Correlation between polarization, surface defects and stress will be researched using luminescence spectroscopy.

Figure 1.3: Time degradation of ^{241}Am signal caused by polarization. Degradation causes broadening and shift of the channel peak. Schottky type detector, bias 700V. Higher applied E-field makes polarization smaller. Adopted from [2].
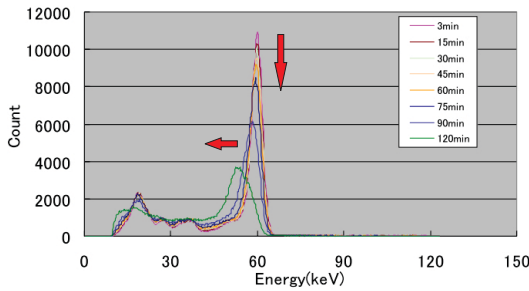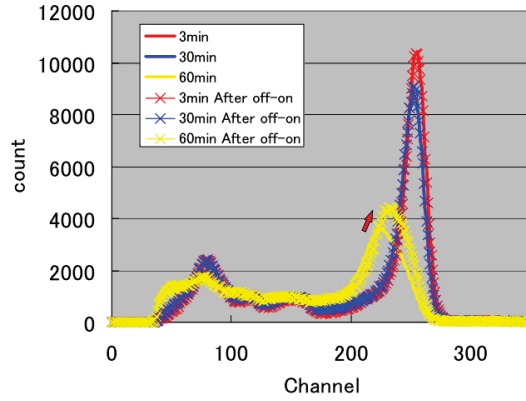
Figure 1.4: The recovery from the polarization by interrupting the bias for a one second (off-on action) [2].

1.3 Brief revision of Cadmium Telluride properties

CdTe is a II-IV compound semiconductor with 1.51-1.53 eV (300 K) direct band gap. CdTe has zinc-blende crystal structure and belongs to F$\bar{4}$3m space group (Fig. 1.7). Since the Pauling electronegativity of cadmium is 1.69 and 2.1 for tellurium, then Cd acts as a cation in the crystal lattice while Te plays the role of an anion neighbour. Its average atomic mass is 50 and ionization energy per electron-hole pair is 4.43eV [4]. The material is an effective absorbing medium for X-ray photons in the range of 3-150 keV. Only a 2 mm thin block stops about 90% of the incident photon flux at 100 keV [36]. Crystals can be easily scratched due to low mechanical hardness. The direction for easy crystal cleavage is parallel to (110) planes. The material is resistant to air moisture. High concentration of unfamiliar substituents can modulate the gap width (Hg, Zn, Mn for Cd and Se, S for Te).[1] Its effective mass for electron is $m_e^*/m_0 = 0.096$ and for hole $m_h^*/m_0 = 0.83$ [6]. Typical dark intrinsic resistivity ranges in the interval of $0.5 - 5 \times 10^9 \, \Omega$cm.

Zero temperature extrapolation of the band gap is (1.608±0.005) eV [7, 16]. Temperature dependence of CdTe band gap and dispersion of refractive index is dependent upon specific crystal preparation and origin. Many authors published more

---

[1]Addition a small percentage of Zn gives rise to resistivity that reduces leakage current of the detector.

Figure 1.5:   Energy band structure of CdTe [9]. Main electronic properties are given by direct 1.5 eV gap between Γ_8 and Γ_6.
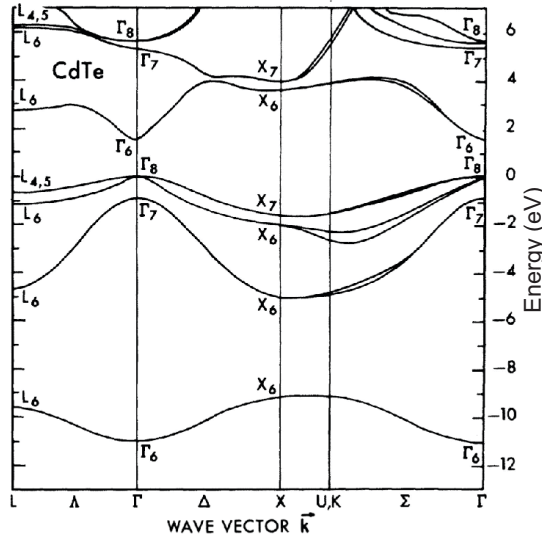
Figure 1.6:   Phonon dispersion of CdTe. Interaction with optical phonons are significant for ionic crystals, particularly LO with 21 meV at Γ. Retaken from [13].
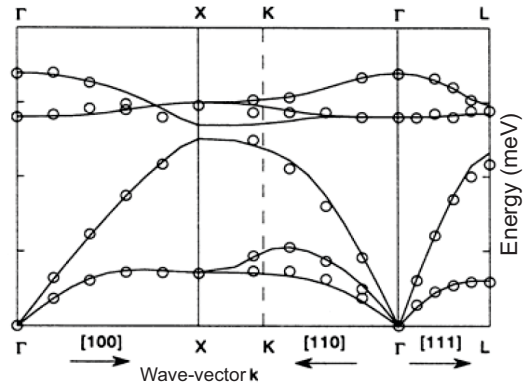
or less similar semi-empirical approximative equations. They accuracy and theoretical basis corresponds with the number of involved effects. The simplest formula supposed by VARSHNI [8] is

$$\mathsf{E}_G(T) = \mathsf{E}_{G0} - \frac{\alpha T^2}{\beta + T} \tag{1.2}$$

with $\mathsf{E}_{G0} = 1.6077\text{eV}, \alpha = 0.372\text{meV/K}$ and $\beta = 110\text{K}$ has the meaning of the Debye temperature, after [16]. Other selected properties are listed in table 7.1 at page 88. Energy band diagram and phonon dispersion diagram of CdTe are depicted at Fig. 1.5 and 1.6. CdTe has a strong electron-phonon coupling interaction, particularly with 21 meV longitudinal optical phonons.

Figure 1.7: Unit cell of the zinc-blende structure. Status of Cd and Te atoms is equivalent. Each Cd atom is surrounded with four Te atoms forming a centered tetrahedron. Four tetrahedra make a unit cell. Theoretical Te-Te (Cd-Cd) distance is 4.582 Å and 2.806 Å for Te-Cd. Bound angle Cd-Te-Cd is 109.5° and Te-Te-Te 60°, respectively.

Figure 1.8: The first Brilloune zone of the zinc-blende structure.

1.4   CdTe crystal growth
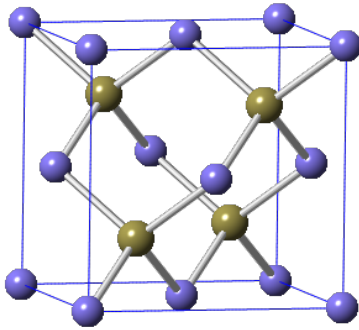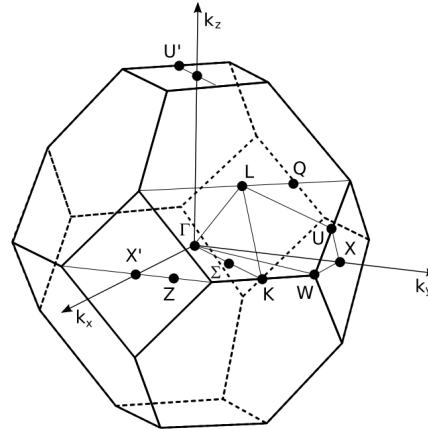
CdTe, a stoichiometric compound of Cd and Te, was firstly prepared by French chemist Margottet in 1879 [5]. Single CdTe crystals can be grown from Te-rich or Cd-rich melts. CdTe represents a sharp line segment at the temperature-concentration diagram at $c = 50\%$. Slight extra-addition of Te (resp. Cd) and fast cooling results in two-component phase (CdTe-Te) with precipitation of excessed element. Large difference in melting point of CdTe (1092°C) and boiling point of Cd (767°C) and Te (988°C) give possibility to adjust recrystallization conditions via gas phase pressure. High Cd vapour pressure at 500-1000°C does not allow to grow crystal directly by Czochralski method. Bridgman vertical gradient freeze technique makes possible to grow large-diameter ingots. The growth starts with seed orientation (111). Annealing or final recrystallization of the ingot can be done under encapsulation in quartz glass ampoule. Addition of a small amount of Cd powder at the ampoule and its heating equilibrate liquid composition during remelting process in Te-rich alloy. Cd vapour penetrates into the CdTe melt and reacts with surplus of Te. Resultant ingot is usually polycrystallic with macroscopic grain size of 1-3 cm. Each grain consists of an almost paralel set of subgrains with mutual low-angle boundaries.[2]

After the growth, the ingot is sliced to thin wafers and cut to small block pieces. A wire saw with SiC lubricant is used for cutting out the crystal grains and forming the required shape. Then, the sides are usually polished with fine Al_2O_3 powder or etched in bromine (iodine) solution to decrease surface roughness and get shinny

---

[2]Crystallinity and low angled boundaries between subgrains evinces for ingots grown at the Physics Institute of the Charles University. Large-scaled fully monocrystallic ingots can be obtained with contemporary methods [4].

Figure 1.9: Map of the CdTe surface etched in 1% Br-MeOH for 5 min. Measured by the optical interferometric profiler Zygo. Sample B39K4.

(a) Visualization of surface artefact occurred after etching.
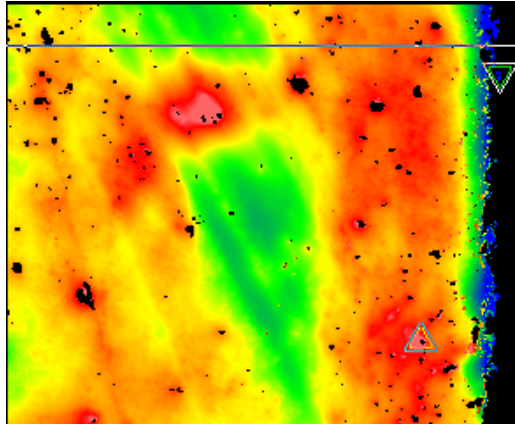
(b) Height profile along the line segment depicted above.
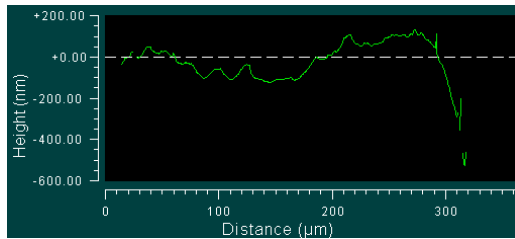
(c) Damage of the crystal edge.
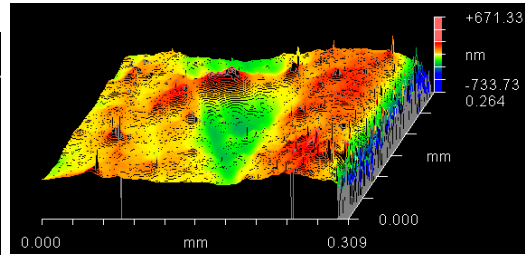
(d) Grey-scaled picture of the same spot highlighting smoothness and grooves.
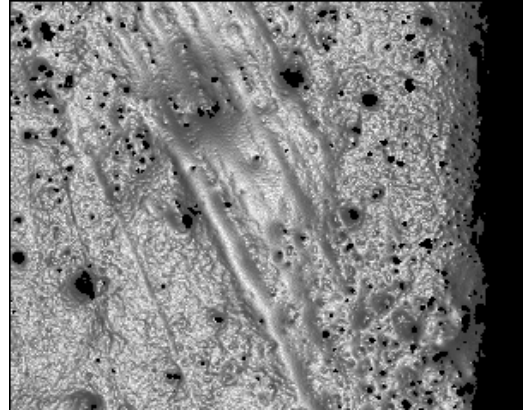
gloss [11]. Such treatment diminishes surface faults. Small-grained abrasive polishing smoothes the surface roughness root mean square (RMS) below several nanometers at area $100 \times 100 \, \mu m^2$. Surface RMS might be measured by an optical profilometer Zygo (Fig. 1.9d).

1.5 On lattice defects of CdTe

Within non-ideal growth and cooling process, many crystal defects occur. The easiest observable defects are probably Te precipitates and inclusions. When a droplet of an excessed element is solidified in matrix of CdTe, then a crystalline inclusion of a second phase is created with a typical size of $10 \, \mu m$. Inclusions are visible with an IR microscope or camera. Especially, Te inclusions form triangular or hexagonal grains. Precipitates are produced when diffusion of the excessed component to the crystal surface is quenched. Redundant atoms freeze in the matrix and create a cluster with lower energy. Tellurium volume defects can be eliminated by annealing in vapours of Cd at appropriate temperature and pressure. Line and plane defects are usually results of relaxation when the material was mechanically strained, e.g. after cutting or polishing. They might be also located in the vicinity of grain boundaries.

The last type of defects are atomic imperfections of lattice strongly affecting electronic and optical properties of the detector-grade material. The most common native

point defects are cadmium vacancy V_{Cd} followed by Cd, Te interstitials, substitutional antisite Cd_{Te}-Te_{Cd}, Frenkel pair interstitial-vacancy and more complicated atomic disordering. Temperature changes the position of the Fermi level (FL) that consequently influences the concentration of defects. Extrinsic defects come from impurities that are mixed to basic unpolluted materials Cd and Te. Sometimes dopant contamination is unintentional, particularly, when process of Cd, Te purification is not perfect (6-7N materials). Residual elements are regularly Cu, Li, Na, Ag, K or O with atomic concentration in order of $10^{15}\,\mathrm{cm}^{-1}$.
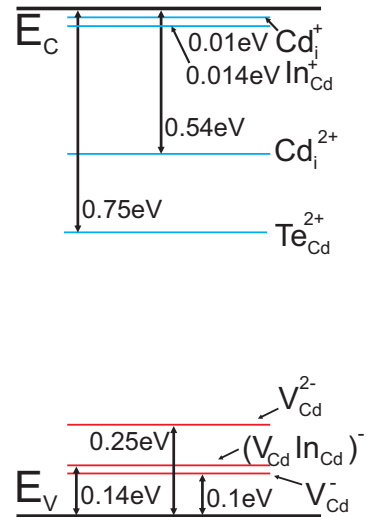
For intentional doping of intrinsic CdTe, there are used shallow donors In, Cl or deep donors Sn, Ge. Indium substitutes Cd and chlorine replaces Te. Both donor levels are positioned approximately 0.01-0.02 eV bellow the conduction band. Four-valent tin and germanium create extra states 0.9 eV below the conduction band edge and henceforth their electronic character is not strictly determined [20]. They are used for pinning of the Fermi level at the midgap. Location of the Fermi level and its displacement influences band bending as it will be in detail discussed in chapter 6. In the thermodynamic equilibrium cadmium vacancies are neutral V_{Cd}^0, single V_{Cd}^- or double ionized V_{Cd}^{2-} due to their different ionization energies. The vacancies act as acceptors, their position in the band gap diagram is shown in Fig. 1.10. The negative charge of the vacancy increases with the rise of the Fermi level [10,20]. Consequently, intrinsic CdTe with Cd vacancies behaves as a well-defined p-type with concentration $10^{15}\,\mathrm{cm}^{-3}$ under Te-rich grow condition.

Incorporation of a shallow donors In (Cl) leads to compensation of the semiconductor ($10^{16} - 10^{17}\,\mathrm{cm}^{-3}$). But exact balance between compensating dopants and negatively charged vacancies is problematic to preserve and rarely reproducible. Semi-insulating properties (resistivity $0.5 - 5 \times 10^9\,\Omega\mathrm{cm}$ [12]) are reached by addition of deep level dopant (Sn, Ge) up to $10^{15}\,\mathrm{cm}^{-3}$ fixing Fermi level in the midgap. Sometimes the FL is sufficiently fixed by natural defect Te_{Cd} with typical concentration $10^{11}\,\mathrm{cm}^{-3}$.

Figure 1.10: List of point defects in In-compensated CdTe and their position in the gap. After [20].

When a point defect is attached to an impurity atom then a more complex center is formed. For instance, a pair of donor dopant and vacancy with overall negative charge is called A-center. As we will see further, the key role in the CdTe detector development plays especially the complex V_{Cd}^{2-}-In^+. Similarly, a pair of donor and acceptor atoms creates a coupled unit. Recombination processes at complexes can be radiative and thus recognizable with luminescence spectroscopy.

2. Surface defects studied by luminescence spectroscopy

Surface as source of defects and tension

A certain part of CdTe deep levels originates from structural and point defects of the crystal lattice. They are mostly concentrated in the surface layer where they might contribute to the polarization effect and merge with the effect of band bending. Our task was to investigate the presence of deep levels in the damaged surface layer. As an indicator of the surface quality, CdTe photoluminescence was studied. A crystal face (311) of specimen B39K4 was subjected to two different surface treatments - polishing and subsequent etching. Although the polished surface is mirror smooth after it was rubbed by fine abrasive, we assume that the surface layer was stressed by tension. On the contrary, etchants remove the upper strained layer and leave a relaxed surface. Polishment was undertaken by Al_2O_3 grit of $1\,\mu m$ grain size with the resultant RMS 8nm. Succeeding process of wet etching was two-staged. Firstly, the sample was exposed to 1% solution of bromine in methanol for 1 min. Afterward, exposition to etchant was prolonged to the final 5 min duration. Etchant removes approximately $5\,\mu m$ of the upper material per minute. Optical-profilometer images of the final surface states is shown in Fig. 1.9d.

Experimental of luminescence spectroscopy

Experimental arrangement of our low temperature luminescence apparatus (Fig. 2.1) consists of an excitation laser, the sample held in a cryostat and IR Fourier transform spectrometer. Luminescence is collected from the side of excitation entrance. A titanium-sapphire CW Laser (Spectra Physics 3900s) was employed for excitation (tunable in the range 1.24 -1.77 eV, line width 0.16 meV, power 300 mW) and monochromatic Coherent Radius Laser (energy $1.943\,eV$, power $25\,mW$). Continual gas helium flow cryostat and resistive-wire heating enable to vary the chamber temperature from $4.2\,K$ to $300\,K$. Fourier spectrometer IFS 66S (Bruker) was equipped with silicon and germanium[1] detectors with sensitivity range 1.1-1.8 eV and 0.7-1.45 eV. Resolution of the spectrometer is 0.2-1 meV. Low-pass interference filter Semrock 1.565 eV was used as an edge filter.

Signal detected by luminescence

Dependency of the luminescence spectrum upon the excitation energy in $\mathsf{E}_E = 1.54$-$1.62\,eV$ and its temperature quenching within 4.2-250 K was measured. Intrinsic CdTe absorp-
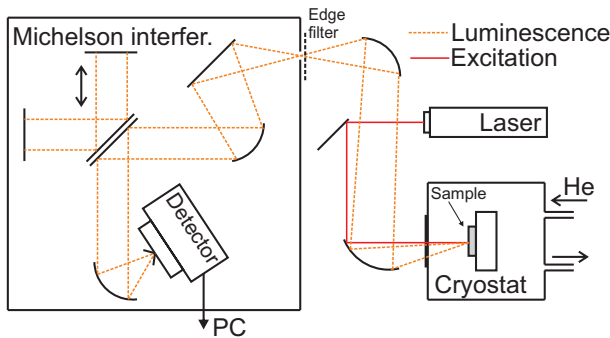
---

[1]Cooled by liquid nitrogen.

Figure 2.1: Scheme of the experimental set-up for measurement of CdTe luminescence in a back-reflection variant [18]. Sample is deposited in a continual He gas flow cryostat. Luminescence light is captured and directed to the Michelson interferometer through a set of mirrors. Thereafter, the intensity of interference is detected and a computer processes its inverse Fourier transform.
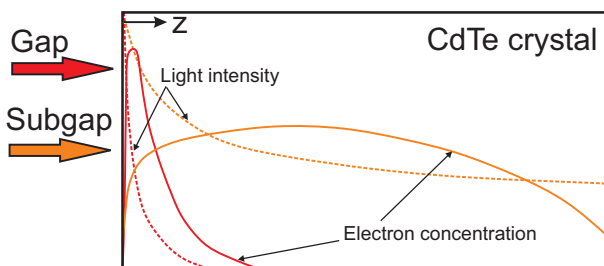
Figure 2.2: Intensity profile of the excitation light and distribution of generated electrons sketched for two extremal cases. Gap light is absorbed at the uppermost part of the crystal. Electron-hole generation is limited by surface recombination. Subgap light transmits through the entire sample and generation takes place relatively homogenously across the whole thickness.

tion coefficient α in the vicinity of the gap strongly varies from $200\,\mathrm{cm}^{-1}$ at $1.588\,\mathrm{eV}$ to $17000\,\mathrm{cm}^{-1}$ at excitation $1.605\,\mathrm{eV}$ ($T = 4\,\mathrm{K}$), [18] p. 48. Effective penetration depth z_{10} of excitation fulfills Beer-Lambert law $I(z_{10})/I_0 = \exp(-\alpha z_{10})$. Let us assume that z_{10} describes the depth where the intensity falls to 10% of its value just below the surface. For excitation $1.588\,\mathrm{eV}$ we obtain penetration $115\,\mu\mathrm{m}$ whereas for $1.605\,\mathrm{eV}$ only $1.4\,\mu\mathrm{m}$, $7.7\mu\mathrm{m}$ for $1.593\,\mathrm{eV}$ with $\alpha = 3000\,\mathrm{cm}^{-1}$ respectively. Hence, we see that the choice of excitation energy could serve as a tool for continual adjustment of the penetration depth, if the dependence of absorption coefficient $\alpha(\mathsf{E}_E)$ is known (Fig. 2.2).

Intensity of excitation light in the depth z is $I(z) = I_0(1 - \mathsf{R}_E)\exp(-\alpha_E z)$ where R_E is the back-reflection coefficient and α_E is an absorption coefficient for excitation energy $\mathsf{E}_E = \hbar\omega_E$. In the elementary layer $\mathrm{d}z$ at the depth z, $\mathrm{d}N_E$ excitation photons are absorbed

$$\mathrm{d}N_E = -\frac{1}{\mathsf{E}_E}\frac{\mathrm{d}I}{\mathrm{d}z}\mathrm{d}z\,. \tag{2.1}$$

A luminescent recombination is followed by emission of $\mathsf{E}_L = \hbar\omega_L$ photon. The action proceeds with quantum efficiency $\eta(\mathsf{E}_E, \mathsf{E}_L)$. In the layer $\mathrm{d}z$ de-excitation generates $\mathrm{d}N_L(\mathsf{E}_L)$ of luminescent photons

$$\mathrm{d}N_L = \eta(\mathsf{E}_E, \mathsf{E}_L)\mathrm{d}N_E\,. \tag{2.2}$$

One half of them propagates back to the crystal surface to be captured. On their reverse path, luminescent photons are attenuated with absorption given by α_L and partly reflected (R_L coefficient). Number of photons emitted from $\mathrm{d}z$ layer, that are

ideally collected from unit area and reach the detector, is

$$dN_D = dN_L(1 - \mathsf{R}_L)\exp(-\alpha_L z).\tag{2.3}$$

After the integration over the whole thickness of the sample we obtain final expression [13] describing the number of photons with energy E_L impinging to the detector

$$N_D(\mathsf{E}_E, \mathsf{E}_L) = \frac{1}{2}\frac{I_0}{\mathsf{E}_E}(1 - \mathsf{R}_E)(1 - \mathsf{R}_L)\frac{\alpha_E}{\alpha_E + \alpha_L}[1 - \exp(-(\alpha_E + \alpha_L)z)]\tag{2.4}$$

where R_E, α_E are functions of E_E, respectively R_L, α_L are functions of E_L.

2.1   Configurational coordinate model for localized center

For an interpretation of a deep level and A-center luminescence, the model based on a configurational coordinate will be adopted describing the radiative transition in a localized optical center (Fig. 2.3) [14, 15].

Figure 2.3: Radiation transition in the system of the localized luminescent center and lattice - representation of configurational coordination Q. After [14].
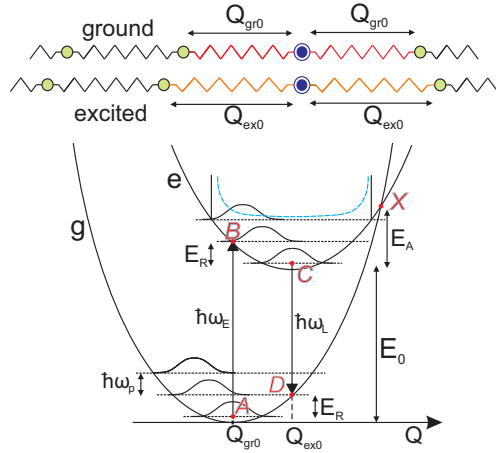
Let us assume a point defect or more generally an active localized complex center embedded in the lattice of neighbouring domestic atoms (Cd, Te). The entire system undergoes harmonic lattice vibrations at a non-zero temperature. Domestic atoms of mass m are mutually bounded with spring constant f_D. The defect of mass M is coupled with surrounding domestic atoms through the bound of strength f_{Cg}. A parameter describing general remoteness in the direct space between the optical center and the adjacent atom is denoted Q. In the ground state (no excitation), equilibrium distance within atom m and impurity is Q_{gr0}.

Energy of oscillating impurity E_{gr} is composed of the ground state E_{gr0} corresponding to the parabola vertex A, potential and kinetic energy given by the instantaneous displacement $Q - Q_{gr0}$, respectively by the velocity $\dot{Q}$

$$\mathsf{E}_{gr} = \mathsf{E}_{gr0} + \frac{1}{2}f_{Cg}(Q - Q_{gr0})^2 + \frac{1}{2}M\dot{Q}^2.\tag{2.5}$$

When the center absorbs energy of an excitation photon, it transfers to the excited state $A \to B$ and the configurational coordinate increases to Q_{e0} because of the repulsion between the excited electronic charge and ionic lattice. Its behaviour is governed by the upper displaced parabola with the vertex at $(Q_{e0}, \mathsf{E}_{gr0} + \mathsf{E}_0)$. The energy of the

excited center may be written analogically as (2.5)

$$\mathsf{E}_{ex} = \mathsf{E}_{ex0} + \frac{1}{2}f_{Ce}(Q - Q_{e0})^2 + \frac{1}{2}M\dot{Q}^2 \,. \tag{2.6}$$

Absorption of the excitation photon $\hbar\omega_E$ proceeds within the interval of about 10^{-15} s. Typical frequencies of lattice vibrations are spanned in the interval 10^{12}-10^{13} s^{-1} [14,15]. Therefore, the event of absorption takes place much faster than nuclei around the impurity could rearrange into new equilibrium positions. Thus, the process $A \to B$ is represented as a strictly vertical line, leaving the term $\frac{1}{2}M\dot{Q}^2$ unaffected.[2] Then, the system is thermalized reaching the minimum C and releases the excess energy E_R to the lattice through $\hbar\omega_p$ phonons. After a finite lifetime 10^{-9}-10^{-8} s, excited electronic states radiatively drop back to the ground state $C \to D$ emitting a luminescence photon $\hbar\omega_L$. Since a photon was emitted, the center approaches back to the initial state A following the path $D \to A$ and releases again appropriate number of phonons. If parabolas displacement goes to zero, i.e. $Q_{ex0} \approx Q_{gr0}$, then $\hbar\omega_L = \mathsf{E}_0$ and no phonon is emitted. Average numbers of phonons emitted during the relaxation of the center to the minimum of the parabolas $B \to C$ and $D \to A$ are equal and expressed by the dimensionless Huang-Rhys factor $S > 0$ as

$$\mathsf{E}_R = S\hbar\omega_p \,. \tag{2.7}$$

Higher values of S means the stronger center-lattice coupling and more of phonon replicas in the luminescence spectrum. At absolute zero temperature, distribution of replicas intensities is given by Poisson statistics

$$I(\text{n-th phonon}) \approx \frac{S^n}{n!}e^{-S} \text{ for } n = 0, 1, 2, \ldots \tag{2.8}$$

This yields the shape of the spectrum where the zero-phono line (ZPL) with energy $\mathsf{E}_L = \mathsf{E}_0$ is accompanied with satellite phonon peaks at $\mathsf{E}_L = \mathsf{E}_0 - n\,\hbar\omega_P$ (see A-center in Fig. 2.4). ZPL is the highest peak in the set, only if $S < 1$, e.g. for $S = 1$ the dominating replica is $n = 1$.

Strained induced displacement of an optical center

As the lattice is being strained in the damaged surface layer, ground Q_{gr0}^s and excitation Q_{ex0}^s coordinates are changed with respect to the coordinates of the relaxed surface Q_{gr0}^r, Q_{ex0}^r

$$\begin{aligned} \text{ground:} \quad & Q_{gr0}^r \to Q_{gr0}^s \\ \text{excitated:} \quad & Q_{ex0}^r \to Q_{ex0}^s \,. \end{aligned}$$

---

[2]Franck–Condon principle

Surface tension produces relative elongation or compression of the distance separating the optical center and the lattice. In notation of the configurational coordinate, it is written for $Q > 0$ as

$$
\begin{aligned}
\text{elongation}: \quad & Q_{gr0}^{r} < Q_{gr0}^{s},\ Q_{ex0}^{r} < Q_{ex0}^{s} \\
\text{compression}: \quad & Q_{gr0}^{r} > Q_{gr0}^{s},\ Q_{ex0}^{r} > Q_{ex0}^{s}.
\end{aligned}
\tag{2.9}
$$

Displacement $\Delta Q^{s} = Q_{ex0}^{s} - Q_{gr0}^{s}$ between the ground-state parabola and the excited-state parabola is enlarged and oppositely the parabolas of the compressed surface layer are closer each other. Spring constant and y-displacement of parabolas E_0 might be also altered since the arrangement of atoms constituting the complex is reorganised due to the stress. But in our phenomenological model an idea of the Hooke's law $e = s\sigma$ for continuous media is adopted. Here $e = Q^{s}/Q^{r}$ is the relative strain, s is a constant of compliance that is characteristic for the material and σ denotes the stress. Equivalent representation, that is more familiar with the concept of particles connected with springs (Fig. 2.3), says $F_{gr0} = f_{Cg}(Q_{gr0}^{s} - Q_{gr0}^{r})$ and $F_{e0} = f_{Ce}(Q_{ex0}^{s} - Q_{ex0}^{r})$ where F denotes the force deforming an optical center.

According to the parabolic scheme and formulas (2.5) and (2.6), the energy of the luminescent photon is expressed as

$$
\mathsf{E}_L = \hbar\omega_L = (\mathsf{E}_{ex0} - \mathsf{E}_{gr0}) - \frac{1}{2} f_{Cg}(Q_{ex0} - Q_{gr0})^2
\tag{2.10}
$$

where difference between ground and excited states $\Delta Q = Q_{ex0} - Q_{gr0}$ varies for the stretched and relaxed surface. Then the zero-phonon peak in a PL spectrum indicating the optical center is shifted by

$$
\Delta\mathsf{E}_L = \hbar(\omega_L^{s} - \omega_L^{r}) = \frac{1}{2} f_{Cg}(\Delta Q_s^2 - \Delta Q_r^2).
\tag{2.11}
$$

Lattice strain affects surface defects and adjacent crystal medium. Its magnitude weakens as we move deeper into the sample until it continuously disappears. This forms an effective depth $L_s \approx 30 - 50\,\mu m$ where the strained lattice is presented.

When the penetration depth is changed through the excitation energy, luminescence response comes from a thinner surface slab (Fig. 2.2). At a certain moment when the penetration depth and the effective strain depth coincide, the PL signal originates only from the damaged layer. Thus, an excitation dependency of luminescence could be exploited for estimation of the effective strain length L_s and indicates the nature of the defects prevailing at the specific excitation depth.

2.2 Luminescence of deep levels and A-center

CdTe has an intense luminescence signal originating from radiative recombination in deep levels, A-center, donor-acceptor pairs and excitonic annihilations.[3] Firstly, we will focus on luminescent features acting in the range of 0.7-1.55 eV (Fig. 2.4).

This region could be divided into two sectors. Primarily, it is a remarkable system of an A-center and its sixfold replica covering area 1.3-1.46 eV. Secondly, it is broadly spread transition of deep levels spanning from 1.3 eV to lower energies hardly measurable with Ge-detector.

PL of the strained surface evinces many overlapping peaks forming a wide band over 0.7-1.3 eV. Meanwhile, the relaxed surface possesses a pair of relatively close peaks at 1.2 eV and 1 eV. Their centers were obtained from decompositions into two Gaussian functions. Longer presence of the sample in the etchant bath empowers the first peak in the expense of the second one.

The observed A-center is the complex of an indium atom and double ionized cadmium vacancy In^+-V_{Cd}^{2-}. Signal from the A-center is noticeably suppressed and its satellites are reduced or even aborted for the stretched layer. Deexcitation processes are redistributed into more recombination channels. For example, the defect Y-line at 1.474 eV, attributed to dislocations, is strongly activated, likewise the unknown peak at 1.36 eV does. The rest of recombinations are not radiative. Displacement of the A-center ZPL and Y-line is approximately 20-23 meV and we cannot decide whether Y-line's replica or the ruin of the A-center remains.

Similarly, an excitation dependency of PL might be surveyed for damaged and restored surface (Fig. 2.5). Four different exemplary excitation energies were chosen for manifestation of the dependency. As the laser is tuned to a lower energy, excitation light penetrates deeper into the material and PL profile should resemble bulk spectra. Such limit case would have been in common for etched state as well as for a polished one, no matter how the surface was modified. This concordance is observed for low excitation 1.575 eV.

Only a behaviour of the deep level band is a little bit diverse. Polishing leaves 0.8-0.9 eV shoulder moreless unchanged and self-sustaining for various excitation energies. Its origin probably correspondents with the presence of an intrinsic point defect for the polished surface. For sample etched 1 min, the evidence of the shoulder is slightly visible; for 5 min long treatment it is entirely missing (Fig. 2.4). The deep tail band might be responsible for polarization of CdTe radiation detectors due to its midgap value. Whilst the DL peak at 0.86 eV and Y-line could be associated with the surface harmed by fine polishing, peaks at 1 and 1.2 eV are rather referred to the bulk.

---

[3]See the table of abbreviations 2 used in luminescence spectroscopy at page 2.

Figure 2.4: Luminescence spectra of polished and etched surface in the range of $0.7-1.5$ eV. Deep level peak at 1.19 eV is suppressed and wider band at lower energies is activated after polishing. Damaged surface also evinces extra Y-line of dislocations. Coupling between phonons and A-center is stronger for the restored surface after treatment in the etchant. Spectra are not corrected by the detector sensitivity function and filter transmittance. Sample B39K4 , T=4 K, excitation 1.943 eV, 25 mW, Ge detector.
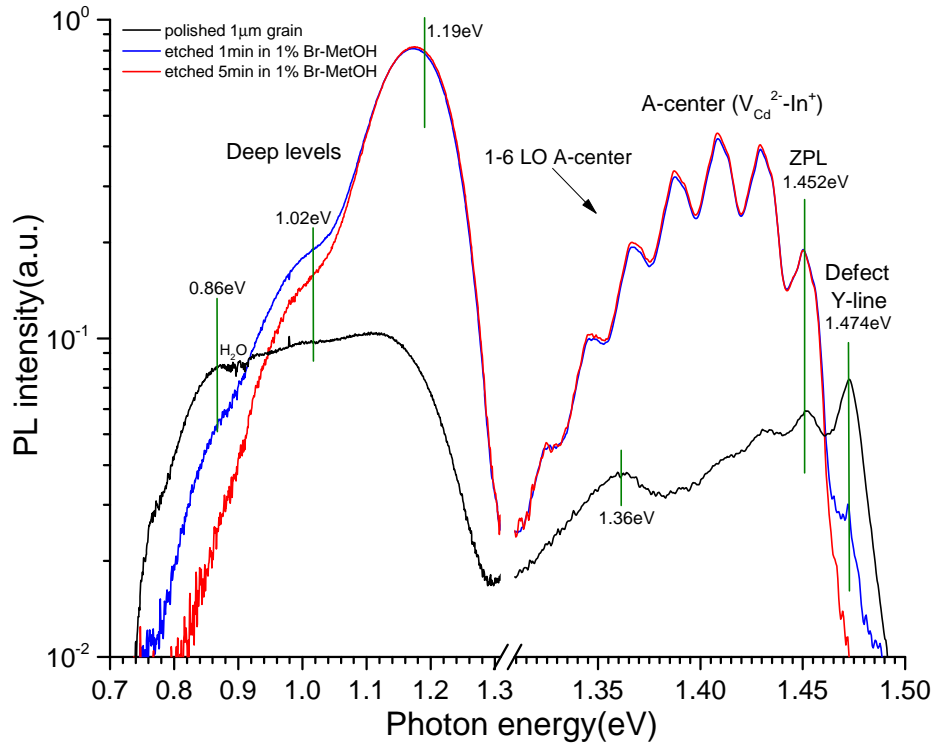
Figure 2.5: Luminescence spectra for various excitation energies. Higher energy is equivalent to a thinner surface layer of excitation. Etched and polished surfaces exhibit the same signal for 1.575 eV meaning that excitation takes place in the bulk interior. Contradictory, 1.717 eV excitation is the uppermost and the diametral disproportionality between the differently treated surfaces is evident. Sample B39K4, de-excitation range $0.8-1.482$ eV, $T=4$ K, Ge detector.
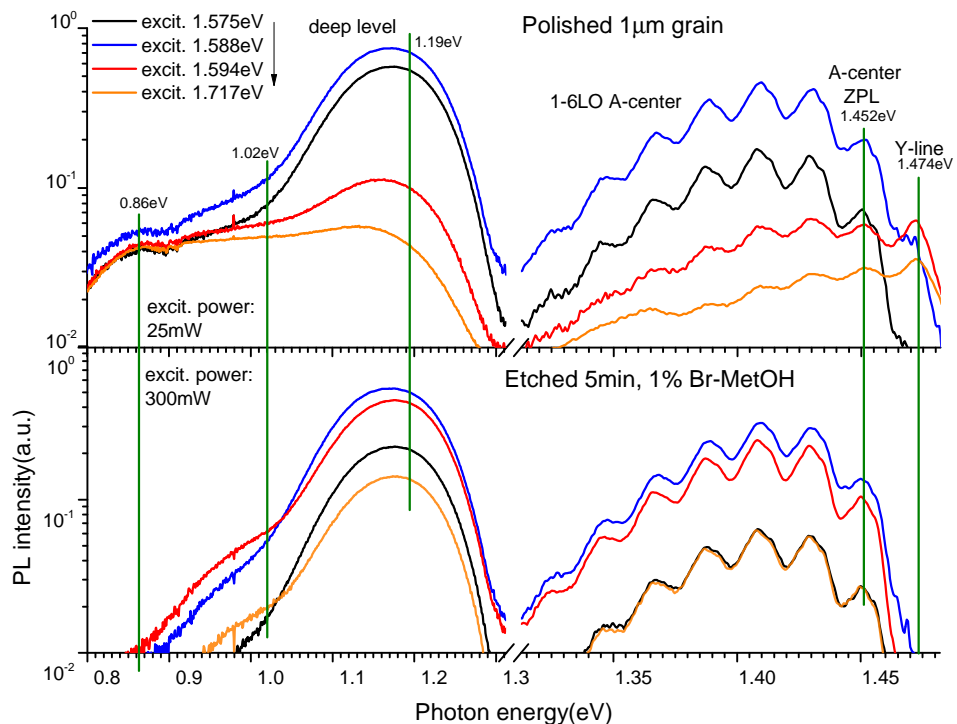
The idea of the equivalence between the surface depth profiling and tuning the laser excitation energy mediated by Beer-Lambert law using the known absorption dependency $\alpha(\mathsf{E})$ cannot be so trivially and straightforwardly implemented as was ambitiously stated so far. The situation complicates the fact of low temperature when the thermal noise does not overlap quantum effects[4] (Fig. 2.6). For a direct-gap semiconductor the curve for the absorption coefficient has a square-root rise $\propto \sqrt{\mathsf{E}_G - \hbar\omega}$ at room temperature. As the material is cooled, the proximity of the fundamental absorption edge is modulated by the huge absorption peak referred to the generation of free excitons in the ground state with energy $\mathsf{E}_{FX,\,n=1} = 1.5961\,\mathrm{eV}$. Monotony of absorption dependency is no longer conserved. The first excited state of an exciton ($\mathsf{E}_{FX,\,n=1} = 1.6037\,\mathrm{eV}$) is shifted by the value 7.6 meV. The first LO absorption replica of the free exciton with energy 1.617 eV lies beyond gap 1.606 eV [16] overlapping with the almost asymptotic value 24000 cm^{-1} of the fundamental absorption edge. Deeper to the band an exciton bounded on neutral centers A^0-X has weaker absorption peaks. For our case, it is a couple - C-line (1.584 eV) and A-X line (1.5894 eV) with correspondent binding energies 7 meV and 1.2 meV. Then far below the fundamental edge, the absorption falls to the left-side subgap asymptotic value $200 - 500\,\mathrm{cm}^{-1}$ [18].

Integration of the deep level spectrum in the range of $0.8 - 1.3\,\mathrm{eV}$ reveals its non-trivial dependence upon the excitation energy (Fig. 2.7). Initially increasing tendency is passed to two sharp spikes (addressed to C-line and A-X line[5]) followed by a swift drop of $\mathrm{FX}_{n=1}$. Furthermore, there is a mound for the case of the etched surface caused by the narrow transparent window (magenta in Fig. 2.6) cut by the notch of $\mathrm{FX}_{n=2}$. The curve ends with the asymptotic constant from the uppermost surface excitation when the penetration to the bulk is stopped by the high absorption coefficient.

---

[4]Low temperature is necessary for intense CdTe luminescence.
[5]Their origin is explained further in the section 2.4.

Figure 2.6:   Spectral dependence of the CdTe absorption coefficient at the helium temperature. Direct-gap dependence is modulated by absorption peaks of the free exciton (mainly by states $n = 1, 2$ and 1-th LO replica). The positions of excitation energies from Fig. 2.5 are tagged. The left plot focuses the region of the absorption below the fundamental absorption edge related to the bounded excitons [18], p. 48. The bottom plot shows the effect of the pure FX [16].
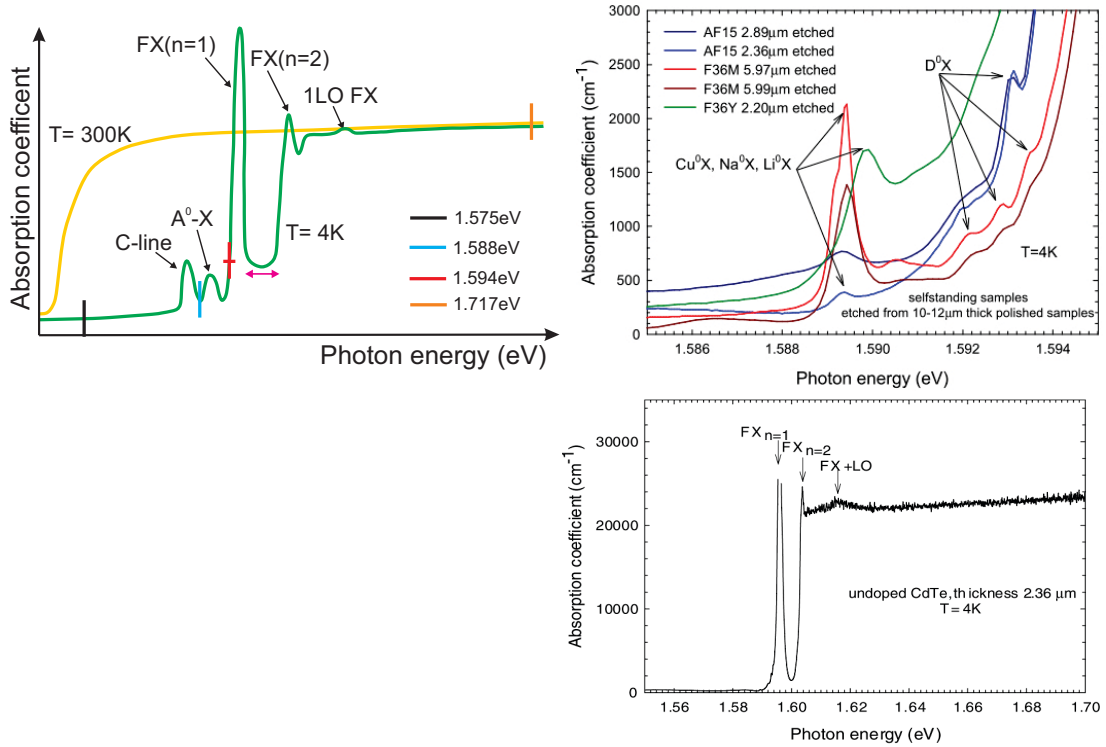
Figure 2.7:   Excitation spectrum of integrated PL from deep levels, i.e. integrated DL spectrum in dependence upon the excitation photon energy. Signal is not monotonous as excitation energy grows within $1.585 - 1.75$ eV. Resonant peaks are correlated with intense radiative channels of C-line and bound exciton. PL of the deep level is stronger for strained surface in $1.52 - 1.58$ eV and the excitonic part spanned in $1.595 - 1.605$ eV is missing. Integration range $0.8 - 1.3$ eV. Sample B39K4, $T = 4$ K, Ge detector.
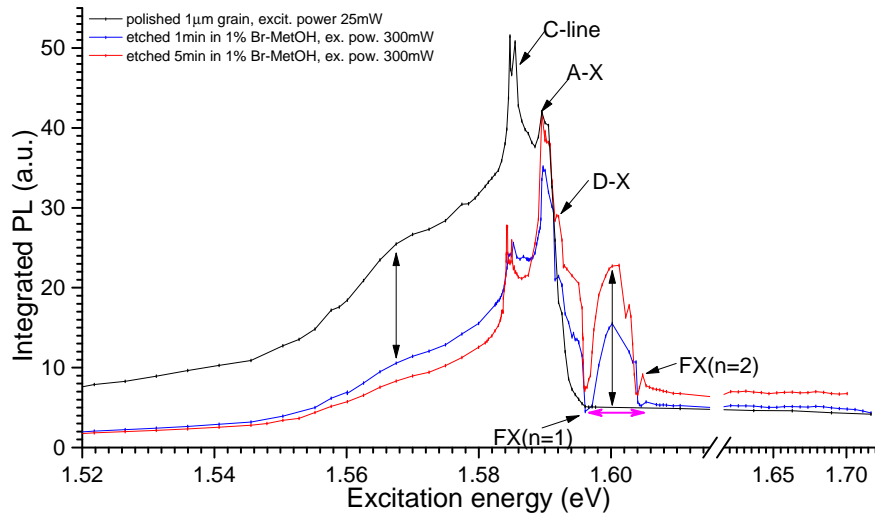
2.3 Thermal quenching of deep level luminescence

In the following analysis we demonstrate the effect of thermal quenching of luminescence revisiting the diagram in Fig. 2.3.

In general, a linear quantum oscillator cannot deterministically report the exact position of the vibrating impurity but it depicts only the density of probability determined by square of amplitude of its wavefunction. Classical probability of center's location is maximal at boundaries of the parabola (blue dashed line).

At a temperature close to zero, the center in excited states occupies a state in the proximity of point C. As the temperature T is increased, higher energy levels of the excited parabola are more probable and vibrations around Q_{ex0} extends. The chance of the system to reach the point X and overcome the potential barrier E_A becomes more realistic.

The height of the barrier E_A between C and X is equal to

$$\mathsf{E}_A = \frac{(\mathsf{E}_0 - \mathsf{E}_R)^2}{4\mathsf{E}_R} \, . \tag{2.12}$$

The probability p of overcoming the barrier E_A fulfills $p = p_0 \exp(-\mathsf{E}_A/k_B T)$ where p_0 is an extrapolation for zero temperature.

After the center passes point X, it has an option of a non-radiative return to point C by following the curve $X \to A$ while emitting phonons. Energy received from the absorption is fully converted into lattice vibrations, i.e. heat. If we denote τ_r probability of radiative transition $C \to D$ then quantum efficiency of luminescence can be expressed as

$$\eta = \frac{I}{I_0} = \frac{1}{1 + \tau_r p_0 \exp(-\mathsf{E}_A/k_B T)} \tag{2.13}$$

where I_0 is intensity of luminescence for $T \to 0$. For a sufficiently large temperature, the relation (2.13) reduces to a simpler Boltzmann form $1/\tau_r \nu_0 \exp(\mathsf{E}_A/k_B T)$.

However, sometimes luminescence grows in a short interval of temperature instead. The configurational coordination model can no longer encompass this fact and the semi-empirical formula needs to be engaged

$$\eta \sim \frac{T \exp(-\mathsf{E}'_A/k_B T)}{1 + \tau_r \nu_0 \exp(-\mathsf{E}_A/k_B T)} \tag{2.14}$$

introducing new low temperature activation energy E'_A [14]. Increase of luminescence with the rise of temperature is observed only in a limited temperature interval. Subsequent growth of temperature makes the quenching dominant and luminescence fades away in the end.

Deep band thermal quenching for the etched surface is compared with the polished one in Fig. 2.8. We restricted the experiment to the deep band from 0.8 eV to 1.3 eV attributed rather to the bulk than to the surface. The level at 1 eV is activated at a

Figure 2.8: Temperature quenching of deep level luminescence. Whilst for the polished surface the deep level band is continuous, for 1min-etched surface two dominant peaks persist. Their centers are marked by green line. Sample B39K4, excitation energy 1.72 eV, Ge detector.
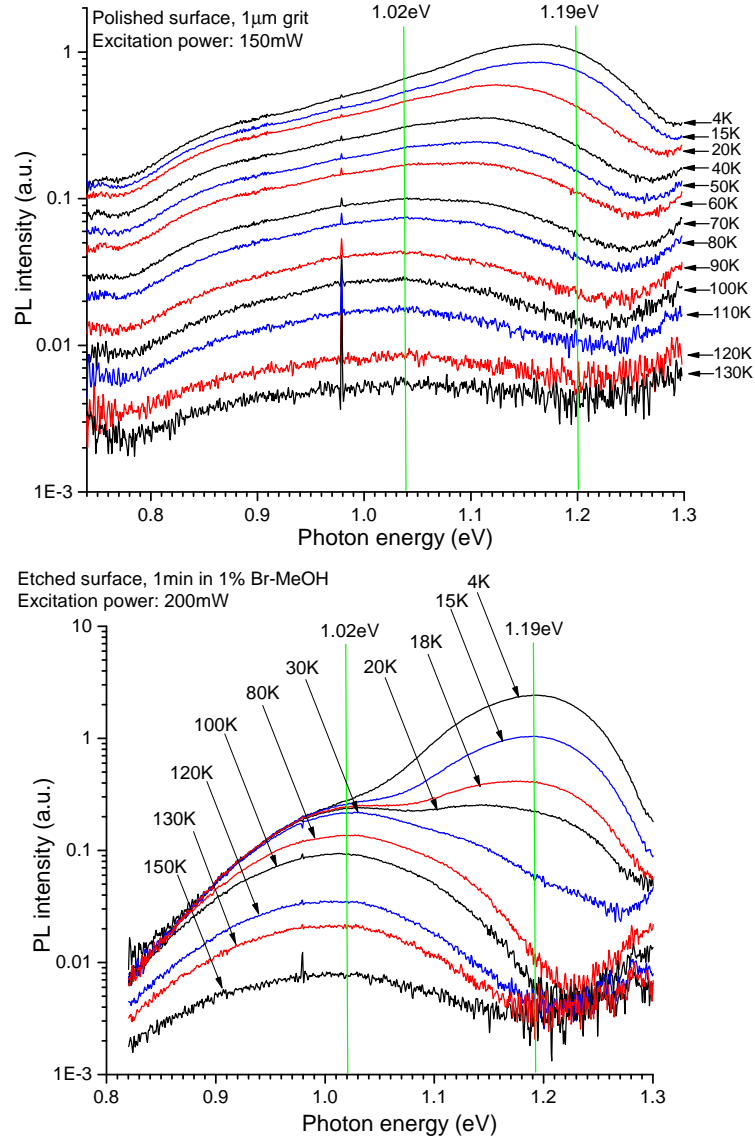
higher temperature (> 30 K) while the level at 1.2 eV is almost faded away. This holds for polished as well as for the etched surface. Approximative values of activation energies for the deep level band centered at 1 eV are $\mathsf{E}'_A = 3\text{-}5\,\mathrm{meV}$ and $\mathsf{E}_A = 60\text{-}80\,\mathrm{meV}$. For the polished sample the decomposition and fitting of spectra is troublesome. A new level at 0.9 eV is awaken and wide deep bands are redistributed and mutually overlayed.

From that reason it is beneficial to investigate integrated PL of the deep band (Fig. 2.9) as a function of temperature. One sees qualitative distinction between the monotonous curve for the polished surface described by formula (2.13) and the curve with a maximum at $T \sim 14\,\mathrm{K}$ better characterized through (2.14). Secondly, it is easily to recognize a change in the slope of the course and to notice quenching and activating of the levels in continuous band although the band is not separated to individual peaks.

Figure 2.9: Integrated luminescence spectrum as a function of temperature. Integration is separated into two regions: 0.8-1.3 eV deep band, 1.3-1.485 eV A-center and Y-line. While PL of etched surface evinces maximum at T=14 K, PL of polished sample is strictly decreasing. After polishing PL of the A-center is anti-correlated with the deep band. Same experimental conditions as in Fig. 2.8.
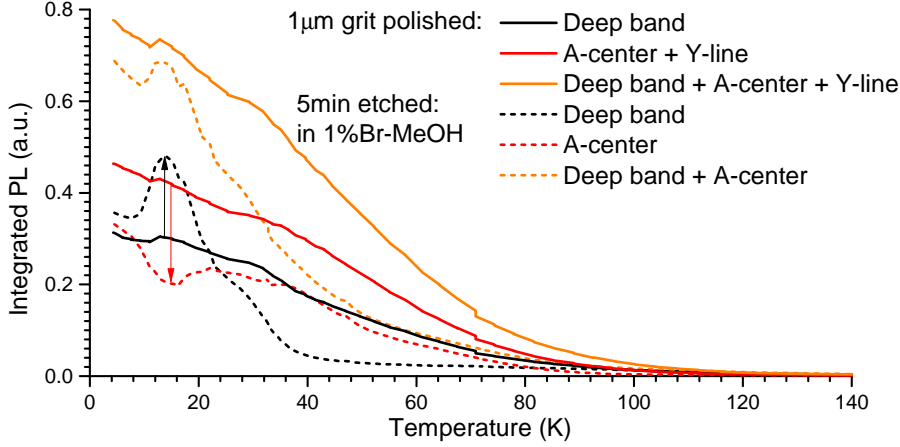
In addition, we point out the anti-correlation between the integrated spectrum of the deep band and A-center for the relaxed surface where the mutual coupling is stronger.

Unfortunately, the deep level at 0.8 eV in Fig. 2.5 connected with the surface defects is at the border of the Ge detector sensitivity and thus hardly experimentally available.[6] Our aim is to verify the following physical relationship between the PL thermal quenching and PL dependency upon the photon energy of the excitation laser in the framework of the proposed model of the configurational coordinate. In the stretched[7] system of the optical center, a horizontal displacement between the excited and the ground-state parabola is extended. Hence, optical transitions are moved in the spectrum to the lower photon energies (red shift). Furthermore, the barrier for the non-radiative transition $C \rightarrow X \rightarrow A$ is lowered and its activation energy E_A is decreased. Thermal quenching of the stretched layer should begin at lower temperatures since the activation energy of the non-radiative channel is smaller than for the relaxed optical center. In the excitation dependency we anticipate the red shift of the DL as the excitation is tuned to the higher photon energies.

Oppositely, when the system of the optical center is compressed, parabolas are closer to each other. The optical transition becomes blue-shifted, thermal barrier for the non-radiative recombination is enlarged. Consequently, thermal quenching is reduced because more heat from the lattice must be transmitted to the excited center.

However, for the excitation energy below the fundamental absorption edge the mentioned effect should not be presented since the strained and relaxed surface should

---

[6]In the upcoming time, the luminescence experiment will be repeated with a detector based on InSn with an effective sensitivity in the lower range 0.45-1.2 eV.

[7]elongated

exhibit the same bulk behaviour.

The idea does not take into account competitive recombination among the channels and thermal change in the occupation of the defect states. Our configurational model is only one-dimensional and not respecting all degrees of freedom of the system. On the top of that, the configurational coordinate might not be directly related to a geometrical coordinate and the system can consist of more than two electronic states represented by parabolas.

2.4   Luminescence of exciton and donor-acceptor pairs

In subsequent paragraphs we will briefly discuss the PL results obtained in the spectral region of excitons and D-A pairs spanned in $1.55 - 1.6\,\text{eV}$ close to the intrinsic CdTe absorption edge.

Let us review essential theoretical formula for energy of a free exciton in n-th state

$$\mathsf{E}_{X,n} = \mathsf{E}_G - \frac{m_r^*/m_0}{\varepsilon_r}\frac{1}{n^2}\,Ry\; + \frac{\hbar^2 K^2}{2(m_e^* + m_h^*)}\,, \qquad (2.15)$$

where E_G is energy of the gap, m_0 free electron mass, ε_r relative permittivity, Ry Rydberg constant, m_r^* is reduced mass defined as $1/m_r^* = 1/m_e^* + 1/m_h^*$ and finally $\hbar K$ means quasi-impuls of the exciton. Energy of bound exciton is lowered by the characteristic binding energy $\mathsf{E}_B > 0$ associated to a specific impurity

$$\mathsf{E}_{BX,n} = \mathsf{E}_{X,n}|_{K=0} - \mathsf{E}_B\,. \qquad (2.16)$$

Energy of a photon E_{DAP} emitted during the electron-hole recombination between donor D and acceptor A described as $D^0 + A^0 \rightarrow D^+ + A^- + E_{DAP}$, is given by

$$\mathsf{E}_{DAP} = \mathsf{E}_G - \mathsf{E}_A - \mathsf{E}_D - \frac{e^2}{4\pi\varepsilon_0\varepsilon_r R}J(R) \qquad (2.17)$$

where E_A, E_D denotes energy of the shallow acceptor, resp. donor in the energy band diagram, R means distance separating both centers, $J(R)$ is a wavefunction overlap integral [14].

Typical very sub-edge spectra consist of a bound exciton, sharp lines from chemical elements and donor-acceptor pairs (Fig. 2.10). Some abundant native defects act as optical centers and their electronic states and energies are summarized in Fig. 1.10. Mother ZPL lines are multiplied with satellite replicas after interaction with longitudinal optical 21 meV phonons. Number of occurrence signifies quality of coupling between the optical center, resp. quasi-particle and lattice.

Free exciton luminescence due to its self-reabsorption exhibits the shape of a notch instead of a peak. The identical notch is observed in the reflectance curve. Photon, created after the annihilation of a free exciton, followed by emission of phonons can

Figure 2.10: Excitonic part 1.55-1.604 eV of luminescence spectrum and neighbouring region of donor-acceptor pairs 1.49-1.55 eV. Strong C-line corresponds to complex $V_{Cd}-In_{Cd}$ or $V_{Cd}-In_i$. Free exciton is observed as a notch harmonically coincident with the reflectance. Free exciton and donor-acceptor pairs are reduced for the polished surface. Sample B39K4, $T = 4$ K, excitation 1.943 eV, 25 mW, Si detector. Spectrum normalized to 1.
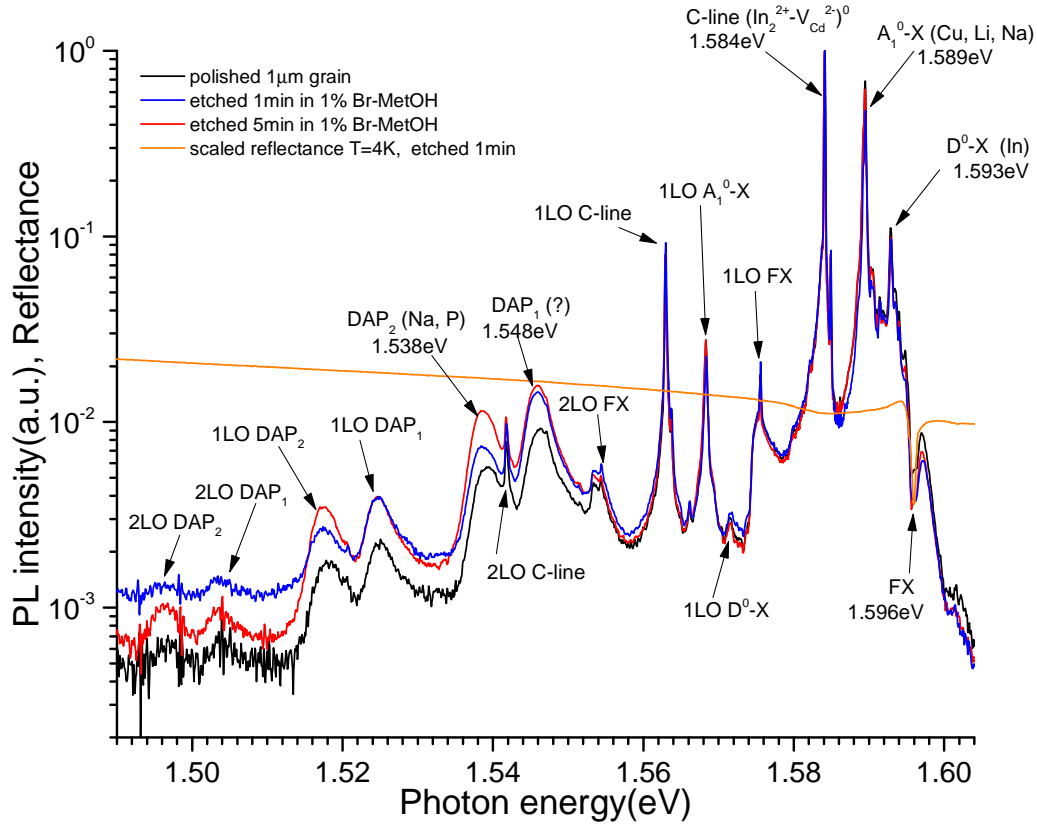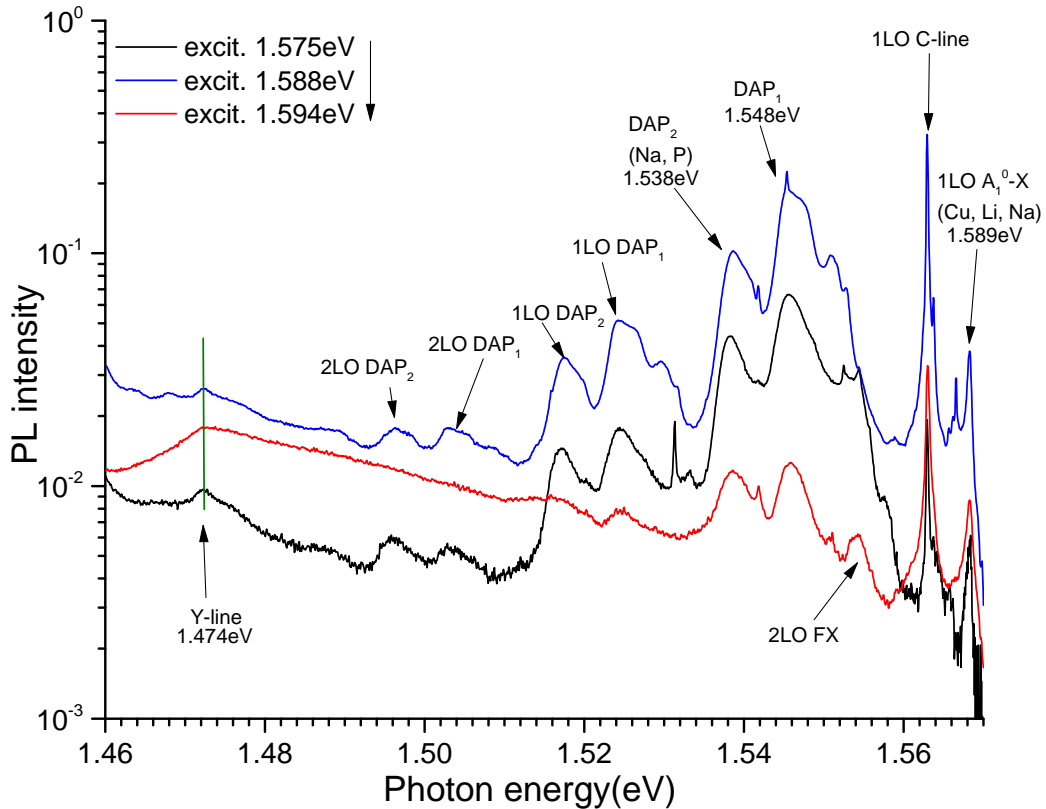

Figure 2.11: Luminescence of exciton and DAP in 1.46-1.57 eV for a triplet of distinguished excitations. At higher energies fine structure is diminishing and defect Y-line persists. Polished sample B39K4, $T = 4$ K, excitation power 25 mW, Si detector.

propagate liberally towards the crystal surface. Ergo, *n*-LO replicas of FX are observed as peaks not notches.

Lines from annihilation of excitons bounded to impurities (defect complexes) are not broadened with Boltzmann distribution because the quasi-particle recombinates with null kinetic energy [13] and their typical FWHM is about 1 meV. The sharp shoot at 1.584 eV is called C-line. Its origin is attributed to the exciton bounded to indium-vacancy complexes such as In^+-V_{Cd}^{2-}-In^+. While the line at 1.593 eV belongs to donor In_{Cd}, line at 1.589 eV is supposed to be associated to one of elements Cu, Li, Na. Sharpness of 'tooth-like' surrounding background is below the resolution of the spectrometer.

Doubled donor-acceptor pairs at 1.538 eV and 1.548 eV are featured with significant left-side replicas. Etching increases their importance, particularly the one located at 1.538 eV. The origin of the acceptor is often referred to the sodium residual impurity substituting a cadmium atom. The nature of the donor is not so crucial, because the most of them having very similar positions.

An attempt to portray the depth profiling via variation of excitation energy is caught in Fig. 2.10. When the laser tunes the excitation 1.588 eV, the bottom of valley in the middle of *BX* absorption peaks is hit (Fig. 2.6 blue mark). The crystal becomes more transparent than for lower excitation energy 1.575 eV and PL is more intensive.

Defect Y-line accompanying dislocations is the only indicator of the surface damage in the plot. As excitation energy grows, Y-line is persistent or slightly boosted, meanwhile the rest peaks fade away.

Summary of the main results

The attention was focused on the difference between luminescence of the polished and etched CdTe surface in the range of deep radiative transitions. PL of the polished surface (damaged and strained 30-50 μm layer with dislocations and defects) evinces wide continuous band of overlapping deep level maxima. Excitation dependency revealed the correlation of 0.8 eV peak with surface. For the case of etched (relaxed) surface only peaks at 1 and 1.2 eV persist (bulk nature). Thermal activation energy of the level at 1 eV is lower than for the peak at 1.2 eV. Their absolute position in relation to the edge of the conduction or valence band was not yet fully understood [17]. Activity of V_{Cd}^{2-}-In^+ A-center is suppressed after polishing while the dislocation Y-line significantly appears.

Verification of the validity and subsequent implementation of the configurational coordination model would be possible after additional PL measurements. CdTe absorption is strongly influenced by free exciton and C-line close to the fundamental absorption edge. Excitation sweep of integrated deep level spectra showed a transparent window between the ground and the excited states of the FX.

3. Metal-Semiconductors junction, carrier trapping in semiconductors

3.1 Schottky theory of metal-semiconductor interface

Since a metal and a semiconductor have qualitatively diverse electronic structure, a divide in the shape of a barrier or slide must occur for charge carriers transported across their mutual junction. In the metal the concentration of electrons is enormous in comparison to the semiconductor. At zero temperature electrons occupy states below the Fermi level (FL) and leaving the states above empty (Fig. 3.1). When the temperature is elevated, the FL border for occupation is described with the Fermi-Dirac statistics. However, the shape of the electron distribution is approximately conserved, even if the FL edge is smoothed and no longer sharp and strictly step-like.

In the semiconductor there are two bands of electronic states separated by a forbidden gap. For an intrinsic semiconductor the FL lies in the vicinity of the midgap. For an extrinsic n-type semiconductor (with shallow donors) the FL is located closer to the conduction band, whereas for a p-type the FL is positioned towards the valence band.

Work function Φ is an energy that an electron located at the FL needs to leave the semiconductor and reach the vacuum with zero kinetic energy, i.e. it is a distance between the Fermi and the vacuum level $\Phi = \mathsf{E}_{vac} - \mathsf{F}$. Electron afinity is defined as an energy that must be supplied to the electron at the conduction band edge E_c to quit into the vacuum, i.e. $\chi = \mathsf{E}_{vac} - \mathsf{E}_c$.

Let us firstly analyse the situation $\Phi_M > \Phi_S$ and restrict our consideration to the n-type semiconductor. When the metal and semiconductor are linked, the Fermi levels of both materials are balanced $\mathsf{F}_M = \mathsf{F}_S$ across the whole system in the thermal equilibrium. Electrons from the semiconductor transfer to the metal and the depletion region of positively charged donors is formed. At the interface $z = 0$, the valence and the conduction band are curved, meanwhile in the semiconductor bulk the initial band structure is preserved ($\mathsf{E}_c - \mathsf{F}_S = $ const.). The potential drop between the semiconductor conduction band and the metallic FL is

$$\Phi_{Bc} = \Phi_M - \chi_S \tag{3.1}$$

25

Figure 3.1: Schottky model of the metal-semiconductor junction.
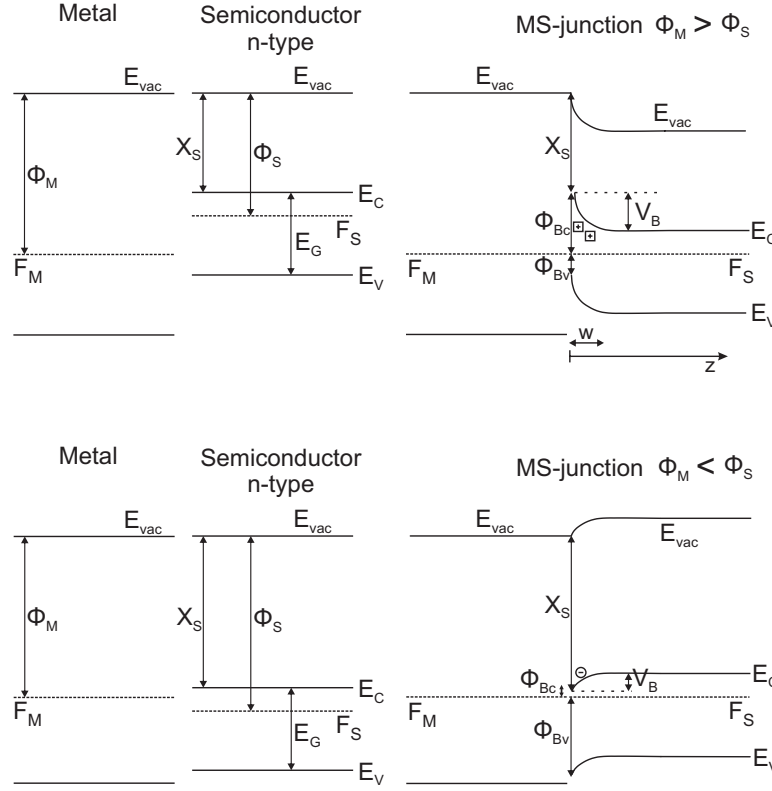
and the drop between the valence band and the F_M is

$$\Phi_{Bv} = E_G - \Phi_M - \chi_S \tag{3.2}$$

with the notation introduced in Fig. 3.1. Direction of the band incurvation is dependent upon the type of the semiconductor but the absolute value of the potential drop Φ_{Bc} does not matter on semiconductor's doping. For the n-type semiconductor the bands are bent upwards after the junction is formed. Now, when an electron should transfer from the semiconductor to the metal, it must overcome a built-in barrier

$$V_B = \Phi_{Bc} - |E_c - F_S|. \tag{3.3}$$

The scope of the charge depletion is limited within the width w towards the semiconductor bulk. Under the abrupt approximation the space charge density in the depleted layer $z \in (0, w)$ is constant $\varrho(z) = qN_D$ where N_D is the concentration of shallow donors. Charged density creates the electric field spread across the whole thickness of depletion

$$E(z) = -\frac{qN_D}{\varepsilon_S}(w - z) = -E_{max} + \frac{qN_D}{\varepsilon_S}z \tag{3.4}$$

and develops the electric potential

$$V(z) = \frac{qN_D}{2\varepsilon_S}(z - w)^2 + V(w) \tag{3.5}$$

where ε_S denotes the permittivity of the semiconductor and q is the elementary charge. The increase of the E-potential is proportional to the built-in barrier growth, thus $V_B = V(0) - V(z)$. From this boundary condition and the formula (3.5), we obtain depletion thickness $w = \sqrt{2\varepsilon_S V_B / q N_D}$. When the junction is biased[1] to voltage $U > 0$, the barrier width reduces to

$$w = \sqrt{\frac{2\varepsilon_S(V_B - U)}{qN_D}} \, .$$ (3.6)

Now we will comment the result for the opposite situation $\Phi_M < \Phi_S$ and the n-type semiconductor. Here, the Fermi level F_S lies under the F_M. After the connecting of the materials, F_S rises, electrons flow from the metal to the semiconductor and the Fermi levels are equilibrated. The semiconductor bands are tilt down. The vacuum level and the FL serve as two continuous energetic references. The concentration of electrons n_c in the conduction band is given by

$$n_c(z) = n_{c0} \exp \frac{-|\mathsf{F}_S - V(z)|}{k_B T} \, .$$ (3.7)

and especially for $z = 0$

$$n_c(0) = n_{c0} \exp \frac{-|\Phi_S - \Phi_M|}{k_B T} \, .$$ (3.8)

where n_{c0} is the equilibrium value of n_c for the free-standing semiconductor [22]. We have discussed only an ideal M-S junction where no surface states or surface dipoles influencing the barrier height are presented.

3.2 Schockley-Read-Hall model for occupation of traps

The SRH model describes statistical recombination and generation processes in a semiconductor with a level of free states positioned between the conduction and the valence band. Such states are distributed in the band diagram with the same energy E_t and constant concentration N_t. The states act as electrically neutral vacancies with an ability to capture or release an electron or a hole (Fig. 3.2). Ionisation of the trap can be done by the hole capture from the valence band or by excitation of an electron from the trap to the conduction band. Oppositely, emission of the hole from the trap to the valence band or electron capture from the conduction

Figure 3.2: Thermal and optical transitions of electrons in semiconductor with a trapping level.
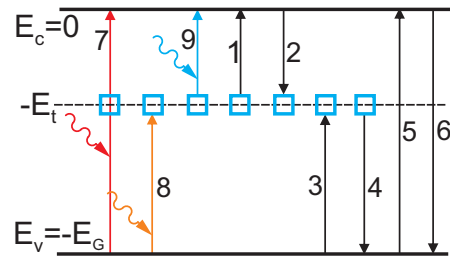
---

band lead to the negative occupation of the trap. It is equivalent if we speak strictly in the terms of purely electron transitions or if the representation of the hole as a positive charge carrier is supposed. Composition of the electron transitions 2 and 4 lead to the recombination across the level E_t, similarly process 3 followed by 1 generate an electron in the conduction band. Process 2 and 1 stand for the trapping and detrapping of the electron from the conduction band, whereas 3 and 4 do the same for an electron from the valence band.

Besides this, the thermal band-to-band generation and recombination across the gap take place in a semiconductor (processes 5, 6). Their contribution to the total electron concentration n_c in the conduction band is given by the gap energy and the temperature. Carrier generation might be also done through the inner photo-effect 7. Photons with appropriate energies provide optical excitations of electrons (processes 8, 9) from/to the level E_t.

The whole step-by-step derivation of the model is presented in the original paper [19] of SHOCKLEY. We will just point out the idea and review main results connected with the trapping and detrapping rates important for our problem [1]. In upcoming chapters we employ the SRH model as a way-out and a universal concept for consideration and analysis of the polarization processes in CdTe detectors.

Description of the trapping mechanism

We will describe the action of electron trapping 2 through the coefficient $C_n = \sigma_n v_n$ where v_n means thermal velocity of electrons and σ_n is their effective capture cross-section. The number of transitions per unit time in a unit volume is directly proportional to n_c and to the concentration of empty traps $p_t = N_t - n_t$

$$P_2 = C_n n_c (N_t - n_t) \, . \tag{3.9}$$

In the same way, process of the hole capture can be written as

$$P_4 = C_p \, n_t \, p_v \, . \tag{3.10}$$

Analogically, coefficient for the hole capture C_p is introduced, n_t means the electron concentration on the trap level and p_v denotes the hole concentration in the valence band. Electron emission to the conduction band 1 is not dependent upon the concentration n_c in the band but only upon the concentration at the level n_t

$$P_1 = e_n^t \, n_t \tag{3.11}$$

where is e_n^t is an unknown parameter of the thermal emission.

In the thermal equilibrium, the filling of all levels is balanced, i.e. emission rate P_1

is equal to the trapping P_2. The balance leads to the expression of the concentration n_t

$$n_{t0} = \frac{N_t}{1 + e_n^t/C_n n_{c0}} \tag{3.12}$$

where n_{c0} indicates the equilibrium value. On the other hand, from the electron statistics it follows that[2]

$$n_{t0} = N_t f_{t0} = N_t \left[1 + \frac{1}{g} \exp \frac{\mathsf{E}_t - \mathsf{F}}{k_B T} \right] \tag{3.13}$$

where F stands for the Fermi level, f_t denotes the occupation number given by the Fermi-Dirac statistics, g is a degeneracy factor, hereafter $g = 1$. After the simple comparing of expressions (3.12) and (3.13) for n_t, one obtains the formula for the emission coefficient

$$e_n^t = C_n n_{c0} \exp \frac{\mathsf{E}_t - \mathsf{F}}{k_B T} = C_n N_c \exp \frac{\mathsf{F}}{k_B T} \exp \frac{\mathsf{E}_t - \mathsf{F}}{k_B T} = C_n n_{c1} \tag{3.14}$$

where $n_{c1} = N_c \exp(\mathsf{E}_t/k_B T)$. In the same manner process 3 and 4 can be treated resulting in $e_p^t = C_p p_{v1}$ and $p_{v1} = N_v \exp \frac{-\mathsf{E}_G - \mathsf{E}_t}{k_B T}$. Artificial values n_{c1}, p_{v1} are interpreted as band concentrations n_c, p_v for the situation when F coincides with E_t. Balance between processes 1, 2 and 3, 4 can be restated in the terms of n_{c1}, p_{v1} as

$$\begin{aligned} P_1 &= e_n^t n_t = C_n n_{c1} n_t \,, \\ P_3 &= e_p^t (N_t - n_t) = C_p p_{v1}(N_t - n_t) \,. \end{aligned} \tag{3.15}$$

The electron-hole (e-h) pair generation 7 in a thin slab[3] is equaled to a light decrement

$$P_7 = \eta \alpha I \tag{3.16}$$

where I is the intensity of illumination with photon energy $\hbar\omega$, α denotes the optical absorption coefficient, η represents the quantum efficiency of generation, i.e. number of e-h pairs generated by $\hbar\omega$ quantum, e.g. for photon energy $\hbar\omega \geq \mathsf{E}_G$ holds $\eta \geq 1$.

We will describe optically induced emissions from the traps 9 and 8

$$\begin{aligned} P_9 &= e_n^o n_t \,, \\ P_8 &= e_p^o (N_t - n_t) \,. \end{aligned} \tag{3.17}$$

introducing similar emission coefficients e_n^o and e_p^o as in (3.11), but for this case

$$e_n^o n_t = \sigma^o I n_t = \frac{\eta \alpha I}{n_t} n_t = \eta \alpha I \,. \tag{3.18}$$

Finally, equipped with all necessary we are able to write down the three equations

---

[2]The convention used here takes the zero energy at the conduction band edge.
[3]In a thin slab per unit time and per unit volume.

of carrier kinetics

$$\frac{\mathrm{d}n_c}{\mathrm{d}t} = -C_n n_c (N_t - n_t) + (e_n^t + e_n^o) n_t + \eta \alpha I$$

$$\frac{\mathrm{d}p_v}{\mathrm{d}t} = -C_p p_v n_t + (e_p^t + e_p^o)(N_t - n_t) + \eta \alpha I \tag{3.19}$$

$$\frac{\mathrm{d}n_t}{\mathrm{d}t} = -(C_p p_v + C_n n_c + e_p^t + e_n^t + e_p^o + e_n^o) n_t + (e_p^t + e_p^o + C_n n_t) N_t \,.$$

In the steady state regime and in the thermal equilibrium time derivations are null and a homogenous system of algebraic equations is received.

The neutrality boundary condition says that the number of vacancies in the valence band is equaled to the number of excited electrons at the trap level and in the conduction band

$$n_c + N_t f_t = p_v \tag{3.20}$$

and especially for the thermal equilibrium

$$n_{c0} + N_t f_{t0} = p_{v0} \,. \tag{3.21}$$

Substraction of both conditions gives concentration excesses

$$\Delta n_c = n_c - n_{c0}, \ \Delta p_v = p_v - p_{v0}, \ \Delta n_t = n_t - n_{t0} \tag{3.22}$$

deviated from the equilibrium but still in the steady state

$$\Delta n_c + \Delta n_t = \Delta p_v \,. \tag{3.23}$$

When the trap concentration is small compared to the electron concentration in the conduction band[4], then the deviation Δn_t can be neglected and $\Delta n_c = \Delta p_v$. If the optical emissions from the trap level are excluded from the system (3.19) then one can easily eliminate n_t and get an important formula

$$N_t \frac{C_n C_p (n_c p_v - n_{c1} p_{v1})}{C_p (p_v + p_{v1}) + C_n (n_c + n_{c1})} = \eta \alpha I \,. \tag{3.24}$$

Whilst the left hand side of (3.24) describes electron recombination R from the conduction band, the right side represent band-to-band carrier generation. Principally, the right side might be replaced with any other means of constant generation G.

After substituting the concentrations n_c, p_v from (3.22) and comparing with the steady-state solution $\Delta n_c = G\tau$ of a general equation $\mathrm{d}\Delta n_c / \mathrm{d}t = G + R$ where $R = -\Delta n_c / \tau$, we obtains the Shockley-Read formula for the carrier lifetime τ

$$\tau = \tau_{p0} \frac{n_{c0} + n_{c1} + \Delta n_c}{n_{c0} + p_{v0} + \Delta n_c} + \tau_{n0} \frac{p_{v0} + p_{v1} + \Delta n_c}{n_{c0} + p_{v0} + \Delta n_c} \,. \tag{3.25}$$

---

[4]i.e. $\Delta n_t \ll \Delta n_c$ or even $N_t \ll \Delta n_c$

Here, new auxiliary lifetimes are defined as

$$\tau_{p0} = \frac{1}{C_p N_t} \text{ and } \tau_{n0} = \frac{1}{C_n N_t} \tag{3.26}$$

representing the limit situations when the trapping level is fully occupied by electrons, respectively when the level is entirely empty.

Trap vs. recombination center

Electron recombination 4 and electron detrapping 1 are competing process (Fig. 3.2). Their mutual ratio determines the nature of the center. When the emission of electron from the center to the conduction band prevails over the emission to the valence band, then we talk about an electron trap, in the opposite case the center has a recombination character. For holes equivalent rival processes are 2 and 4.

Let us suppose a single electron occupying a center. Probability of its emission to the conduction band is $e_n^t = C_n n_{c1}$ according to (3.15), whereas the probability of the emission to the valence band is after (3.10) $C_p p_v$. If the ratio $k_n = C_p p_v / C_n n_{c1}$ fulfils the criterion $k_n > 1$, then the center behaves as an electron recombination center. Contrary, when $k_n > 1$, the center is a trap. Analogical ratio could be constructed for holes $k_p = C_n n_c / C_p p_{v1}$ with the same requirements for trap characterization.

Figure 3.3: Demarcation lines characterizing the nature of centers.

Moreover, we might introduce two fictional levels so called demarcation lines

$$
\begin{aligned}
\mathsf{E}_{Dn} &= \mathsf{F}_n + k_B T \ln \frac{p_{t0}}{n_{t0}}, \\
\mathsf{E}_{Dp} &= \mathsf{F}_p + k_B T \ln \frac{p_{t0}}{n_{t0}}
\end{aligned}
\tag{3.27}
$$

where F_n, F_p denote the quasi Fermi levels for electrons and holes. Demarcation lines divide the gap into the three regions (Fig. 3.3). Trap levels positioned between E_{Dn} and E_{Dp} are recombination centers. Levels spanned between E_{Dn} and E_c represent electron traps and levels within E_v and E_{Dn} are traps for holes. The classification is only approximative and convenient especially when the capture-cross sections of electrons vs. holes do not differ much.

4. Theory of Pockels electro-optic effect in zinc-blende structure

4.1 Optical index ellipsoid

Anisotropy of light propagation in solids is a consequence of the tensor nature of refractive index. In isotropic non-absorbing medium, the relation between the permittivity and the refractive index is trivially $\varepsilon = n^2$. For case of anisotropic solids, the situation is rather complicated. Permitivity is described by symmetrical two-rank tensor represented by a square matrix

$$\varepsilon = \begin{pmatrix} \varepsilon_{11} & \varepsilon_{12} & \varepsilon_{13} \\ \varepsilon_{21} & \varepsilon_{22} & \varepsilon_{23} \\ \varepsilon_{31} & \varepsilon_{32} & \varepsilon_{33} \end{pmatrix}. \tag{4.1}$$

In the principal axis coordinate system the permittivity tensor is purely diagonal. Such reference frame exists for each regular symmetrical matrix. In dualism, electric impermittivity η may be introduced as a reciprocal property to permittivity. Impermittivity tensor is not inverse to the matrix of dielectric constants but it is constructed as $\eta_{ij} = \frac{1}{\varepsilon_{ij}}$. Especially, in the principal axis frame the reciprocal matrix and inverse matrix coincide. Permittivity as a material property that converts the electric field[1] to the electric displacement

$$\boldsymbol{D}^w = \varepsilon \boldsymbol{E}^w \text{ respectively } D_i^w = \sum_j \varepsilon_{ij} E_j^w. \tag{4.2}$$

Electric energy density has the form in the principal frame

$$w_e = \frac{1}{2} \boldsymbol{E}^w . \boldsymbol{D}^w = \frac{1}{2} \sum_j \varepsilon_{jj} E_j^w E_j^w = \frac{1}{2} \sum_j \frac{D_j^w D_j^w}{\varepsilon_{jj}}. \tag{4.3}$$

If the last expression is rewritten explicitly in the form of refractive indices

$$2w_e = \frac{D_{w,x}^2}{n_x^2} + \frac{D_{w,y}^2}{n_y^2} + \frac{D_{w,z}^2}{n_z^2} \tag{4.4}$$

we obtain equation of ellipsoid. To receive its canonical form

$$\frac{x^2}{n_x^2} + \frac{y^2}{n_y^2} + \frac{z^2}{n_z^2} = 1 \tag{4.5}$$

---

[1]When we talk about the electric field of a propagating electro-magnetic wave, we write suffix w, i.e. $\mathbf{E}^w$, resp. $\mathbf{D}^w$.

we assume formal coordinates $x = D_x^w/\sqrt{2w_e}, y = D_y^w/\sqrt{2w_e}, z = D_z^w/\sqrt{2w_e}$. Refractive index ellipsoid is also called optical indicatrix. Semi-axes of the ellipsoid represent refractive indices.

Geometrical construction based on the intersection of the optical indicatrix and a plane gives the clue for determination of the phase velocity (Fig. 4.1). Imagine a normal wave vector of propagation $\boldsymbol{s}$ acting in phase development $i(k\boldsymbol{sr} - \omega t)$ and a plane perpendicular to this direction.[2] Plane section of the optical indicatrix is generally an ellipse. Length of the ellipse semi-axes are equal to the refractive indices of polarization modes that wave propagates through the solid. Directions of electric displacement in fundamental modes are parallel to the semi-axes of the ellipses.

Figure 4.1: Index ellipsoid and construction of two orthogonal vibration modes of $\boldsymbol{D}$ belonging to the wave normal direction $\boldsymbol{s}$.
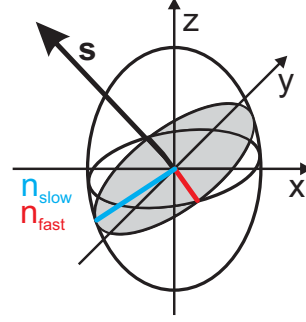
Analogically, the optical indicatrix might be assembled from the impermittivity tensor in the same manner in an arbitrary reference system

$$\eta_{11}^0\, x^2 + \eta_{22}^0\, y^2 + \eta_{33}^0\, z^2 + 2\eta_{12}^0\, xy + 2\eta_{13}^0\, xz + 2\eta_{23}^0\, yz = 1\,. \tag{4.6}$$

Zero superscript emphasizes that the solid is not subjected to conditions resulting in the change of impermittivity. From symmetry of the impermittivity tensor we substitute η_{21} with η_{12}, η_{31} with η_{13}, and η_{32} with η_{23}.

4.2 Formalism of the Pockels effect

After exertion to the external field[3] $\boldsymbol{E} = (E_x, E_y, E_z)$, impermittivity is altered due to the crystal deformation or mutual displacement of crystal sublattices. The variation of a impermittivity element may be developed in the Taylor series

$$\eta_{ij} = \eta_{ij}\Big|_{\boldsymbol{E}=0} + \sum_{k=1}^{3} \frac{\partial \eta_{ij}}{\partial E_k}\Big|_{\boldsymbol{E}=0} E_k + \frac{1}{2}\sum_{k=1}^{3}\sum_{l=1}^{3} \frac{\partial \eta_{ij}}{\partial E_k E_l}\Big|_{\boldsymbol{E}=0} E_k E_l + \ldots \tag{4.7}$$

where $\eta_{ij}|_{\boldsymbol{E}=0}$ coincides with zero-field statical values from (4.6). Optical indicatrix for electrostatically distorted crystal gets the form

$$\eta_{11}(\boldsymbol{E})\, x^2 + \eta_{22}(\boldsymbol{E})\, y^2 + \eta_{33}(\boldsymbol{E})\, z^2 + 2\eta_{12}(\boldsymbol{E})\, xy + 2\eta_{13}(\boldsymbol{E})\, xz + 2\eta_{23}(\boldsymbol{E})\, yz = 1\,. \tag{4.8}$$

---

[2]More explicitly, $\boldsymbol{s}$ is the direction of a propagating wave and k denotes the absolute value of its wave-vector.

[3]The external field that stands for the Pockels effect is labeled $\boldsymbol{E}$.

Pockels effect describes restriction to the linear term in the Taylor expansion of distorted impermittivity

$$\Delta\eta_{ij} = \eta(\boldsymbol{E})_{ij} - \eta_{ij}^0 = \sum_{k=1}^{3} \frac{\partial \eta_{ij}}{\partial E_k}\bigg|_{\boldsymbol{E}=0} E_k = \sum_{k=1}^{3} R_{ijk} E_k \,. \tag{4.9}$$

Pockels coefficients R_{ijk} in the three-suffix notation fully characterize the disturbance of impermittivity in linear approximation. They constitute three-rank tensor of 27 components invariant to exchange of i and j due to the symmetry of η. Indicatrix then depends upon E-field

$$\sum_{i,j} \eta_{ij}^0 x_i x_j + \sum_{i,j} \Delta\eta_{ij}(\boldsymbol{E}) \, x_i x_j = \sum_{i,j} \eta_{ij}^0 x_i x_j + \sum_{i,j} \sum_k R_{ijk} E_k \, x_i x_j = 1 \tag{4.10}$$

where naturally $x_1 = x$, $x_2 = y$, $x_3 = z$. In order to reduce the number of dependent components R_{ijk}, transformation to two-suffix notation r_{pq} is welcome

$$
\begin{aligned}
\Delta\eta_1(\boldsymbol{E}) &= \eta_1(\boldsymbol{E}) - \eta_1^0 &=& r_{11}E_x + r_{12}E_y + r_{13}E_z \\
\Delta\eta_2(\boldsymbol{E}) &= \eta_2(\boldsymbol{E}) - \eta_2^0 &=& r_{21}E_x + r_{22}E_y + r_{23}E_z \\
\Delta\eta_3(\boldsymbol{E}) &= \eta_3(\boldsymbol{E}) - \eta_3^0 &=& r_{31}E_x + r_{32}E_y + r_{33}E_z \\
\Delta\eta_4(\boldsymbol{E}) &= \eta_4(\boldsymbol{E}) - \eta_4^0 &=& r_{41}E_x + r_{42}E_y + r_{43}E_z \\
\Delta\eta_5(\boldsymbol{E}) &= \eta_5(\boldsymbol{E}) - \eta_5^0 &=& r_{51}E_x + r_{52}E_y + r_{53}E_z \\
\Delta\eta_6(\boldsymbol{E}) &= \eta_6(\boldsymbol{E}) - \eta_6^0 &=& r_{61}E_x + r_{62}E_y + r_{63}E_z
\end{aligned}
\tag{4.11}
$$

instead of more extensive and less comfortable

$$
\begin{aligned}
\Delta\eta_1(\boldsymbol{E}) &= \eta_{11}(\boldsymbol{E}) - \eta_{11}^0 &=& R_{111}E_x + R_{112}E_y + R_{113}E_z \\
\Delta\eta_2(\boldsymbol{E}) &= \eta_{22}(\boldsymbol{E}) - \eta_{22}^0 &=& R_{221}E_x + R_{222}E_y + R_{223}E_z \\
\Delta\eta_3(\boldsymbol{E}) &= \eta_{33}(\boldsymbol{E}) - \eta_{33}^0 &=& R_{331}E_x + R_{332}E_y + R_{333}E_z \\
\Delta\eta_4(\boldsymbol{E}) &= \eta_{23}(\boldsymbol{E}) - \eta_{23}^0 &=& R_{231}E_x + R_{232}E_y + R_{233}E_z \\
\Delta\eta_4(\boldsymbol{E}) &= \eta_{32}(\boldsymbol{E}) - \eta_{32}^0 &=& R_{321}E_x + R_{322}E_y + R_{323}E_z \\
\Delta\eta_5(\boldsymbol{E}) &= \eta_{13}(\boldsymbol{E}) - \eta_{13}^0 &=& R_{131}E_x + R_{132}E_y + R_{133}E_z \\
\Delta\eta_5(\boldsymbol{E}) &= \eta_{31}(\boldsymbol{E}) - \eta_{31}^0 &=& R_{311}E_x + R_{312}E_y + R_{313}E_z \\
\Delta\eta_6(\boldsymbol{E}) &= \eta_{12}(\boldsymbol{E}) - \eta_{12}^0 &=& R_{121}E_x + R_{122}E_y + R_{123}E_z \\
\Delta\eta_6(\boldsymbol{E}) &= \eta_{21}(\boldsymbol{E}) - \eta_{21}^0 &=& R_{211}E_x + R_{212}E_y + R_{213}E_z \,.
\end{aligned}
\tag{4.12}
$$

Two-suffix Pockels coefficients are easily representable with a 6×3 matrix. For instance, indices xy and yx are reduced to a single index 6, etc. The same suffix reduction was done for the symmetrical impermittivity tensor. Ergo, two-rank impermittivity tensor might be written as a six component vector η_{1-6} or as the symmetrical matrix $\eta_{3 \times 3}$.

Relation (4.9) describing the Pockels effect is then clearly expressed as a matrix product

$$
\begin{pmatrix}
\Delta\eta_1 \\
\Delta\eta_2 \\
\Delta\eta_3 \\
\Delta\eta_4 \\
\Delta\eta_5 \\
\Delta\eta_6
\end{pmatrix}
=
\begin{pmatrix}
r_{11} & r_{12} & r_{13} \\
r_{21} & r_{22} & r_{23} \\
r_{31} & r_{32} & r_{33} \\
r_{41} & r_{42} & r_{43} \\
r_{51} & r_{52} & r_{53} \\
r_{61} & r_{62} & r_{63}
\end{pmatrix}
\begin{pmatrix}
E_x \\
E_y \\
E_z
\end{pmatrix}.
\tag{4.13}
$$

In other words the Pockels effect, shortly written as $\Delta\eta = r\boldsymbol{E}$, says that the change in impermittivity is directly proportional to the external field through the coefficients r_{ij} ordered in matrix r.

Index ellipsoid in the two-suffix notation has the form

$$
\begin{aligned}
(\eta_{11}^0 + \Delta\eta_1)\,x^2 + (\eta_{22}^0 + \Delta\eta_2)\,y^2 + (\eta_{33}^0 + \Delta\eta_3)\,z^2 + \\
+ (2\eta_{23} + \Delta\eta_4)\,yz + (2\eta_{13} + \Delta\eta_5)\,xz + (2\eta_{12} + \Delta\eta_6)\,xy \quad = 1\,.
\end{aligned}
\tag{4.14}
$$

Symmetry operations significantly reduce the number of independent and non-vanishing Pockels coefficients. The Pockels matrix for crystals of the zinc-blende structure gains the simple appearance

$$
r =
\begin{pmatrix}
0 & 0 & 0 \\
0 & 0 & 0 \\
0 & 0 & 0 \\
r_{41} & 0 & 0 \\
0 & r_{41} & 0 \\
0 & 0 & r_{41}
\end{pmatrix}.
\tag{4.15}
$$

The derivation of coefficients is outlined in the appendix A.

4.3   Electro-optically induced uniaxial refraction

At this moment we are equipped with the specific form of η and r for zinc-blende structure in the crystallographic basis. Let us approach to the further derivation of the index ellipsoid equation. After expansion of the product $r.\boldsymbol{E} = (0, 0, 0, r_{41}E_x, r_{41}E_y, r_{41}E_z)^\mathsf{T}$ and substituting $\Delta\eta$ in (4.14), the following equation is acquired

$$
\frac{x^2}{n_0^2} + \frac{y^2}{n_0^2} + \frac{z^2}{n_0^2} + 2r_{41}(E_x\,yz + E_y\,xz + E_z\,xy) = 1\,.
\tag{4.16}
$$

Equation of the ellipsoid might be aesthetically written down via matrix multiplication $\boldsymbol{x}^{\mathsf{T}} M \boldsymbol{x} = 1$ or explicitly

$$
\begin{pmatrix} x & y & z \end{pmatrix}
\begin{pmatrix}
\dfrac{1}{n_0^2} & r_{41}E_z & r_{41}E_y \\[2mm]
r_{41}E_z & \dfrac{1}{n_0^2} & r_{41}E_x \\[2mm]
r_{41}E_y & r_{41}E_x & \dfrac{1}{n_0^2}
\end{pmatrix}
\begin{pmatrix} x \\ y \\ z \end{pmatrix} = 1 \,.
\tag{4.17}
$$

Let us restrict the electric vector to point in direction (111), i.e. $\boldsymbol{E} = E\frac{1}{\sqrt{3}}(1,1,1)^{\mathsf{T}}$. This is equivalent to the statement that a crystal facet is cut as (111) plane in Miller notation and the E-field is applied perpendicularly to the facet. Since, the matrix M is deviated only with a single parameter - absolute value of the electric vector

$$
\begin{pmatrix} x & y & z \end{pmatrix}
\begin{pmatrix}
\dfrac{1}{n_0^2} & r_{41}E/\sqrt{3} & r_{41}E/\sqrt{3} \\[2mm]
r_{41}E/\sqrt{3} & \dfrac{1}{n_0^2} & r_{41}E/\sqrt{3} \\[2mm]
r_{41}E/\sqrt{3} & r_{41}E/\sqrt{3} & \dfrac{1}{n_0^2}
\end{pmatrix}
\begin{pmatrix} x \\ y \\ z \end{pmatrix} = 1 \,.
\tag{4.18}
$$

To find out semi-axes of ellipsoid (4.18), M matrix needs to be transformed to principal axes where the deviated M is diagonal. The proposed operation will bring out directions of canonical vibration modes as well as effective refractive indices for respective polarizations. Strictly speaking, we look for eigenvalues and eigenvectors of M. Eigenvalues are roots of the determinant equation of secular matrix

$$
M_N =
\begin{pmatrix}
\dfrac{1}{n_0^2} - \dfrac{1}{N^2} & r_{41}E/\sqrt{3} & r_{41}E/\sqrt{3} \\[2mm]
r_{41}E/\sqrt{3} & \dfrac{1}{n_0^2} - \dfrac{1}{N^2} & r_{41}E/\sqrt{3} \\[2mm]
r_{41}E/\sqrt{3} & r_{41}E/\sqrt{3} & \dfrac{1}{n_0^2} - \dfrac{1}{N^2}
\end{pmatrix}
=
\begin{pmatrix}
a & b & b \\
b & a & b \\
b & b & a
\end{pmatrix}
\tag{4.19}
$$

where $a = 1/n^2 - 1/N^2$ and $b = r_{41}E/\sqrt{3}$ were chosen for shorter notation. Determinant equation of the third order in variable a is stated as

$$
a^3 - 3ab^2 + 2b^3 = 0
\tag{4.20}
$$

with roots $a_1 = -2b$ and two-fold $a_{2,3} = b$. Substituting from definition of a and b, we obtain the net form of roots

$$
\begin{aligned}
N_1 &= \frac{n_0}{\sqrt{1 + 2n_0^2 r_{41}E/\sqrt{3}}} \quad \simeq n_0 - \frac{1}{\sqrt{3}} n_0^3 r_{41}E \\[3mm]
N_{2,3} &= \frac{n_0}{\sqrt{1 - n_0^2 r_{41}E/\sqrt{3}}} \quad \simeq n_0 + \frac{1}{2\sqrt{3}} n_0^3 r_{41}E \,.
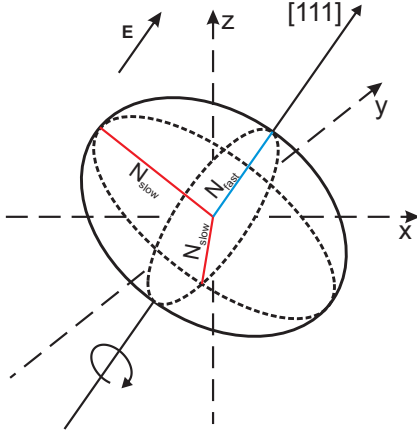\end{aligned}
\tag{4.21}
$$

Figure 4.2: Shape of the index ellipsoid under exertion to the electric field $\boldsymbol{E} = E\frac{1}{\sqrt{3}}(111)$. Originally, the index ellipsoid was spherical for solids of zinc-blende structure. E-field application causes prolongation in transverse direction and shortening in longitudinal direction ($r_{41} > 0$). Ellipsoid has axis of revolution in (111). Thereby all modes vibrating along the biased field run faster with refraction index N_{fast}. The modes vibrating perpendicularly to the electric field propagate with refraction index N_{slow}.

Back-substitution of roots a_1 and $a_{2,3}$ to the secular matrix (4.19) provides projective matrices to the irreducible subspaces specified by eigenvalues

$$P_{a_1} = \begin{pmatrix} -2b & b & b \\ b & -2b & b \\ b & b & -2b \end{pmatrix}, \; P_{a_2, a_3} = \begin{pmatrix} b & b & b \\ b & b & b \\ b & b & b \end{pmatrix}. \tag{4.22}$$

The rank of P_{a_1} equals two and rank of $P_{a_{2,3}}$ is one. Complement to $\mathbb{R}^3$ gives the number of vectors generating the subspace. Thus, the generator of subspace P_{a_1} is strictly $\frac{1}{\sqrt{3}}(111)^{\mathsf{T}}$. However, generators of subspace P_{a_2, a_3} are not unique. They create an orthogonal complementary subspace to $\mathbb{R}^3$ space. For instance, one non-orthogonal option could be a couple $\frac{1}{\sqrt{2}}(01\bar{1})^{\mathsf{T}}$, $\frac{1}{\sqrt{2}}(1\bar{1}0)^{\mathsf{T}}$. Different couples might be suggested as $\frac{1}{\sqrt{2}}(01\bar{1})^{\mathsf{T}}$, $\frac{1}{\sqrt{6}}(\bar{2}11)^{\mathsf{T}}$ that together with $\frac{1}{\sqrt{3}}(111)^{\mathsf{T}}$ produce an orthogonal triplet.[4]

As a result, the crystal becomes negatively uniaxial with the fast axis in direction of the applied E-field and the corresponding refractive index is N_1. Slow axes are perpendicular to the fast one having refractive index N_2. In fact, polarization in direction parallel to the electric vector propagates faster then an arbitrary polarization mode at right angle to the external E-field. Initially spherical indicatrix turns into ellipsoid of revolution about the direction of electric vector (Fig. 4.2). Consequently, the solid does not exhibit the longitudinal Pockels effect, i.e. the change of the refractive index of polarization modes belonging to the wave that propagates along the electric vector. All just recapitulated holds only when the electric field is applied in the (111) direction. In all different directions of E-field, the crystal becomes generally biaxial and the determination of the phase velocity complicates.

To estimate the magnitude of the change of refractive index in CdTe, we suppose $n_0 = 2.8$. Pockels coefficient r_{41} is spanned (5.5-6.8) $\times 10^{-9}$ mm/V for $\lambda_0 = $ 1-5 µm according to miscellaneous sources [23], [21], [24]. Typical experimentally accessible external field is $1\,\mathrm{kV/mm}$. Therefore the electro-optically induced deviation of the refractive index is roughly $\Delta N = r_{41}n_0^3 E = $ (1.2-1.5) $\times 10^{-4}$.

---

[4]We reminds that matrix M_N is still regular, even if two eigenvalues are identical numbers.

5. Pockels effect measurements

5.1 Pockels cell

In the previous section, the fundamentals of crystal anisotropy and linear electro-optical effects for zinc-blende structure were presented. Those facts are necessary to understand the concept of a Pockels cell (Fig. 5.1). Pockels cell is a phase modulator controlled by biased voltage. Vertical polarization is congruent with the direction of the fast axis of propagation whereas horizontal polarization belongs to the slow axis. After passing their optical path in the crystal, the horizontally polarized wave is retarded beyond the vertically polarized wave. Henceforth, a phase shift between these two waves must occur due to the mutual delay. Time delay Δt is directly proportional to the length of optical path L and indirectly proportional to the distinction in phase velocity of the fast $v_F = c/n_F$ and slow $v_S = c/n_S$ axis. The angular frequency of light ω is an invariant of propagation. The phase difference gets a simple form

$$\Delta \delta = \delta_x - \delta_z = \omega \Delta t = \omega \left(\frac{L}{v_S} - \frac{L}{v_F} \right) = \frac{\omega L}{c}(n_S - n_F) = \frac{2\pi}{\lambda_0}\Delta n L \qquad (5.1)$$

where λ_0 is vacuum wavelength. The difference in refractive index depends upon the crystal orientation. For electric field application in the direction (111), $\Delta n = \frac{\sqrt{3}}{2}r_{41}n_0^3$ is given as a difference in principal axis refractive indices (4.21). Final phase modulation for (111) reads

$$\Delta \delta = \frac{2\pi}{\lambda_0}\frac{\sqrt{3}}{2}r_{41}n_0^3 L E \,. \qquad (5.2)$$

A CdTe radiation detector represents an electro-optical cell. External electric field modulates the phase shift. In an ideal case, electric field developed across the crystal sample is bias voltage U divided by the crystal thickness d. So, there is a particular value of voltage U_π

$$U_\pi = \frac{\lambda_0}{\sqrt{3}n_0^3 r_{41}}\frac{d}{L}\,, \qquad (5.3)$$

when the phase shift reaches $\Delta \delta = \pi$. Such voltage is called halfwave voltage.

For analysis of the phase difference, the crossed-polarizer technique could be used. Polarization of light will be described by Jones formalism $\boldsymbol{E} = E_0\boldsymbol{J}\exp[i(\boldsymbol{k}\cdot\boldsymbol{r} - \omega t)]$ where $\boldsymbol{J} = a\hat{\boldsymbol{x}} + b\hat{\boldsymbol{z}}$ is a polarization vector[1]. The first polarizer defines initial polarization state. Its easy-pass direction is $45°$ rotated from the horizontal direction. Diagonal linearly-polarized light $\boldsymbol{J}_P = \frac{1}{\sqrt{2}}(\hat{\boldsymbol{x}} + \hat{\boldsymbol{z}})$ has vertical ($\hat{\boldsymbol{z}}$) and horizontal ($\hat{\boldsymbol{x}}$) components of the same amplitude and phase. After passing through the Pockels cell, horizontal waveform gains relative phase retardation $\Delta\delta$ and polarization changes to generally elliptic state $\boldsymbol{J}_{cell} = \frac{1}{\sqrt{2}}(\hat{\boldsymbol{x}}\exp(-i\Delta\delta) + \hat{\boldsymbol{z}})$. The second polarizer serves as an orthogonal

---

[1]Notation does not require unity of $\boldsymbol{J}$.

Figure 5.1: The concept of Pockels cell and crossed-polarizer analytic technique. Waveforms for vertical and horizontal polarization show distinguished velocities of propagation.
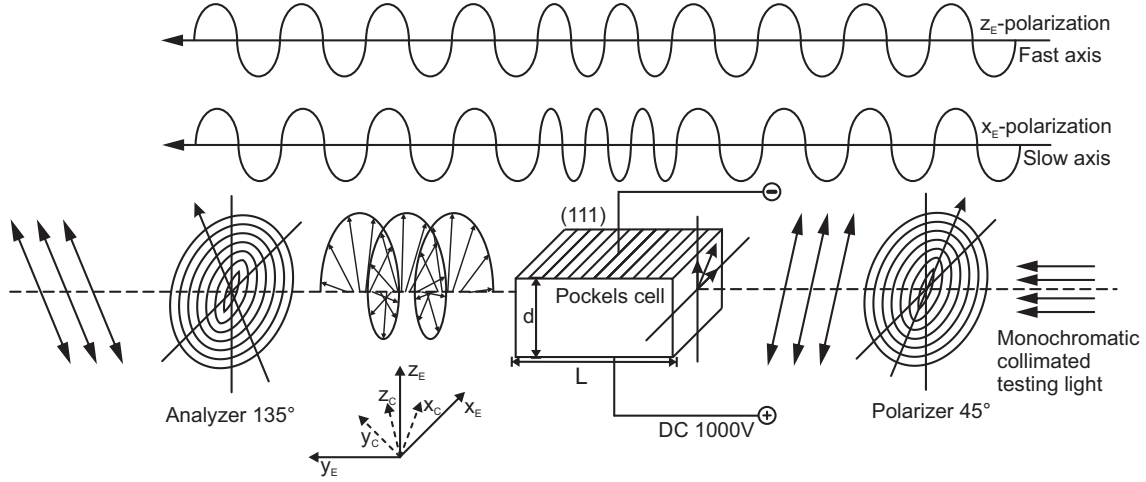
analyser with easy-pass direction of 135° from the horizontal plane. It terminates all polarization states except the projection to its native direction $\boldsymbol{A} = \frac{1}{\sqrt{2}}(-\hat{\boldsymbol{x}} + \hat{\boldsymbol{z}})$. The transmitted projection $\boldsymbol{J}_A$ is given by the dot product

$$\boldsymbol{J}_A = (\boldsymbol{J}_{cell}.\boldsymbol{A}^*)\boldsymbol{A} = \frac{1}{2}(1 - \exp(-i\Delta\delta))\frac{1}{\sqrt{2}}(-\hat{\boldsymbol{x}} + \hat{\boldsymbol{z}}). \quad (5.4)$$

Light intensity as an observable quantity is proportional to the square of E-field amplitude $I \propto |\boldsymbol{J}|^2 E_0^2$. Intensity of the transmitted light for the situation of perpendicular polarizers yields $I_\perp \propto |(1 - \exp(-i\Delta\delta))|^2 |\boldsymbol{J}_A|^2 E_0^2$. Contrary, intensity of transmitted light, in case when both polarizers are parallel and the bias voltage is off, is $I_\parallel \propto |\boldsymbol{J}_P|^2 E_0^2$. Fraction of intensities eliminates the dependence upon arbitrary E_0^2

$$\mathsf{T} = \frac{I_\perp}{I_\parallel} = |(1 - \exp(-i\Delta\delta))|^2 = \frac{1}{2}(1 - \cos\Delta\delta) = \sin^2\frac{\Delta\delta}{2}. \quad (5.5)$$

After substitution of $\Delta\delta$ by the expression (5.2), the final formula for transmittance with E-field perpendicular to plane (111) is obtained

$$\boxed{\mathsf{T} = \frac{I_\perp}{I_\parallel} = \sin^2\left(\frac{2\pi}{\lambda_0}\frac{\sqrt{3}}{4}r_{41}n_0^3 LE\right)}. \quad (5.6)$$

The periodicity of sine in the phase shift reminds formally interference experiments. For null phase shift, entire light is fully diminished by orthogonal polarization filters. For $\pi/2$-multiplication of the phase shift, all light passes through. However, no light coherence is needed and the effect is observed for natural light as well. Dependence of

transmittance upon the E-field could be manifested in a vivid manner

$$\mathsf{T}(x,z) = \sin^2(\alpha E(x,z)) = \sin^2\left(\frac{\pi}{2}\frac{E(x,z)}{E_{\pi/2}}\right) \tag{5.7}$$

where a renormalization factor $\alpha = \frac{\pi}{2}\frac{1}{E_{\pi/2}}$ was introduced.

5.2   Experimental arrangement

Magnitude of Pockels effect is sensitive to a local value of the electric field in the crystal. Electro-optical effect changes refractive indices of orthogonal polarization modes. Transmittance is dictated only by the phase difference of orthogonal polarization modes. Crossed-polarizer technique indicates change in transmittance. All together makes inner electric field distribution a detectable quantity. For an ideal Pockels cell when the electric field is uniform within the inter-electrode space, the transmittance has a constant value all over the crystal. If electric charge is accumulated in the crystal, electric field distribution is modified according to the distributed space charge regions. Hereafter, the effect will be called 'polarization' (of the sample).[2] Consequently, the transmittance is spatially varied and registered as signal information. The Pockels effect is exploited as an indirect tool for investigation of the E-field distribution in a crystal medium.

Experimental arrangement (Fig. 5.2) for electric field measurements consists of a Pockels cell, set of IR polarizers, source of light and a camera [21]. A tungsten lightbulb (*6V*, *3A*) was used as a source of light. Wavelength of 980 nm was extracted from the continuous spectrum by a band-pass filter with FWHM 10 nm and transmittance of 50% at peak maximum. Sub-bandgap light must be selected in order to transmit the CdTe crystal having the gap in the NIR range. A point source was collimated with convex lens. A plane monochromatic wave of intensity 100-500 nW/cm^2 and spot size 2 cm was constructed. The intensity of testing Pockels light needs to be sufficiently high to be detectable by the camera. But the intensity must not exceed the value when it significantly changes the electronic equilibrium.

Figure 5.2: A CdTe detector in an experimental set-up for electric field investigation.
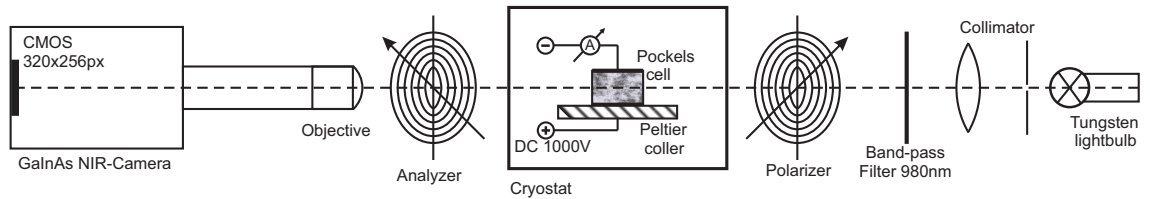
For detection of the transmitted light IR sensitive camera Xenics Xeva was used. The camera has a CMOS pixel array of dimensions 256×320 based on GaInAs. The array is cooled by a Peltier cell down to $240\,\mathrm{K}$ to reduce temperature noise. Camera objective has 20x zoom. Brightness of the camera snapshots is adjusted by integration time[3] with typical values 40-200 ms. This corresponds to framerate 5-25 fps. Camera is connected to PC via USB. Pictures are saved in PNG 8-bit gray-scale format. AD-converter for pixel read-out has $2^{12} = 4096$ channels. Camera exposition is linear to integration time and to the intensity of the Pockels testing light. The objective is focused on the sample surfaces.

Sourcemeter Keithley 2400 with voltage range from -1.1 kV to +1.1 kV was employed as a high-voltage power supply for crystal bias (rise time of $< 1\,\mathrm{ms}$). A CdTe crystal with thin-film metal electrodes was placed on a ceramic plate holder and fixed by silver paint (Fig. 1.2). Ceramic holder ($2.5 \times 2.5\,\mathrm{cm}$) has the gold-layer leads deposited by PVD. Bottom side of the crystal touches directly the gold lead. The top-side contact is connected to the lead via a silver wire of $50\,\mathrm{\mu m}$ diameter. The silver wire is fixed to the top contact by silver paint and soldered to the holder's lead by tin. Thin copper wires connect the holder with the sourcemeter leads.

The holder is staged onto the Peltier cell. Thus, the temperature of the holder is stabilized within $0.1\,\mathrm{K}$ and spanned in 280-325 K. Lower temperature is not recommended under ambient conditions due to air moisture that condenses on the sample's surface. Higher temperature causes irreversible changes in samples due to diffusion of silver or indium from the contacts into the bulk of the crystal. Temperature is measured by platinum $100\,\Omega$ resistance thermometer and regulated by PID controller Eurotherm 3504. Holder and cooler might be placed to a vacuum cryostat to extend the temperature range $200\text{-}325\,K$.

5.3 Acquisition and processing of data

Output of the camera is a grey-scaled image of the crystal (Fig. 5.3). In fact, brightness of the image represents xz array of intensities, i.e. intensity as a function $I(x, z)$ expressed in relative units. Color depth of the image is 8-bits that give relative resolution 1/256=0.4%. Smaller changes in intensity could not be distinguished.

To obtain transmittance according to (5.6) two images need to be taken - a reference image in parallel polarizers adjustment and a signal image in crossed polarizers adjustment when the bias voltage is applied. Their fraction gives the transmittance - the property of our interest. Camera signal never decreases below certain level under absolute darkness conditions due to the temperature noise of the camera. This dark background must be subtracted from the reference and the signal. In crossed-polarizers case with bias voltage off, only pure temp-noise should be received. Nevertheless, po-

---

[3]Or equivalently exposition time.

larizers cannot be ideally adjusted to zero-pass configuration. Furthermore, unwanted light scattering from crystal edges still persists in the crossed-polarizers case. These factors negatively affect the signal. Thus, the backgrounds for parallel and crossed polarizers situations are different.

When the signal in crossed configuration is low, the integration-time for exposition $t_\perp$ is desirable to increase. However, high integration time $t_\parallel$ in parallel configuration leads to saturation of pixels. Therefore, two different integration time periods are chosen. Linearity of the camera exposition to time allows to weigh the image brightness by ratio of the integration times. Whole operation is easily written by equation

$$\mathsf{T}(x,z) = \frac{I_\perp}{I_\parallel} = \frac{I_\perp - I_{bcg,\perp}}{I_\parallel - I_{bcg,\parallel}} \times \frac{t_\parallel}{t_\perp} \,. \tag{5.8}$$

This approach is crucial for correct transmittance analysis.

To evaluate transmittance, images are converted to matrices of numbers and an area of crystal is cropped then $I(x,z)$ is received and utilized by (5.8) The second step

Figure 5.3: Camera photographs of a Au/CdTe/Au cell. Parallel-polarizer image captured in 35 ms integration time and crossed-polarizers images taken in 50 ms. Bright strip below the blocking Au cathode indicates positive space charge region (polarization). Presence of charge gives rise to the electric field that induces stronger Pockels effect. Oppositely, dark region means null E-field. Effect of polarization is amplified with bias voltage. See the fringe effects on the left and right border of the crystal, in contrast to the strip of constant width in the center.
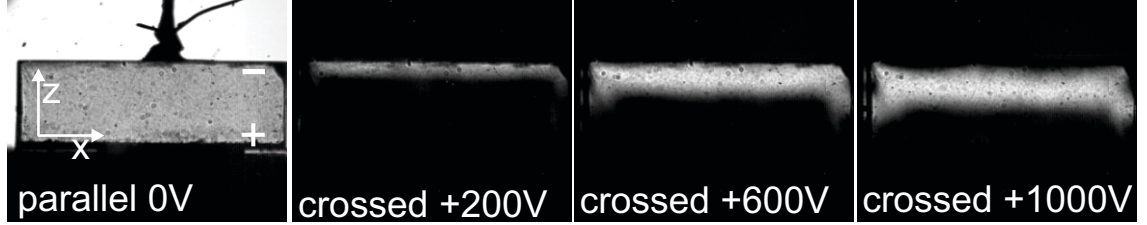
is reconstruction of the E-field $E(x,z)$ from the transmittance $\mathsf{T}(x,z)$. For this purpose an inversion of formula (5.7) is used

$$E(x,z) = \frac{1}{\alpha} \arcsin \sqrt{\frac{I_\perp(x,z)}{I_\parallel(x,z)}}, \quad \alpha = \frac{\sqrt{3}}{2} \frac{\pi}{\lambda_0} r_{41} n_0^3 L \,. \tag{5.9}$$

Electric field in a CdTe detector has one-dimensional distribution within the electrodes due to transitive symmetry in x-direction (Fig. 5.3). Field $E(x,z)$ might be understood as a set of identical profiles $E(z)$ with solely z-dependence. Statistical averaging of profiles in x-direction reduces the noise in E-field profile caused by surface imperfections.

Operation of reconstruction is not ambiguous[4] for two reasons. Square of sine removes the sign of E-field. In other words, negative and positive E-field provides the
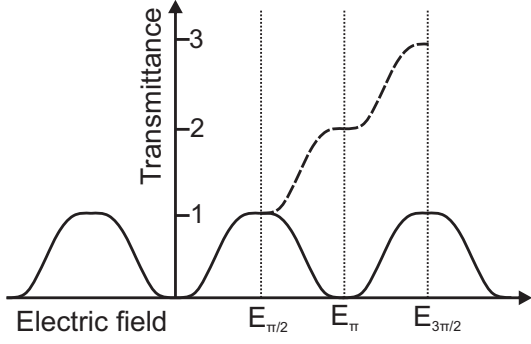
---

[4]bijective

Figure 5.4: Periodicity of transmittance as a function of electric field. In order to get monotonic function of E-field, the transmittance is reconnected each $E_{\pi/2}$ increment according to the formula (5.10).

same transmittance. Further, squared sine is a periodic function with π repetition. Monotonous augmentation of E-field periodically modulates transmittance between 0 and 1 with a quarter-wave voltage increment. Mathematically said, E-field must be reconnected with respect to the boundary conditions at each interval of $\pi/2$-length (Fig. 5.4 and Fig. 5.5)

$$E(z) = \begin{cases} \dfrac{1}{\alpha}\arcsin\sqrt{\mathsf{T}} & \text{for} \quad -E_{\pi/2} \leq E < E_{\pi/2} \\ \dfrac{1}{\alpha}[\arcsin(-\sqrt{\mathsf{T}}) + \pi] & \text{for} \quad E_{\pi/2} \leq E < 3E_{\pi/2}\,, \end{cases} \tag{5.10}$$

if definition $\arcsin(x) \in (-\pi/2, \pi/2)$ for $x \in (-1, 1)$ is considered. Transmitted intensity and reconstructed profiles after reconnection are depicted in Fig. 5.6

Overturn E-field intensity $E_{\pi/2}$ for CdTe for typical values $n_0 = 2.8$, $r_{41} = (5.5\text{-}6.3) \cdot 10^{-12}$ V/m, $\lambda_0 = 980$ nm, $L = 8$ mm, $d = 1.5$ mm is approximately 255-290 V/mm and the renormalization factor α is 5.4-6.2 mm/kV according to the formula (5.3). Such E-field corresponds to quarter-wave voltage 380-440 V for the case of flat undisturbed E-field.

Figure 5.5: Demonstration of different types of E-field developed in a CdTe crystal. The second image reveals effect of polarization when the E-field is spread out below the cathode. Yellow arrow marks the area where the E-field reaches $E_{\pi/2}$ and the transmittance crossed its maximum and begins to fall. The third image depicts even stronger polarization when the E-field even reaches E_π. At that moment transmittance falls to zero and black line is observed(marked by arrow). Last image gives an example of flat E-field where entire crystal is transparent. The trend of field is determined by combination of contact metals (Au/Au or Au/In) and by voltage polarity. Sample B39UA2 with Au/Au contacts.
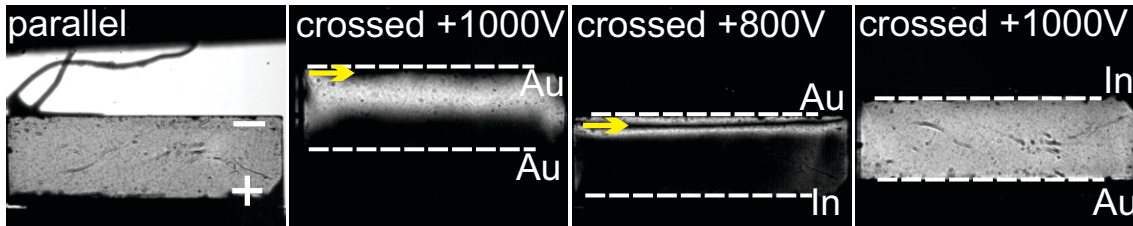
Figure 5.6: Comparison of transmitted intensity versus electric field profiles for bias $+300\,V$, $+1000\,V$. Inter-electrode distance (thickness) of the crystal is $1.5\,mm$ Parallel signal is nearly constant within the sample with drops at the very edges where light is scattered. Parallel and crossed background have similar constant course that equals temperature noise of the camera. Crossed intensity signal shows polarization with approximately linear E-field distribution. When the orientation of crystal does not accurately match to (111), crossed signal never reaches 1 before overturn. This complicates process of the reconnection when the transmittance profile must be firstly rescaled to approach 1 at its maximum.
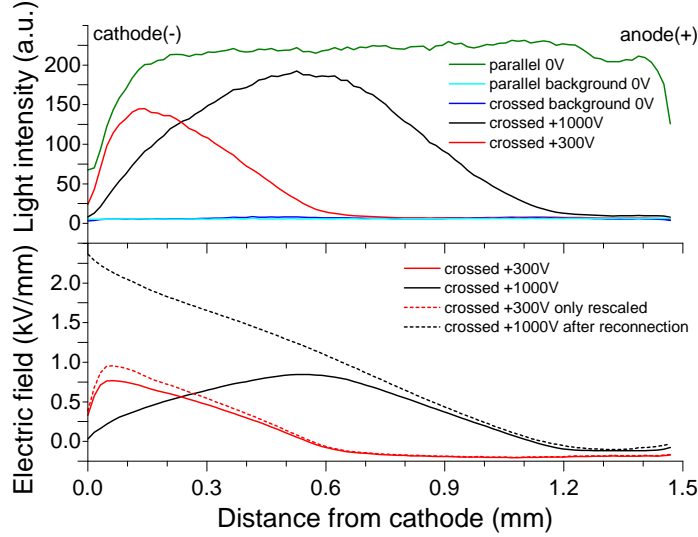
5.4 Practical aspects of the Pockels method and error estimation

In order to reduce measured artefacts and simplify data interpretation, specimen adjustment and preparation must undergo optimizations. Firstly, optical quality of crystal will be discussed. Sides of the crystal block are polished with 0.3-1 μm Al_2O_3 abrasive powder to decrease RMS below 10 nm. Perfect parallelism and orthogonality of planes are highly desirable.

Sharp edges are critical for investigation of effects below electrodes and at metal-crystal interface. Blunt and rounded edges and vertices diffusively disperse light and reduce parallel and crossed signal (Fig. 5.6 light intensity falls at borders). Blunt edges become apparent after subsequent sample treatment, e.g. etching. On the other hand, razor-sharp edges bring about diffraction. Let us suppose the CdTe refractive index $n = 2.8$ at $\lambda = 1\,\mu$m, 10 nm bandwidth of Pockels testing light that corresponds to $\Delta f = 3.12 \cdot 10^{12}$ Hz frequency width. Then the coherence length of the Pockels light is

$$\xi = \frac{c}{n\Delta f} \approx 35\,\mu\text{m}\,. \tag{5.11}$$

If the optical paths of waves differ less than the coherence length then interference

pattern is generally noticeable. This effect is significantly visible at the border-line between the ceramic holder and the crystal. Light is specularly reflected from the holder and interferes with the light passing at the vicinity of the corner. Assuming the sample thickness be 1.5 mm and the region of interest is 1/10 of depth inward the sample, then 150 μm below the electrode is under our attention.

Since IR camera works rather as a microscope, thus perfect collimation of light beam is essential for reasonable objective focusing. For a typical focus length 10 cm between the objective and specimen, theoretical value of resolution 5 μm/px could be reached when the whole specimen's thickness fills completely the field of camera vision. However, full crystal's face images are usually more desirable, thus sampling around 100 px per profile is obtained.

Finite CdTe capacitor dimensions cause fringe effects. Roughly, a CdTe rectangular plate capacitor ($8 \times 5 \times 1.5$ mm) with dielectric constant 10.2 has capacitance 2.41 pF without fringe effects and 3.85 pF including them [29].

Furthermore, surface scratches and damage, visible volume inclusions disturbs smoothness of E-field.

All these effects considerably complicate reproducibility of an experiment. We estimate that acceptable variation of specimen's optical adjustments changes the signal in the range of $10 - 15\%$. Systematic error, variations in adjustments prevails above statistical deviation in processed E-field profiles.

High resistance of the sample is a necessity for the Pockels method. Minimal voltage for measurable signal starts at $100\,V$ when typical values of the rest parameters are supposed $r_{41} = 5.5 \cdot 10^{-12}$V/cm, $L = 10\,\text{mm}, d = 1\,\text{mm}$. If the upper electric current limit is set to $10\,\mu A$ then resistance of $10\,M\Omega$ and Joule dissipation power $1\,mW$ are obtained. Lower resistivity leads to risky high currents and consequent breakdown at voltage above $500\,V$. Fortunately, semi-insulating CdTe samples exhibit dark resistance of few $G\Omega$ with typical current $0.1\,\mu A$ at $100\,V$.

Factors strongly deforming the homogeneity of the transmitted testing light is mechanical strain and stress in the crystal. Different linear expansion coefficients of the contact metals and silver paint fixing the crystal to the holder result in temperature induced stress. Measurements at temperatures lower than $280\,K$ are sometimes affected by stress. Then region for image processing is contracted, usually excluding regions adjacent to the left and right edges.

An illustration of dispersion of the E-field is depicted in Fig. 5.7. Estimation of statistical error proceeds from uncertainty propagation principle applied to formula (5.9). In the beginning, we define elementary deviations

$$\sigma I_\parallel(z) = \sqrt{\langle (I_\parallel(x,z) - \langle I_\parallel(x,z)\rangle_x)^2 \rangle_x}, \quad \sigma I_\perp(z) = \sqrt{\langle (I_\perp(x,z) - \langle I_\perp(x,z)\rangle_x)^2 \rangle_x}$$
(5.12)

according to the framework in Fig. 5.3 and their relative versions $\delta I_\parallel(z) = \sigma I_\parallel(z)/I_\parallel(z)$

and $\delta I_\perp(z) = \sigma I_\perp(z)/I_\perp(z)$. Angled brackets mean averaging in direction of the subscript. Firstly, the expression $\arcsin(\sqrt{I_\perp/I_\parallel})$ is inspected. Its error σ_{arcsin} could be estimated by a sum of quadratic deviations

$$
\begin{aligned}
\sigma_{\mathrm{arcsin}} &= \sqrt{\left(\frac{\partial \arcsin\sqrt{\mathsf{T}}}{\partial I_\parallel}\right)^2 (\sigma I_\parallel)^2 + \left(\frac{\partial \arcsin\sqrt{\mathsf{T}}}{\partial I_\perp}\right)^2 (\sigma I_\perp)^2} \\
&= \left(\frac{\partial \arcsin\sqrt{\mathsf{T}}}{\partial\sqrt{\mathsf{T}}}\right)\left(\frac{\partial\sqrt{\mathsf{T}}}{\partial\mathsf{T}}\right)\sqrt{\left(\frac{\partial\mathsf{T}}{\partial I_\parallel}\right)^2 (\sigma I_\parallel)^2 + \left(\frac{\partial\mathsf{T}}{\partial I_\perp}\right)^2 (\sigma I_\perp)^2} \qquad (5.13) \\
&= \frac{1}{2}\sqrt{\frac{\mathsf{T}}{1-\mathsf{T}}}\sqrt{(\delta I_\parallel)^2 + (\delta I_\perp)^2}\,.
\end{aligned}
$$

The final prefactor converges to zero for $\mathsf{T} \to 0$ and to infinity for $\mathsf{T} \to 1$.

Secondly, let us consider the α coefficient from eq. (5.9) composed of static experimental constants λ_0, r_{41}, n, L. Let us estimate their unsureness as $1.5\%, 10\%, 5\%, 5\%$ in the same order. Their relative impact to renormalization constant $1/\alpha$ is

$$
\delta\frac{1}{\alpha} = \sqrt{(\delta r_{41})^2 + (\delta\lambda_0)^2 + (\delta L)^2 + 3^2(\delta n_0)^2} = 0.19\,. \qquad (5.14)
$$

Heavy dependence upon the refractive index acting in the third power is evident. In the same spirit, overall error of E-field as a product of $1/\alpha$ and arcsin is then

$$
\delta E(z) = \sqrt{\left(\delta\frac{1}{\alpha}\right)^2 + (\delta_{\mathrm{arcsin}(z)})^2}\,. \qquad (5.15)
$$

Transmittance is a relative optical measurement. The IR camera does not serve as an intensity standard. But, evaluated values of the E-field are in absolute units due to constant α after consideration of E-field sign and reconnection. Although the Pockels method offers local two-dimensional resolution due to the camera, resultant profiles undergo averaging. The information about E-field distribution in the third dimension (L) parallel with the ray of the testing light is unavailable. The total phase shift received between the beginning and the end of the Pockels cell has an integral character

$$
\Delta\delta(E(x,z)) = \int_0^L \mathrm{d}[\Delta\delta(E(x,y,z))] \qquad (5.16)
$$

and thus the only projection to the xz plane is observed.[5]

Pockels method is a noninvasive and nondestructive way of inspecting internal E-field. However, its serious drawback is reliance upon the precision of optical adjustment.

Electric field applied only in crystal orientation (111) ensures uniaxiality of the stressed crystal. Other arbitrary crystal cuts are submitted to biaxial description (see appendix B). Transmittance never reaches one and (111) procedure of the data analysis is only approximative.

---

[5] Here, δ means phase development and E is the scalar value of the internal electric field in vertical direction in the relation to the set-up in Fig. 5.1.

Figure 5.7: Illustration of statistical uncertainty in the processing of E-field profiles. Photographs show positions of line segments where the cross-sections were made. Average vertical E-field profile with error bars is computed from the region restricted by vertical white lines. Arrows mark positions of horizontal profiles that are plotted on the right. Histogram below shows distributions around average values at fixed depths of the crystal (bin size 0.015 kV/mm). Applied voltage 400 V.
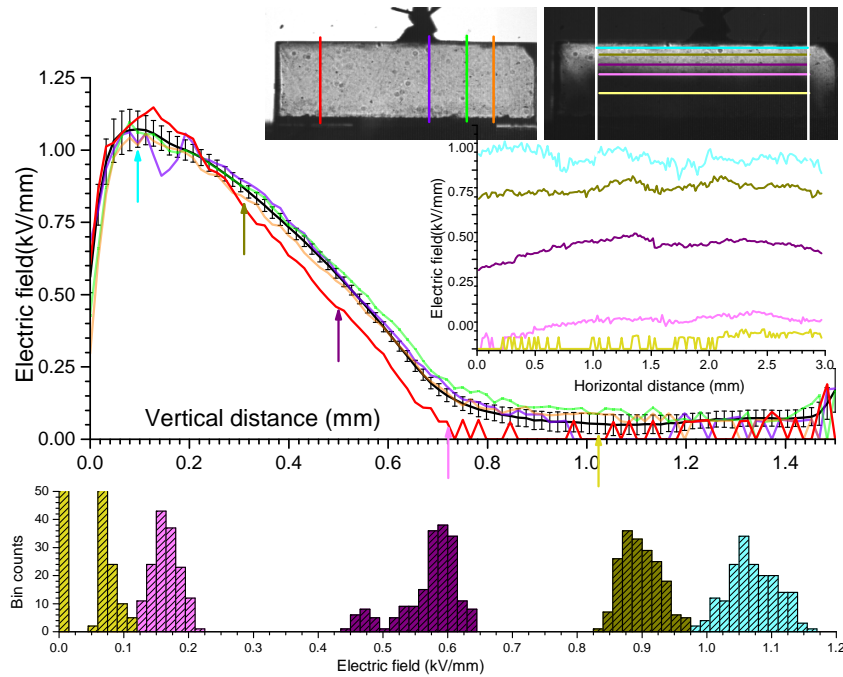
Variation of experimental parameters such as voltage, temperature, time, illumination enables to study the E-field in dependence upon their sweeps. This is the subject of the following chapters. Combination of contact metals can even influence the nature of the E-field. Engagement of other methods as current-voltage and Hall measurements provides a detailed insight to the carrier transport in a CdTe detector.

6. Experimental results by Pockels method

6.1 Observing polarization at Au/CdTe/Au structure

In the previous chapter we have described the technique that leads to the reconstruction of E-field profiles. The electric field varies transmittance through the Pockels effect. The electric profile is a response to an internal mechanisms that will be the next goal of our survey. Particularly, we are interested in the effect of charge polarization in a detector. We know that the ideal course of E-field in a crystal with side contacts should be constant equaled $E = U/d$ where U denotes the bias and d marks the detector thickness.

The presence of deep levels causes the different trend of the E-field. Additional electronic states in the proximity of the Fermi level offer an opportunity for their easy occupation and ionization. Charge confined at deep centers changes the E-intensity and consequently the electric potential V via the Poisson equation

$$-\frac{\mathrm{d}^2 V}{\mathrm{d}z^2} = \frac{\mathrm{d}E}{\mathrm{d}z} = \frac{\varrho(z)}{\varepsilon} \tag{6.1}$$

where z denotes the distance between electrodes starting at the cathode and ϱ stands for space charge density.

In the picture Fig. 6.1, an energy band diagram is depicted describing the formation of space charge under the bias. In the thermal equilibrium, the Fermi level lies above or close to the level with deep centers. The exact position of the FL is dependent upon temperature and concentration of free carriers. Nevertheless, it might be considered

Figure 6.1: Schematic band diagram of a CdTe detector in the thermal equilibrium and under the bias. Gold contacts make semiconductor's bands curved upwards. In equilibrium the deep level is occupied with electrons since the Fermi level lies above. Bias causes a linear ascend of bands within electrodes. At the metal-semiconductor interface, the deep level crosses the quasi Fermi level and electrons are detrapped from centers. Injection of electrons is blocked due to the rise of the barrier. Oppositely, collection of holes is reinforced as the barrier is lowered at the anode.
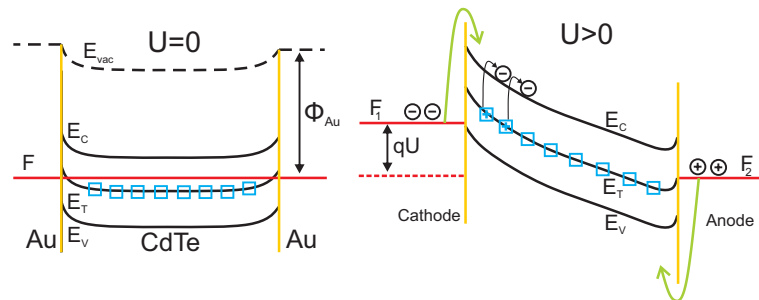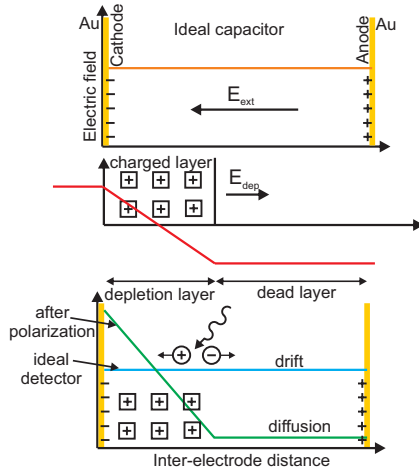
Figure 6.2: An ideal electric field in a CdTe detector is identical with the field developed within the electrodes of a capacitor. De-occupation of deep centers forms a depleted layer of uniform positive charge. Deformed electric profile is created by the superposition of initial external E-field E_{ext} and depolarization field E_{dep}. E-field splits photogenerated electron-hole pair then the carriers move to attracting electrodes. Their motion is driven by drift or by diffusion for the polarized detector.

that traps are neutral. At the metal-semiconductor (M-S) interface bands are tilted due to the Schottky effect. The magnitude and the width of the bending relies on two factors - concentration of the level and the difference of work functions $\Delta\Phi$ between a metal and CdTe. For the pair gold ($\Phi = 5.5\,\mathrm{eV}$) and high resistive CdTe ($\Phi = 5.1 - 5.5\,\mathrm{eV}$), we obtain approximately $\Delta\Phi = 0.2\,\mathrm{eV}$ [28] and gentle upwards bending.

Under bias U the quasi-Fermi level is linearly sloped, intersects the deep level and gets above it. Electrons, that so far occupied neutral centers, leave the centers empty. Immobile centers are accumulated beside the cathode where they form a homogenous positive layer. The band distortion at M-S interface helps to inject or block carriers into the semiconductor. The combination gold-CdTe is rectifying for electrons and easy-pass for holes.

The charged layer produces its own field that acts mostly in the opposite direction to the ideal field (Fig. 6.2). The net field is superposition of the external field E_{ext} and the depolarization field E_{dep}. Outside the charged layer, the field is radically weakened and the so called dead layer is created. Oppositely, inside the charged layer the field receives a typical linearly tilted shape of a triangle and the value of E-field below the cathode is stronger than under ideal circumstances. All free charge carriers disappear and the region is depleted.

The resultant E-field has a significant impact on photogenerated charge collection. An electron-hole pair is standardly separated into two independent carriers that are subsequently attracted by the draining electrodes. Their motion is driven by drift in the regions with strong field. This holds for the depleted layer and an optimal detector. In the dead layer the only motive force remains slow diffusion. Recombination of carriers on their way to an electrode is more probable and performance of the detector is deteriorated. The linear model assuming formation of a homogeneous charged layer is in concordance with experimental curves (Fig. 6.3). Bias voltage U empowers the width of the charged layer w and simultaneously collapses the dead layer $d - w$ in the expense of depletion. If there is some residual field E_{res} and voltage U_{res} developed across the dead layer, we set it constant $E_{res} = U_{res}/(d - w)$ or otherwise $E_{res} = 0$.

Figure 6.3: Electric field dependence upon bias voltage and derived quantities the E-potential and the space charge density. The green line depicts the beginning of the suitable region for evaluation excluding the edge artefacts and define the E-field value below the cathode E_C. Sample BK39UB3, contacts Au/Au, $T = 295\,\mathrm{K}$, state after 1 min.
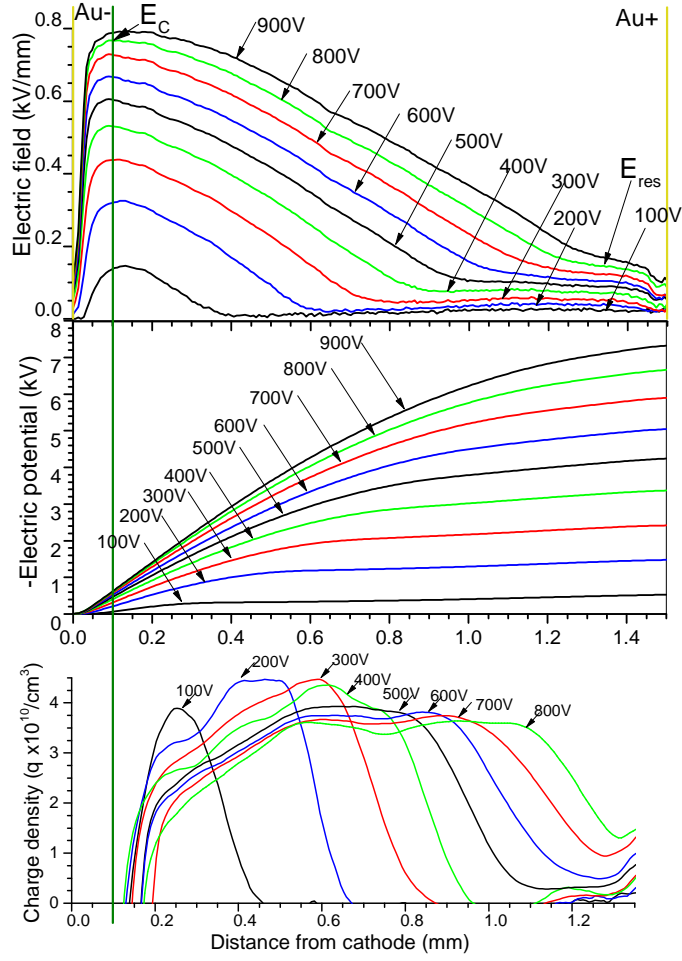
Let us denote the field below electrode E_C, i.e. $E|_{z=0} = E_C$, and the concentration of participating deep levels N_t. The donor sheet has average density of space charge $\varrho = qN_t,\ (q > 0)$. After plugging ϱ into the Poison eq. (6.1) then the first integration yields the E-field and the second one gives the E-potential, explicitly expressed at separated intervals as

$$\varrho(z) = \begin{cases} qN_t & \text{for} \quad z \in (0, w) \\ 0 & \text{for} \quad z \in (w, d) \end{cases} \tag{6.2}$$

$$E(z) = \begin{cases} -\frac{1}{w}(E_C - E_{res})z + E_C & \text{for} \quad z \in (0, w) \\ E_{res} & \text{for} \quad z \in (w, d) \end{cases} \tag{6.3}$$

$$V(z) = \begin{cases} \frac{1}{2w}(E_C - E_{res})z^2 - E_C z & \text{for} \quad z \in (0, w) \\ E_{res}(d - z) - U & \text{for} \quad z \in (w, d)\,. \end{cases} \tag{6.4}$$

The E-potential must fulfill the normalization condition of biased voltage

$$-U = V|_{z=d} - V|_{z=0} = -\int_0^d E(z)\mathrm{d}z \qquad (6.5)$$

where the cathode was set as a ground, $V|_{z=0} = 0$. Straightforwardly, it might be gained from the trivial geometry

$$U = \frac{1}{2}(E_C + E_{res})w + U_{res}\,. \qquad (6.6)$$

Since $E(z)$ is the measured quantity directly from the Pockles experiment, derived quantities $V(z)$, $\varrho(z)$ are determined by the application of inverse operations

$$E(z) \xrightarrow{\frac{\mathrm{d}}{\mathrm{d}z}} \varrho(z) = \varepsilon\frac{\mathrm{d}E}{\mathrm{d}z}\,, \ \ E(z) \xrightarrow{\int \mathrm{d}z} V(z) = -\int_0^z E(z)\mathrm{d}z\,. \qquad (6.7)$$

In other words for the case of the linear model, the density is a step function, the E-potential is quadratic in the depletion region and linear in the dead layer. E-fields are measured in the steady state after 1 min of biasing to U.

6.2   Time evolution of electric field

A formation of the charged layer is not an immediate process. In the following section we will study the time evolution of polarization. For this purpose, the IR camera is operated in a stroboscopic regime and captures images in the adjusted framerate. A typical time resolution does not usually exceed 50 ms because of the limitation given by the minimal camera's integration time. The power supply rises with period less than 1 ms so the voltage profile at sourcemeter's terminals develops in good accuracy as the Heaviside step-function

$$U(t) = \begin{cases} 0 & \text{for} \quad t < 0 \\ U & \text{for} \quad t \geq 0\,. \end{cases} \qquad (6.8)$$

In the figure Fig. 6.4 ascending profiles of the E-field are documented in a sequence lasting 1 min. A charged layer is produced through the two processes. Firstly, deep centers detrap electrons under the cathode resulting in rearrangement of the charge. Secondly, the charged 'wave' is transferred and pressed to the concentrated area below the cathode. Development of the profile proceeds from the initially flat level over the growing pulse to the asymptotic linear shape.

Depopulation of the deep level could be described by a characteristic parameter τ with meaning of average lifetime that electron needs to become detrapped. After all, the width w of the depletion region from (6.2) is no longer time-independent and

similarly the charge density is not stationary but [31]

$$\varrho(x,t) = \begin{cases} qN_t[1 - \exp(-t/\tau)] & \text{for} \quad z \in (0, w(t)) \\ 0 & \text{for} \quad z \in (w(t), d). \end{cases} \qquad (6.9)$$

Furthermore, we assume that the cathodic field E_C grows by the expression [30]

$$E_C(t) = E_{C\infty}[1 - \exp(-t/\tau)] \qquad (6.10)$$

and the residual field in the dead layer is null.

In fact, the last statements claim that the net charge of the depleted zone has the same value and the opposite sign as electrostatic charge Q_C at the supplied cathode. The external field is fully balanced with the field generated by the charged layer. Transient time of electrons at $t \to 0$ for flat E-field in detector is $t_{trans} = d/E\mu = d^2/\mu U$ and numerically 6.5×10^{-8} s under assumptions: thickness $d = 1.5$ mm, mobility $\mu = 1000 \, \text{cm}^2/(\text{V.s})$ and bias $U=350$ V. Electrons are instantly forced to the anode and collected [6].

Since the residual field diminishes, E-profiles simplify to pure triangles with the bounding condition that fixes their area to the constant bias U

$$U = \frac{1}{2}E_C(t)w(t). \qquad (6.11)$$

With the evolution of time, the triangle's width collapses and the height rises

$$E(z,t) = \begin{cases} E_C(t)\left[1 - \dfrac{z}{w(t)}\right] & = E_C(t)\left[1 - \dfrac{E_C(t)z}{2U}\right] & \text{for } z \in (0, w(t)) \\ 0 & & \text{for } z \in (w(t), d). \end{cases} \qquad (6.12)$$

For a point $z > z_C \approx 0$ dependence of field $E(z)$ is not a monotonous function of time but it has more complicated expression coming from (6.12)

$$E(z,t) = E_{C\infty}[1 - \exp(-t/\tau)] - \frac{1}{2U}E_{C\infty}^2[1 - \exp(-t/\tau)]^2 z. \qquad (6.13)$$

To keep things simple we restrict the survey only to the cathode field $E_C(t)$ (see Fig. 6.5).

We arrive to the conclusion that a double exponential formula

$$E_C(t) = E_{C1\infty}[1 - \exp(-(t-t_0)/\tau_1)] + E_{C2\infty}[1 - \exp(-(t-t_0)/\tau_2)] \qquad (6.14)$$

must be employed to fit the data seriously introducing slow and fast components $\tau_1 > \tau_2$ instead of the only one characteristic constant τ used previously. An artificial parameter t_0 has only a technical purpose to synchronize the sourcemeter's trigger and the sequence of images.

Figure 6.4: Time evolution of electric field and derived space charge density in period of 1 min. As time passes, an initial flat field reshapes to the asymptotic polarized state. The green line at x_C depicts cathodic field $E(x_C) = E_C$. In the case of ideal polarization z_C is zero. Sample BK39UA2, contacts Au/Au.
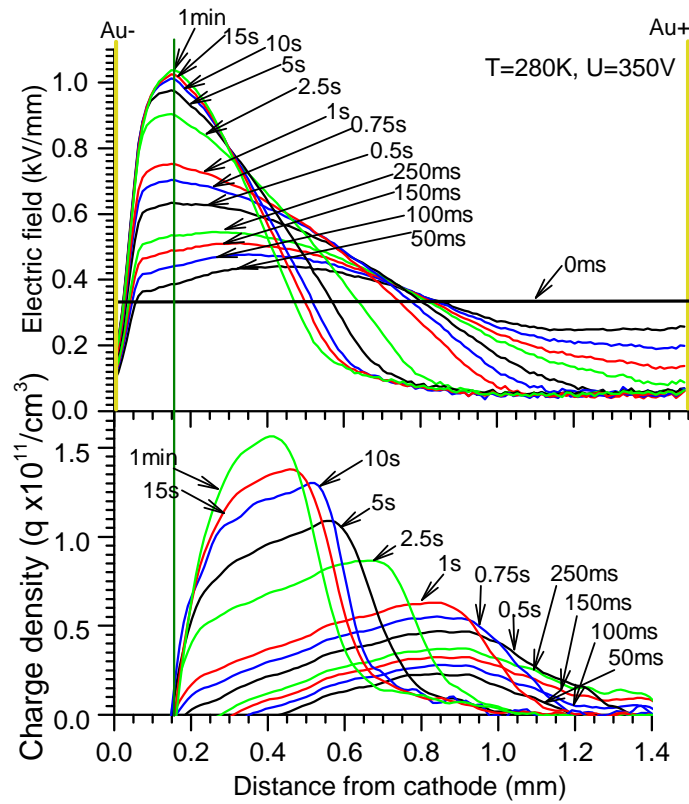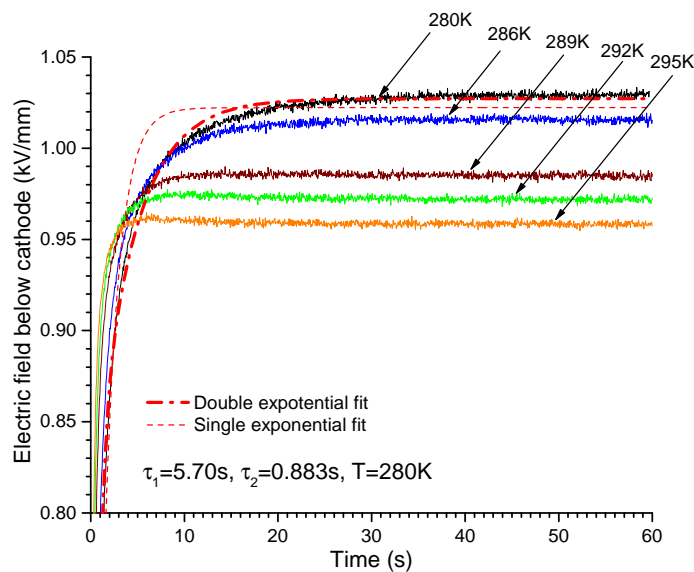
Figure 6.5: Time evolution of the cathode field $E_C(t)$ for various temperatures. A single exponential function does not fit experimental curves correctly, thus an exponential doublet was involved. A slower and stronger polarization is observed for lower temperatures. Sample BK39UA2, contacts Au/Au.

6.3   Temperature effect on polarization

An increase of temperature influences electron population occupying a deep level. The Fermi level F_i of an intrinsic semiconductor linearly increases with temperature by the relation

$$\mathsf{F}_i = -\frac{1}{2}\mathsf{E}_G + \frac{3}{4}k_BT \ln \frac{m_h^*}{m_e^*} \tag{6.15}$$

where the zero is set at the edge of the conduction band and the inequality $m_e^* < m_h^*$ is supposed. When the temperature is elevated, the Fermi level is shifted by a certain constant in the whole crystal. Thereby, deep centers that were depopulated earlier, because they lied above the FL, begin to fill up now. Consequently, the depletion layer of accumulated charge starts to decay and the E-field is depolarized (Fig. 6.6).

Formally, we talk about the thermal emission of carriers from a deep level to the bands [22] that is described by emission rates e_n^t for electrons and e_p^t for holes as

$$
\begin{aligned}
e_n^t &= \frac{1}{\tau_e}(T) = \sigma_e v_e^{th} N_c \exp[-(\mathsf{E}_c - \mathsf{E}_t)/k_BT]\,, \\
e_p^t &= \frac{1}{\tau_h}(T) = \sigma_h v_h^{th} N_v \exp[-(\mathsf{E}_t - \mathsf{E}_v)/k_BT]\,.
\end{aligned}
\tag{6.16}
$$

Here τ is the time constant introduced in section 6.2, σ is an effective cross section of a deep trap, v^{th} is the average thermal velocity, N_c, N_v are the effective density of states at the edge of the conduction and valence band, $\mathsf{E}_c - \mathsf{E}_t, \mathsf{E}_t - \mathsf{E}_v$ are positions of the deep level with respect to the conduction, resp. valence band. The first thermal velocity is determined from the kinetic model

$$v_{e(h)}^{th} = \sqrt{\frac{8k_BT}{\pi m_{e(h)}^*}}\,. \tag{6.17}$$

The emission rate (6.16) could be rewritten in terms of an auxiliary factor [22]

$$A = \frac{2m_{e(h)}^* k_B^2}{\pi^2 \hbar^2} = 3.300 \times 10^{24}\,\mathrm{m}^{-2} \tag{6.18}$$

and a fictional activation energy $\mathsf{E}_A = |\mathsf{E}_{c(v)} - \mathsf{E}_t|$

$$\frac{1}{\tau(T)} = A\sigma T^2 \exp\left(-\frac{\mathsf{E}_A}{k_BT}\right)\,. \tag{6.19}$$

Log-log multiplication transforms (6.19) to the linearized equation

$$\ln(\tau\,T^2) = \frac{\mathsf{E}_A}{k_BT} - \ln(\sigma A)\,. \tag{6.20}$$

Constructing of a linear plot from the temperature dependency of the fitting parametr τ acting in (6.10) in the system of horizontal axis $1/k_BT$ and vertical axis $\ln(\tau T^2)$,

we are able to calculate the energy of the deep level E_t and its effective cross section σ. The slope of the straight line is directly E_t and for the cross section holds $\sigma = \exp(-\text{intercept})/A$.

For full characterization of a deep level, three parameters must be known - a concentration of centers, an energy in relation to the bands, an effective cross section and qualitative classification describing its behaviour, i.e. whether the deep center operates as a recombination center or as a trap and what type of carriers it attracts (holes or electrons). Temperature sweep of the cathodic field evolution $E_C(t)$, demonstrated in Fig. 6.5, allows to find E_t, σ.

In our experiment we measured 1 min evolution with 50 ms steps in temperature range 280-325 K. Bias 350 V was chosen low enough to avoid the necessary reconnection of E-field. Since the bands are bent upward for Au/Au metal contacts, the nature of the deep level is referred to an electron trap. Double exponential fit (6.14) matches better to evolution of $E_C(t)$ so two polarization process are taken into account.

The Arrhenius plot of the dependency (6.20) is shown in Fig. 6.7. We concluded the energies of deep traps as

$$\mathsf{E}_{t1} = (0.87 \pm 0.02)\,\text{eV}, \mathsf{E}_{t2} = (0.77 \pm 0.02)\,\text{eV}\,.$$

Trap energies are related to the zero-temperature band gap $\mathsf{E}_{G0} = 1.607\,\text{eV}$. taken from the conduction-band edge and estimated the effective cross-section as

$$\sigma = 1 - 10 \times 10^{-15}\,\text{cm}^2.$$

Traps capture mainly electrons since polarization takes place below the cathode where the positive space charge is formed. Exact determination of cross-sections is problematic because of the narrow temperature range. A small uncertainty in intercept is extremely magnified by taking exponential in evaluation of σ. The square-root of the cross-section represents roughly an active not a geometrical diameter of the trap around 0.1-1 nm because a probability of carrier capture must be accounted to the real dimensions. Typical point defect cross-sections range in an interval 10^{-15}-$10^{-22}\,\text{cm}^2$ covering eight orders of magnitude.

Slower component $\tau_1 > \tau_2$ in the polarization process corresponds to the higher activation energy $\mathsf{E}_{A1} > \mathsf{E}_{A2}$ and the lower position of the trap. So, it takes longer time the deeper level to de-occupy because electrons must overcome a higher barrier $|\mathsf{F} - \mathsf{E}_t|$. Increase of temperature leads to a quick polarization and a smaller time constant (see $\tau(T)$ in Fig. 6.7).

Figure 6.6: Temperature sweep of E-profiles under the three various bias voltages. Temperature growth leads to depolarization and recovery to the flat field (brown arrows). Sample BK39UA2, contacts Au/Au.
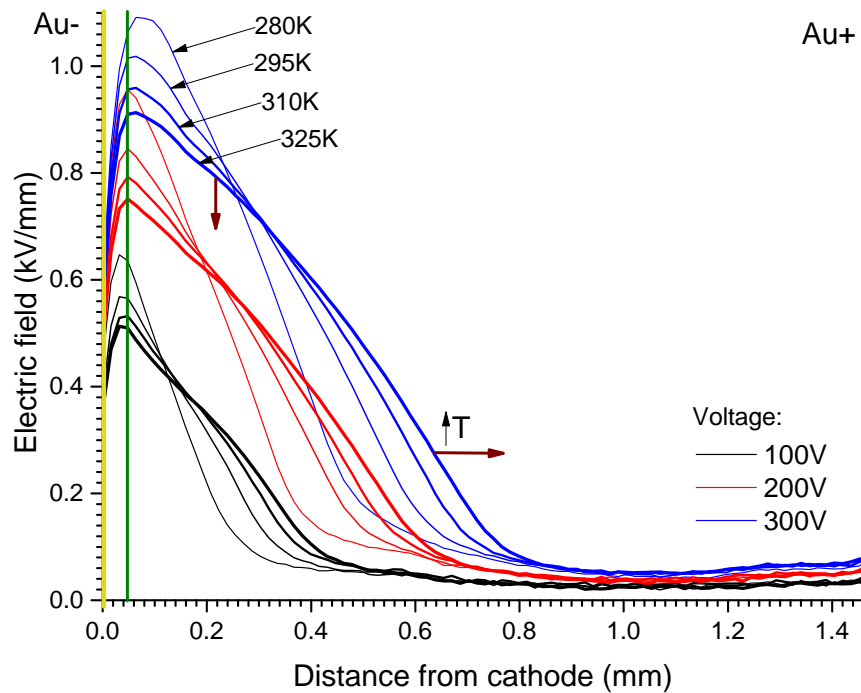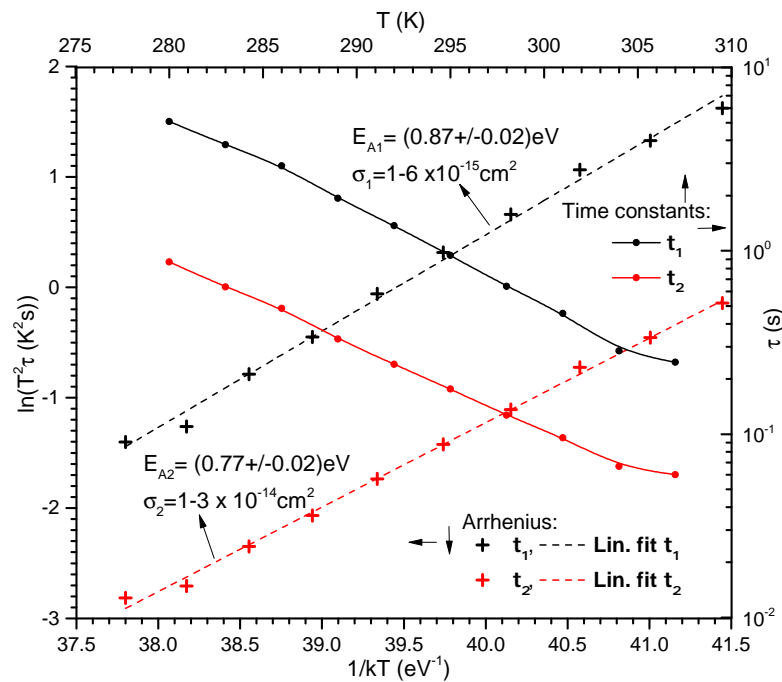

Figure 6.7: Arrhenius plot of the time constants versus temperature. Time constants come from exponential fit of the cathode field evolution. The energy of the level is determined as the slope of the line and the cross-section is obtained from its interception. Sample BK39UA2 with gold contacts under 350V.

6.4 Gold versus indium electrodes

Relation between the Fermi level and band bending

Deep centers located in the midgap are responsible for trapping or detrapping of charge carriers. A change in population at the deep level leads to formation of a charged layer and screening of the external E-field. The carriers, released from the deep level during the process of polarization, are forced to the attracting electrodes, until they reach the dead layer. Therefore the region of the charged layer is depleted from carriers. The intrinsic Fermi level, extended throughout a high-resistive detector, lies in the proximity of the midgap and strongly influences occupation of the deep level. In the bulk of a semiconductor the concentration of electrons n_t, filling the traps, is governed by the Fermi-Dirac distribution function

$$n_t = N_t f_t(\mathsf{F}_i) = N_t \left[1 + \exp\left(-\frac{\mathsf{E}_t - \mathsf{F}_i}{k_B T} \right) \right]^{-1}. \tag{6.21}$$

The heavy dependence of the exponential function upon the mutual position of the deep level and the FL is evident. In the thermal equilibrium, the filling fraction n_t/N_t is spontaneously set in the way that the deep level is occupied neutrally in the global view.

The band bending at a metal-semiconductor interface is ruled by the model based upon M-S work functions difference. The difference in work functions of the metal and semiconductor creates a potential barrier for carriers at the M-S interface. In the thermally equilibrated system, the Fermi levels of the metal and semiconductor coincide. In the steady-state regime under the bias, the quasi-Fermi level (QLF) linearly ascends through the volume of the semiconductor starting at the anode. At the interface the FL is deformed as a result of transition between materials with different concentrations of free carriers. The question is, whether the QLF is still a valid and well-defined physical quantity. According to the S-M transport theory of Sze and Crowell [32], the QLF is no longer continuous.

For transparent and intuitive interpretation of our experiment we will bear in mind the simple theory of the M-S contact by Schottky. The presence of band bending at the interface modulates the line of the Fermi level. If the work function (WF) of the semiconductor Φ_S is lower than the metallic one Φ_M, the semiconductor bands are tilt upward for n-type. Oppositely, if $\Phi_S > \Phi_M$ then the bands are curved down. Thus, the choice of the contact metal has a profound impact on the direction of band bending and consequently on the shape of the E-field.

To demonstrate this idea, two metals with the diverse work functions were selected[1] - gold and indium with the relation to CdTe [34]:

---

[1]Another favorite and convenient couple is platinum Φ_{Pt} = 5.1-5.9 eV and aluminium Φ_{Al} = 4.1-4.3 eV.

$$\Phi_{Au} = 5.1 - 5.4 \, \text{eV} > \Phi_{CdTe} = 5.1 - 5.3 \, \text{eV} > \Phi_{In} = 4.1 \, \text{eV} \,.$$

The work function of CdTe is dependent upon its resistivity. N-type low resistive samples have a lower work function $\Phi = 5.1 \, \text{eV}$ in contrast to the behaviour of semi-insulating CdTe $\Phi = 5.3 \, \text{eV}$ [33], [22].[2] In general, the accurate measurement and estimation of a work function (WF) is a non-trivial issue dependent upon the employed method and conditions. For example, a thin layer and a bulk crystal have different values. The crystal orientation changes the work function in the range of 0.1 eV. An ideal measurement should be carried out at the zero temperature when the Fermi-Dirac function is step-like. We will be satisfied with the fact that the difference between the work functions of gold and CdTe is roughly estimated to 0.15-0.2 eV.

Real current-voltage curves

A metal-semiconductor potential barrier affects the injection and collection of carriers. The transfer of an electron from the Fermi level in the metal to the conduction band of the semiconductor is associated with the passage through the potential barrier Φ_{Bc}. This barrier is enlarged as the upward incurvation of the conduction band grows. Oppositely for holes, the metal contact is blocking for the valence band curved down and injecting for the upward curvature. Therefore, an indium electrode is injecting for electrons and blocking for holes whereas a gold electrode facilitates the entrance of holes and blocks electrons.

In our experiment, all combinations of electrodes were deposited by PVD and studied on the identical n-type sample B39UA2. Firstly, a gold-gold combination of electrodes was prepared, followed by gold-indium and finishing with an indium-indium pair. We started with mechanically polished sides of CdTe. Each metal contact ready for removing was etched in 1% bromine solution of ethylene glycol for 1-2 min until a clear CdTe surface was received. Remaining sides of the block were masked to avoid their disturbance.

In an n-type semiconductor, the majority carriers are electrons with concentration dominantly exceeding the number of holes. Moreover, the significant difference between the mobility of electrons and holes $\mu_e > \mu_h$ empowers the electron current in the expense of the hole current. Thus, the only electron contribution to the overall charge transport will be assumed.

The height of the potential barrier varies with the bias and an each abrupt M-S interface represents a single Schottky diode with the current-voltage (IV) dependency

$$I(U) = I_S \left[\exp\left(\frac{qU}{k_B T}\right) - 1 \right] \tag{6.22}$$

---

[2]Oppositely, p-type samples have a higher work function in comparison to intrinsic CdTe.
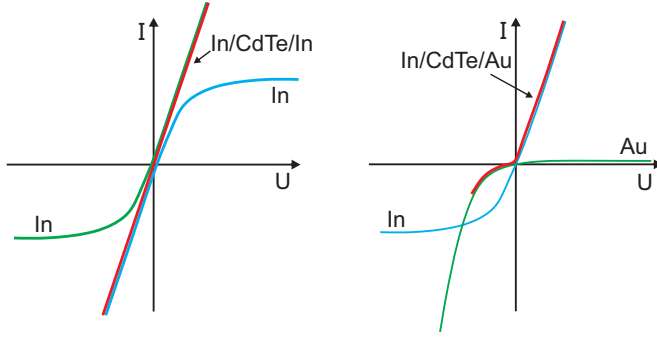
Figure 6.8: Construction of the IV curves from the superposition of two individual Schottky diodes representing carrier injection at the metal-semiconductor contacts. Homo-typed detector structure exhibits an ohmic behavior while the hetero-types contacts are rectifying.

where I_S is a saturation value for $U \to -\infty$ dependent upon a mechanism of the transport. For the classical thermally-emissive theory the factor I_S is given by

$$I_S = A_R S T^2 \exp\left(-\frac{q\Phi_{Bc}}{k_B T}\right) \tag{6.23}$$

where $A_R = q k_B^2 m_e^* / 2\pi^2 \hbar^3$ is called the Richardson constant[3], S is the area of the contact, the barrier Φ_{Bc} is equal to $|\Phi_M - \chi_S|$.

In the case of the symmetric structures (Au-Au, In-In), the M-S contact injecting electrons is arranged in the forward direction for both polarity of the power supply (Fig. 6.8). The net current is governed by two identical diode equations (6.22) written as

$$
\begin{aligned}
I_{M_1 S M_1}(u) &= I_{S1}[\exp(u) - 1]\chi_{(0,\infty)}(u) - I_{S1}[\exp(-u) - 1]\chi_{(-\infty,0)}(u) \\
&= I_{S1}[\exp(|u|) - 1]\mathrm{sign(u)}\,.
\end{aligned} \tag{6.24}
$$

Here, reduced voltage $u = qU/k_B T$ was introduced as a unitless variable. The function $\chi_{(a,b)}$ is a characteristic function of the interval (a,b), i.e.

$$\chi_{(a,b)}(u) = \begin{cases} 1 & \text{for} \quad u \in (a,b) \\ 0 & \text{for} \quad u \notin (a,b)\,. \end{cases} \tag{6.25}$$

The function sign(u) is defined as

$$\mathrm{sign}(u) = \begin{cases} -1 & \text{for} \quad u \in (-\infty, 0) \\ 0 & \text{for} \quad u = 0 \\ 1 & \text{for} \quad u \in (0, \infty)\,. \end{cases} \tag{6.26}$$

Expanding expression (6.24) to the Taylor series in restricted a interval of low voltage, one obtains from the linear term the current that is directly proportional to the applied bias u, i.e. the Ohm law

$$I(u) = I_{S1} u\,. \tag{6.27}$$

---

[3]Compare with prefactor A defined in 6.18.

Figure 6.9: Comparison of the steady-state E-profiles for electrode pairs Au/Au, Au/In and In/In. Gold as a cathode leads to the significant polarization, while indium makes the field flat with slight bending downward at the cathode zone. The synergy of hetero-type pair gold-indium does not result in a dramatic change of the behavior from the native combinations Au/Au resp. In/In. The bottom left plot depicts IV curves of the detector for diverse contacts. Mono-type electrodes have ohmic curves. Indium as cathode is injecting whereas the cathodic gold rectifies for the heterogenous combination. Sample BK39UA2.
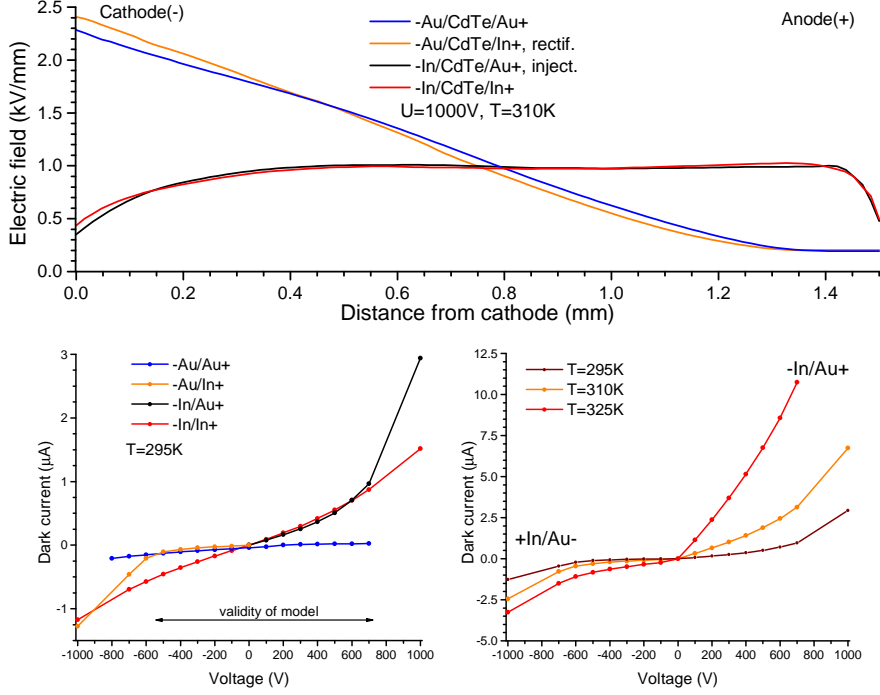

Considering the distinct character of injection for gold and indium contacts in the hetero-structure Au/CdTe/In, we conclude to the asymmetric dependency

$$I_{M_1SM_2}(u) = I_{S1}[\exp(u) - 1]\chi_{(0,\infty)}(u) - I_{S2}[\exp(-u) - 1]\chi_{(-\infty,0)}(u).\qquad(6.28)$$

Rectification is magnified when metals with qualitatively different behaviours are chosen for a CdTe detector. From the stated reasons, we will classify the mono-type electrodes as ohmic for low bias and the heterogenous combination as rectifying as is documented on experimental results in Fig. 6.9. For the bias lower than -500 V, the current drops from 0.1 μA at -500 V to 1.3 μA at -1000 V for the rectifying direction of the Au/CdTe/In structure. Another theoretical model describing IV curves is outlined in the appendix C taking into account injecting as well as a collecting M-S contact.

Measurements of IV curves are affected by the shunt current flowing across the sides and edges of the cuboidal detector due to unoccupied surface states. Passivation of sides or an implementation of the guard ring should lead to the elimination of surface currents. The response of the IV curve to the sweep of the temperature for the In-Au couple reveals a typical dependency given by (6.22).

Figure 6.10: Polarization observed on the structure In/CdTe/In. The field of the negatively charged layer adds to the external field made by bias. Bands tilt down make the occupation of the deep level more probable. The centers are filled with electrons mainly injected from the cathode.
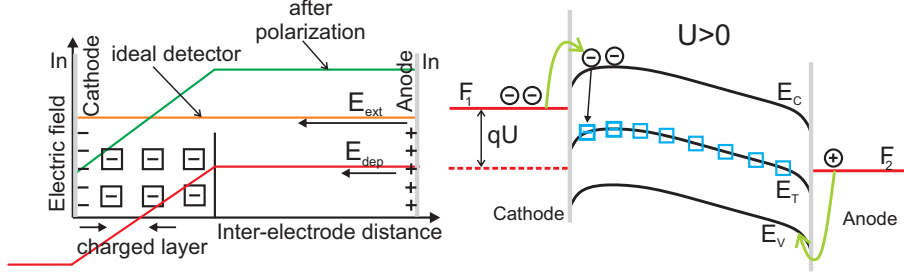

Electric field profiles

An abstraction of the In/In polarization mechanism is depicted in the Fig. 6.10. The combination of three main factors helps to form the negatively charged layer (analogical to the positive layer from the Fig. 6.1 for the Au/Au case). An indium contact bends the bands down. Consequently, the quasi Fermi level under the bias is elevated in relation to the deep centers. The initial neutrality is violated. On the top of that, electrons are massively injected from the indium cathode. Their excess is captured by deep centers similarly as is expressed in the formula (6.21). The trapped charge in the depletion zone reinforces the external E-field in the dead layer. At the vicinity of the cathode, the field from the charged layer subtracts from the external E-field leading to the visible drop (Fig. 6.11). Since we have visualized the shape of the polarized E-field for the Au/Au structure as a right-angled triangle neighbouring the cathode, at this time we are faced to the complement geometric shape - a rectangle minus the triangle. In spite of the simplicity of the idea, it does not loose anything from its functionality and universality. To give an example we are able to predict a voltage dependence of the In-In structure. As the bias is raised, the area of the rectangular grows collectively with the triangular removal. This claim is in concordance with the experimental data.

The size of the effect does not proportionally correspond to the value of work function difference $\Phi_{CdTe} - \Phi_{In}$ in comparison to the value $\Phi_{Au} - \Phi_{CdTe}$. The origin of the discrepancy is unknown.[4]

We will turn our attention to the hetero-type contact structure Au/CdTe/In. First-ly, let us comment the expected trend of the E-field profiles when a gold electrode represents the cathode. The bands below the gold contact are tilted upwards mean-while the indium contact curves the bands down. The quasi Fermi level crosses up the level of traps at the cathode whereas at the anode mutual displacement is amplified, particularly when the polarized field is developed across the entire detector thickness.

---

[4]One explanation asserts that the values of WF are only theoretical (probably exaggerated) and does not comply to the experimental conditions.

Figure 6.11: Temperature and voltage dependency for gold and indium based electrodes. When gold acts as a cathode, the E-field depolarizes at elevated temperatures. Meanwhile for the cathodic indium the downward bending is amplified. Sample BK39UA2. Au-/* plots are reconnected.
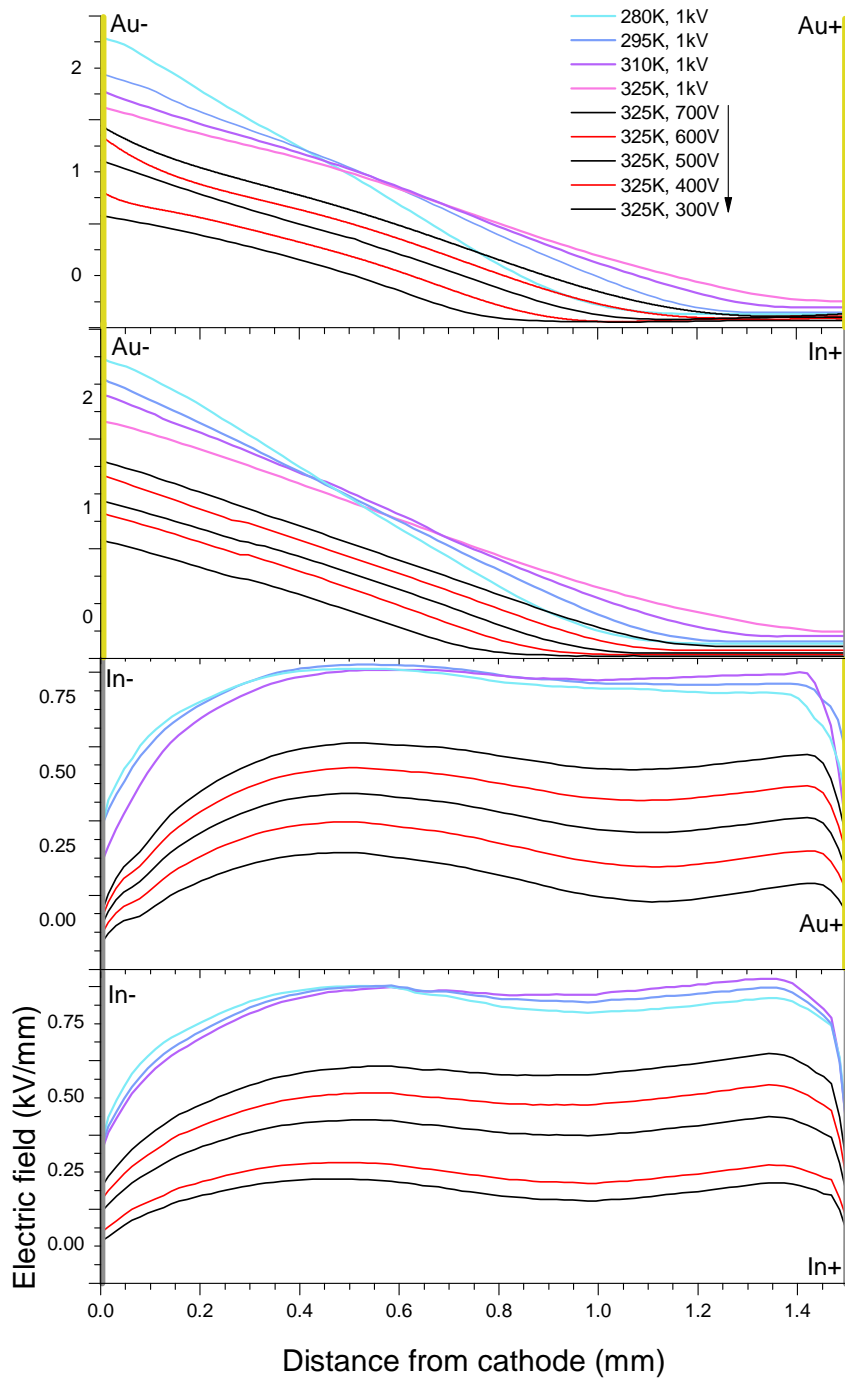
The polarization gets stronger. The stated phenomenon is poor but recognizable (Fig. 6.9).

Secondly, let us discuss the case when the indium contact becomes the cathode. The mutual shift between the FL and the deep level causes depopulation centers below the anode and thus an additional triangle above the flat end should emerge. The prediction was not experimentally confirmed for the n-type sample, since the difference is indistinguishable from the In/In arrangement in the interval of measurement uncertainty. This correlates with the fact that the polarization evinces only by the cathode space. The band curvature at the cathode and anode is not accurately symmetrical for the contacts of identical metals. The displacement between the steep FL line and the parabolic DL band is constructed additively at the cathode and subtractively at the anode resulting in the diverse shape of band bending.

The temperature dependency of the E-field profiles for the couple Au/Au is already well-known and justified from the section 6.3. Bearing in mind the message of the last paragraphs, the same thermal behaviour is deduced for the -Au/In+ arrangement. However, the situation is definitely contrasting for the structures In/In and -In/Au+. Here, the E-profiles are even more polarized as a consequence of the FL elevation from the DL line with a temperature increment.

6.5   Detector under sub/above bandgap illumination

Additional illumination of a CdTe detector could be exploited as a tool for studying internal processes and for simulating various physical conditions. As we will see further the illumination radically influences E-field profile and its integration to the Pockels experimental set-up makes the whole system very versatile and interesting.

Utilization of the illumination

In general, there are three main practical applications for additional illumination. We can employ gap-laser for the E-field depolarization and for the recovery of the detector to its standard operation. IR illumination can serve for inspection of a deep level because its filling factor changes as the photon energy of the IR excitation is tuned.

Moreover, the supplementary illumination might even simulate X-ray radiation in a limited way. To develop this idea we will introduce mass attenuation coefficient (MAC) for X-ray radiation μ/ϱ defined as the length attenuation coefficient μ reduced by the material density ϱ. It describes beam attenuation by the formula

$$I(z) = I_0 \exp\left[-\frac{\mu}{\varrho}(\varrho z)\right] \tag{6.29}$$

where $I(z)$ is the intensity of the beam in the depth z and I_0 denotes the initial flux of the radiation. Attenuation coefficient is dependent upon the photon energy and tabulated for CdTe [36]. Let us suppose an X-ray source with photon energy 100 keV, CdTe photoelectric MAC about 1.65 cm^2/g, the detector thickness 1.5 mm and mass density 6.2 g/cm^3. Using formula (6.29) we conclude that 15% of all photons are absorbed within 1/10 of the detector depth, 55% in 1/2 and 80% in the full width. Generation of a single electron-hole (e-h) pair consumes averagely 4.4 eV, thus one 100 keV photon creates approximately 23×10^3 pairs.

Illumination with above-gap energy 1.5-1.8 eV has an ability to produce electron-hole pairs. However, the process takes place in a very thin surface layer due to strong absorption coefficient. Whereas subgap IR excitation in 0.6-1.5 eV transmits the material but cannot directly make e-h pairs. The only possible transfer of an electron from the valence to the conduction band must be mediated across an energy level between them. Therefore, none of the mentioned could fully substitute a genuine X-ray source. In the ref. [22] the comparison of gap-laser illumination with X-ray tube is documented having similar effects.

Enhanced Pockels set-up

The implementation of the supplementary illumination of the CdTe detector to the Pockels arrangement is depicted in Fig. 6.12. For excitation of charge carriers the laser illuminates the thin semi-transparent gold contact. The fractional part of the incident
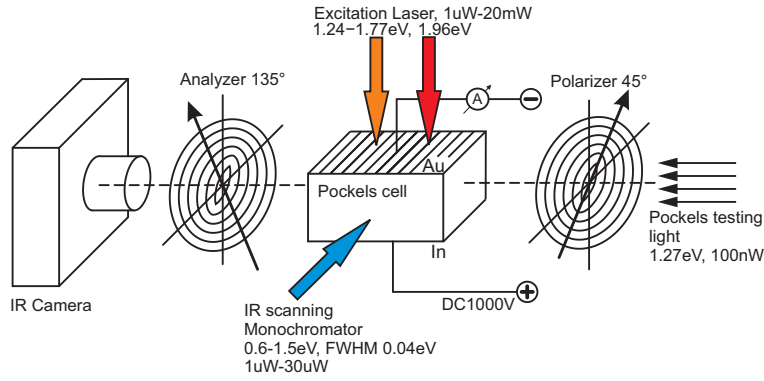
Figure 6.12:
Experimental arrangement for additional illumination of a CdTe detector. Excitation laser penetrates through the semi-transparent Au-electrode. The method of IR scanning uses a monochromator beam passing the detector laterally.

beam penetrates to the crystal. Reflectance of gold is approximately constant in the range of 0.5-1.7 eV. Absorption coefficient of gold is about $8.5 \times 10^5 \, \text{cm}^{-1}$ [25]. If the gold electrode should exhibit transparency more than 2%, it needs to be maximally 45 nm thin. Since our deposition chamber does not allow to adjust precisely the layer thickness, we estimate it to several tens of nanometers.

Laser Cube, Coherent Inc. (red diode 1.94 eV(638 nm), 30 mW) and the tunable laser were used for excitation. For measurement of the light intensity, Vega (Nova) Ophir power meter was applied.

Another auxiliary IR illumination for scanning deep level comes at the right angle from the lateral side. To obtain a tunable IR source and get a particular photon energy, the appropriate wavelength was selected by a monochromator (Karl-Zeiss SPM2, single LiF prism) from the black body radiation (50 W halogen lightbulb). Constant photon flux of the IR source was received by adjusting the slit at the output of the monochromator. Rough specification of the IR source are - spectral range 0.6-1.5 eV, FWHM 0.04 eV (50 nm), power 1-30 µW. The tunable laser could be also employed as an IR source for the limited spectral range 1.24-1.5 eV.

In our further experiments we restrict to the illumination of the gold electrode in Au/CdTe/Au and Au/CdTe/In structures.

Polarization under the illumination

We begin the analysis of internal processes in the illuminated detector with the subgap excitation. A conceptional insight to the problem brings an improvement of the band energy scheme (Fig. 6.13) introducing the Au/In electrode arrangement. We already know that gold curves the bands upward and indium downward. When the gold contact acts as a cathode, a positively charged layer is accumulated and E-field is polarized. The entire bulk is transparent for the subgap light, hence the laser beam passes throughout the crystal. We suppose the laser excitation energy E_E to be $\mathsf{E}_E < \mathsf{E}_G$ but $\mathsf{E}_E > |\mathsf{E}_c - \mathsf{E}_t|$ and $\mathsf{E}_E > |\mathsf{E}_t - \mathsf{E}_v|$. The weak but still non-zero absorption leads to the electron excitation from the deep level to the conduction band as well as to the excitation from the valence band to the deep level. On the other hand, electrons are being trapped

Figure 6.13: Scheme of processes in a Au/CdTe/In detector after cathode illumination. The progress of charge polarization fundamentally depends upon the energy of excitation laser. Subgap light penetrates through the entire sample and excites electrons from the deep level to the conduction band. Deep centers, that cause formation of positive charge, are depopulated and polarization is boosted. Whilst the gap light generates electron-hole pairs close the surface. Holes are collected by the cathode while electrons are captured by traps. E-field is recovered to the flat course.
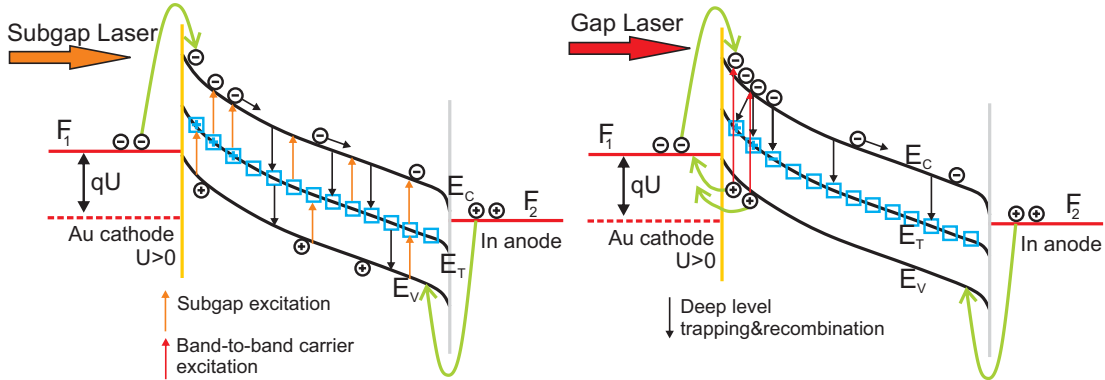
on their way to the anode. All processes are moreless balanced taking place along the whole specimen. Laser induced ionization of deep centres is permanent close the cathode where the quasi Fermi level lies under the deep level line. From the overall view, the charged layer is enlarged and the polarization is reinforced.[5]

However, a beam of the gap laser is stopped at the uppermost surface layer where electron-hole pairs are massively generated. Holes neighbouring the cathode are instantly collected and do not contribute to the polarization process. Whereas electrons drift to the attracting anode. Initially ionized deep centers capture passing-by electrons and they start to fill. Depopulation of deep centers due to the band bending is overweighed by trapping of excessed electrons. The depletion layer is reduced. E-field is depolarized and recovers to the flat profile of an ideal detector. For the giant generation, i.e. high photon flux, the negative character of charge occupying deep centers prevails over the positive as trapping of electrons dominates. Similar explanation is given in [37].

Photon flux dependency

Higher flux of subgap photons amplifies depolarization. An ideal flux for studying the mechanism of electron emission should be comparable with the number of deep centers presented in the entire volume of the detector. Suppose the typical concentration of deep centers to be $10^{15}\,\mathrm{cm}^{-3}$ and the detector with dimensions $(5 \times 5) \times 1.65\,\mathrm{mm}$. The

---

[5]We cannot essentially distinguish whether the deep level communicates preferentially with the valence band or the conduction band. It other words, the effect on the final charge of the deep level is the same when the hole is emitted from DL to the valence band or whether the electron is trapped by the DL from the conduction band. And vice versa, if the hole is captured from the valence band to DL or if the electron is released from DL to the conduction band. To keep the model and interpretation simple, we restricts to excitation between the conductive band and DL.

total number of deep centers in the sample is 4×10^{13}. Then the appropriate flux covering them all each second is $1.6 \times 10^{14} \, \mathrm{cm^{-2}s^{-1}}$ with intensity $38 \, \mu\mathrm{W}$ at energy 1.5 eV. The intensity must be further divided by the transmittance factor of the gold contact ($\approx 50\times$). Under higher fluxes, the emission from the deep level might be overlapped by simultaneous processes and under a weak flux the effect does not theoretically exceed its saturation.

The real dependency of E-field profiles upon the intensity of light (or equivalently upon the photon flux) is shown in Fig. 6.14. High intensity of the subgap laser (1.31 eV) leads to the disapperance of the cathode field E_C because the signal underneath the electrode is badly resolved by the IR camera or lost. For the huge power of the gap laser (1.96 eV) the surface recombination is substantial and photocurrent gets risky high. Moreover, the depolarization saturates at 20 mW and an additional increment of the intensity does not results into the reversed polarization. Therefore, we concluded that convenient intervals of intensities are 5-100 μW for subgap and 0.05-20 mW for gap illumination.

In the paper [38], the electric field in the dependency upon the photon flux under X-ray irradiation was studied. A similar result was observed as we received for the subgap illumination.

Figure 6.14: Recovery and polarization of the electric field in the Au/CdTe/In detector induced by the illumination of the cathode. When the sub-bandgap light penetrates the detector, electrons from deep centers are excited to the conduction band. Empowered depopulation of centers leads to the more concentrated charge layer and larger polarization. Situation for the gap light illumination is distinguished. At the surface below the gold electrode, electrons and holes are photo-generated. The cathode immediately collects holes, meanwhile electrons transfer to the bulk. On their path to the draining anode, some of them are trapped by deep centers resulting in the restoration of the detector to the flat E-field profiles. Sample BK39UA2, E-profiles are reconnected.
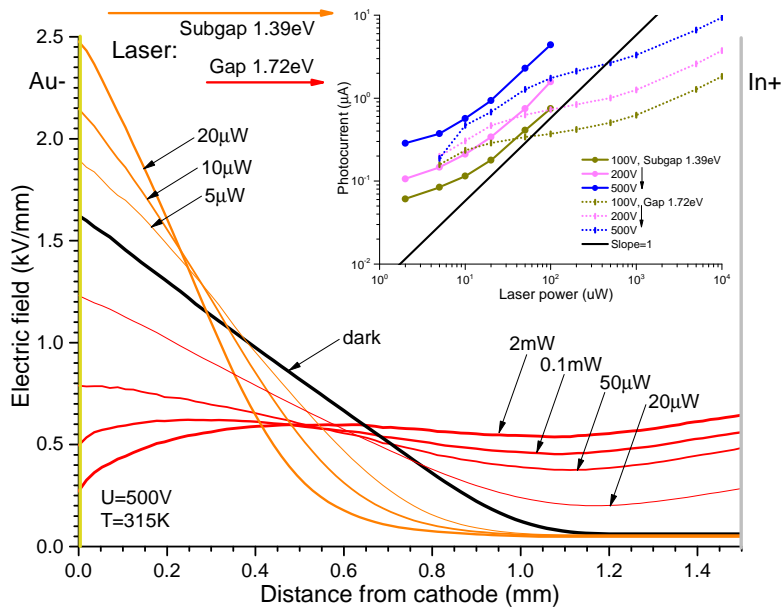
Spectral dependency close the absorption edge

Let us shortly discuss the behaviour of E-field profiles in dependence upon the photon energy of excitation in the region close to the absorption edge. The spectral sweep is purely performed by the tunable laser illuminating the gold contact. We have detaily surveyed the effect of the gap and subgap illumination and we concluded the diametral distinction between both cases.

Now we understand them as limiting cases and we focus on the transition between them in range 1.3-1.7 eV. The experimentally obtained E-profiles for various excitation energies are plotted in Fig. 6.15. From the inset one immediately sees that the cathode field E_C is not a monotonous function of the photon energy. In fact, the field E_C represents cross-sections of E-profiles in the spectral sweep. Here, the cathode field in the darkness was chosen as a reference to compare the change with. For the subgap excitation energy the E-field is polarized and the curve lies above the dark background. Since the gap illumination depolarizes E-filed, the curve is situated below the background value. Subgap peak with the center at 1.435 eV may be correlated with photogeneration of electron-hole pairs between acceptor level V_{Cd}^{2-}-In$^+$ and the conduction band. At 1.47 eV the polarization and the surface photogeneration are compensated and the E_C is balanced to its dark value. Surface photogeneration affects E-field in the constant manner for $E_E > 1.51eV$.

Figure 6.15: Spectral development of the polarization for various photon energies of the excitation laser. The laser power is fixed to 50 μW. The inset reveals spectral dependency of the electric field under the cathode. Polarization reaches the maximum for subgap energy 1.435 eV. The drop of the electric field for the above-gap photon energies is merely constant. Sample Au/B39UA2/Au.
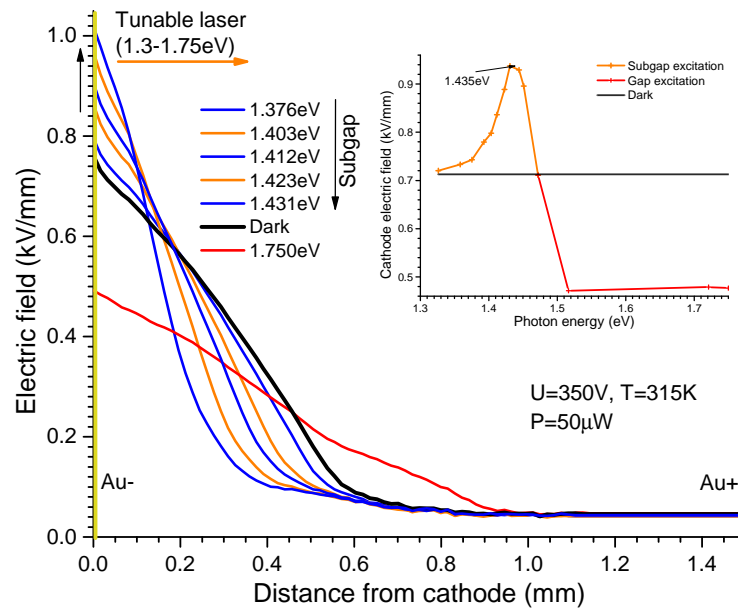
Illumination of Au/Au vs. Au/In structure

Our further attention was aimed to the comparison of gold-gold and gold-indium contact structure. In both cases the only gold cathode was illuminated. As the reference, the intensity of 20 μW was chosen for the subgap and 1 mW for the gap laser. The difference is notable from the plot in Fig. 6.16 and not very surprising. All curves - in the darkness, after illumination by the gap (subgap) laser are less sloped for the homo-type Au/Au arrangement where the band bending is symmetrical.

The bottom graph shows what happens when the polarity of Au/In detector is switched. Here, the indium electrode represents the cathode. From the analysis taken in the section 6.4, we recognise the flat E-profile measured in the darkness. Injection of electrons is strong for the -In/Au+ configuration. After the subgap illumination the negative charge in the vicinity of the indium electrode is dissolved. Electrons, released from deep centers, carry on in the transfer towards the gold contact. During their journey they might be captured by deep traps. Therefore, the electric field is mildly decreased beyond the vicinity of the cathode. Complementary, the field towards the cathode is refreshed to the flat line.

Figure 6.16: Comparison of Au/Au versus -Au/In+ structures under the gap and subgap illumination. The polarization property is stronger for the gold-indium couple. The bottom graph demonstrates depolarization after the subgap illumination when the polarity of power supply is swapped and the direction of illumination is maintained. Electrons are detrapped from the neighbourhood of the indium cathode and driven to the opposite electrode. Sample BK39UA2.
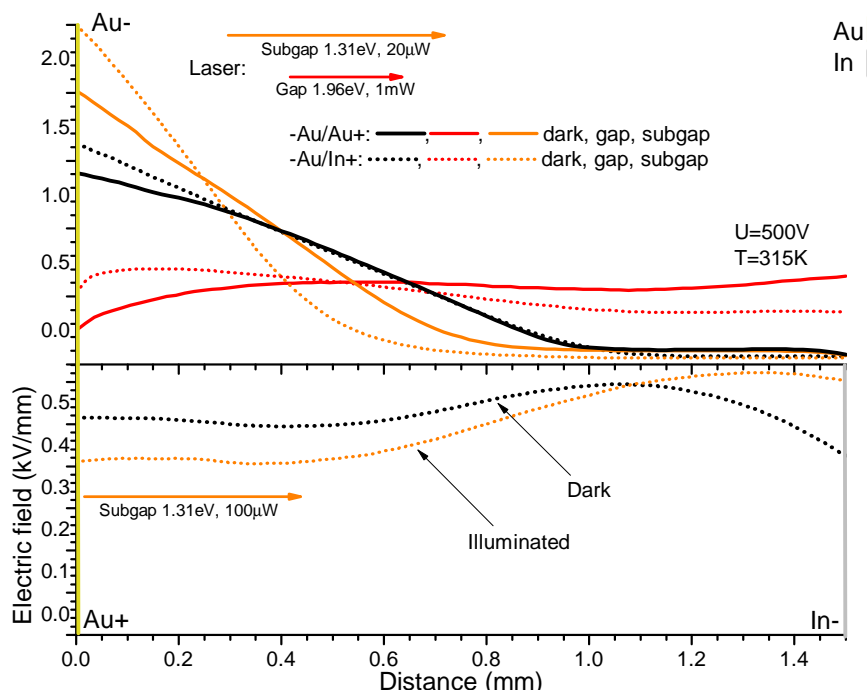
Method of the infra-red scanning

In the following text, we will outline the technique of IR spectral scanning and its application for deep level analysis. The enhanced experimental arrangement was already introduced in the Fig. 6.12. The set-up involves two light sources - the excitation laser and the IR scanning light. Since we know that the gap resp. subgap illumination dramatically changes the polarization state, the excitation laser is used for the preparation of an initial E-field profile. The purpose of the additional IR source is to test the response of the E-profile to a particular photon energy. When the photon energy coincides with the energy of the electron emission between two energy levels, then the change in E-field distribution is observed. As the IR light is being tuned in the interval $(0, \mathsf{E}_G)$, the response from the energy levels located in the bandgap is detected.

In general, the E-field dependency upon the photon energy of excitation has two regions of interest. Firstly, it is the range of 0.5-1.2 eV where transitions between the deep level and the conduction band (valence band) are anticipated. The second accent is aimed to the window of 1.3-1.5 eV below the absorption edge of CdTe discussed earlier.

The explanation the mechanism of electron detrapping induced by IR scanning light will be provided by an advanced energy band diagram (Fig. 6.17). For the subgap excitation when the positive charge is accumulated below the cathode, the additional IR illumination matching the energy $\mathsf{E}_c - \mathsf{E}_t$ ionizes deep centers. Detrapped electrons are collected by the anode and E-field polarization is supported.   Under the condition of the gap illumination, the E-field slope is lower (Fig. 6.18) and deep centers are more occupied than in the darkness. The probe of IR photons depopulates the deep level from electrons. Although excessed electrons at the cathode space are being captured by traps, they are subsequently emitted back to the conduction band. The trend of

Figure 6.17: Additional IR stimulation of deep level detrapping. Exact photon energy $\mathsf{E}_c - \mathsf{E}_t$ excites electron only from the deep level. Synergy of the IR scanning light and the simultaneous subgap-laser excitation reinforces polarization. For the case of the gap excitation, the IR scan counteracts with the flat-field restoration resulting in the crash of depolarization.
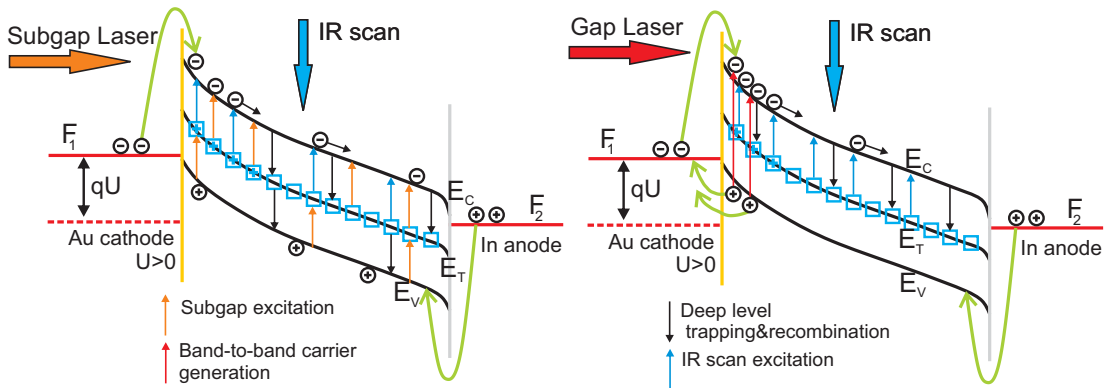
Figure 6.18: The method of the IR scanning employed for a diagnosis of deep levels. Excitation laser (gap, subgap) illuminates the detector through the semi-transparent gold contact (solid lines). The IR scanning light penetrates into the crystal from lateral sides. Specifically, the additive IR light excites electrons to the conduction band and depopulates the deep level. Its effect is added to the result of the illumination by the excitation laser (dashed lines). When the monochromator tunes the exact energy $E_c - E_t$ then DL detrapping is the most efficient and E-field polarization is maximized. The phenomenon is represented as a dependency of the cathode field E_C upon the scanning energy of IR light. Sample BK39B5, all profiles reconnected.
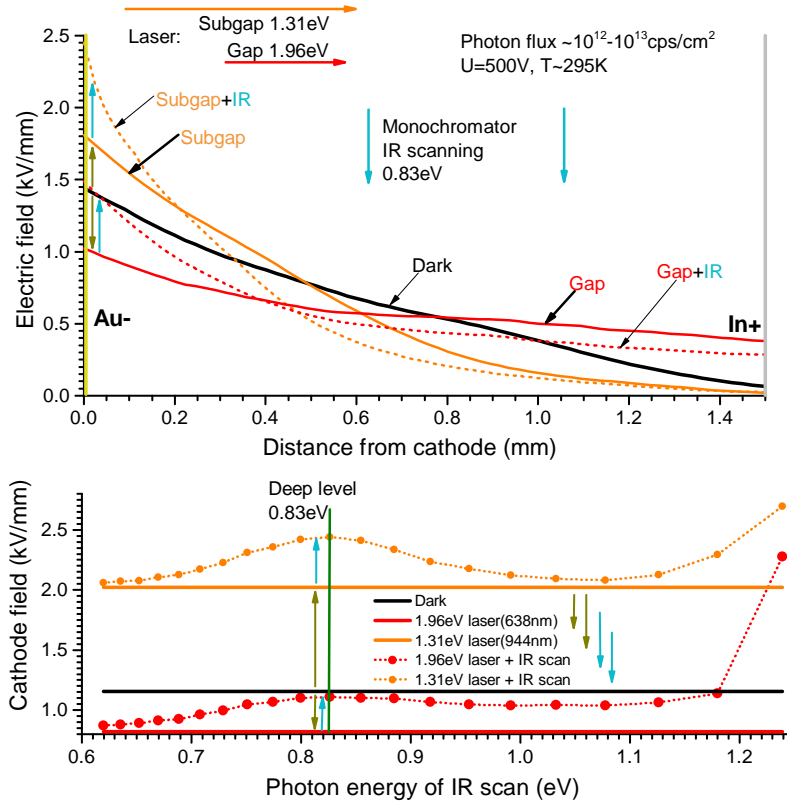
E-field is reversed to the polarized shape. Compensation of competing effects depends upon the mutual ratio of subgap and IR scan photon fluxes.

Since the spectral dependence of E-profiles is not monotonous, it is convenient to display their cross-section as a function of the IR photon energy as it was done in Fig. 6.15. Here, we have three reference lines - dark, gap 1.96 eV and subgap 1.31 eV excitations. The cathode field curve for 1.31 eV excitation lies entirely above the subgap reference whereas the E_C curve for 1.96 eV is restricted from the bottom by the gap reference and from the top by the dark background. The black-red boundary indicates almost the same photon flux of the IR scan and gap excitation laser. A mound at the energy ≈ 0.8eV is attributed to the detrapping from the deep level to the conduction band.

It was stated in the chapter 5 that small differences in E-field lies in the interval of an experimental uncertainty. But for the unchanged optical adjustment of the light path during the whole experiment, the E-field measurements are quite accurate.

7. Conclusion and closing remarks

The CdTe detector is a device for spectral and intensity measurement of X-ray and ionizing radiation. In its simplest arrangement the detector consists of a cadmium telluride crystal block and a pair of charge collecting electrodes. The detector performance is degraded due to the effect of charge polarization. The origin of the phenomenon is related to the presence of defect/impurity centers forming a level of free electronic states that is positioned in the midgap of the energy band diagram. The behavior of the deep level does not have strictly donor or acceptor-like character. Mutual position of the Fermi level and the deep level governs the filling of centers. Electrons and holes trapped in deep centers create a charged layer that screens the external electric field and corrupts charge carrier collection efficiency. Charged centers are concentrated at the metal-semiconductor interface, the rest of the volume is depleted from carriers. Due to the semi-insulting property the interfacial band bending extends deeply into the crystal and makes it semi-bulk. We have observed that gold tilts bands upward whereas indium downwards that is in concordance with the standard work function model.

Since CdTe evinces strong electro-optic effect, the detector represents a Pockels cell. Bias voltage producing the electric field has in fact two functions. It activates the modulation of the crystal transmittance and it supplies the detector that consequently causes the polarization. The transmittance was recorded by the infra-red camera. Its snapshots were processed with the result of a one-dimensional profile of the electric field between the electrodes. The electric field of an ideal detector is a flat line. When the detector is influenced by polarization, the profile becomes sloped. The linear model approximating real electric profiles was introduced. Derivative of the electric field gives information about the space charge density distribution.

The thesis was aimed to inspection of the deep level. For this purpose, three independent methods were exploited. Luminescence spectroscopy revealed wide band of optically active centers with peaks at 0.8 eV, 1 eV, 1.2 eV. Relation to the valence or conduction band edge was not found. It was discovered by comparison of etched and polished surfaces that 0.8 eV level is correlated with surface tension.

We have studied the time evolution of polarization at the early nonequilibrium state by the Pockels method. From the time-temperature development of the electric field under the cathode we deduced energies of deep levels 0.87 eV and 0.77 eV.[1]

Employing infrared scanning set-up we surveyed spectral dependence of the electric field polarization. The feature attributed to the transitions between the deep level and

---

[1]Taken from the conduction band edge.

the conduction band was identified at 0.8 eV. All measured values are in relatively good agreement.

Furthermore, two distinguished effects after additional illumination of the detector were observed. Whilst the light with photon energy above the bandgap recovers the electric field to the flat shape, the sub-bandgap light contributes to the higher polarization. The first fact has a perspective application for the future generation of CdTe detectors. The concept would be based on periodically switched illumination of the detector by diodes with the above-gap energy. A real test of the implementation and a study of radiation spectra were performed by SATO in the ref. [39] (Fig. 7.1a).

Figure 7.1: Time evolution of ^{241}Am radiation spectrum measured by Pt/CdTe/In structure under the bias 100 V, T=283 K. Adopted from [39].

(a) Due to the polarization of the detector, the charge collection efficiency fades away (40-45 min) until it definitely declines (80-90 min). Within the period of 90-95 min the detector was illuminated with near-edge 1.46 eV IR light onto the platinum upside electrode. The operation of the detector is temporally restored. Additional biasing (95-185 min) leads in repetition of the polarization effect and degradation of the spectrum.

(b) The same experiment and signal acquisition. However, in time 5-6 min the detector was illuminated by subgap 1.38 eV light resulting in the instant diminishing of the Am peak.
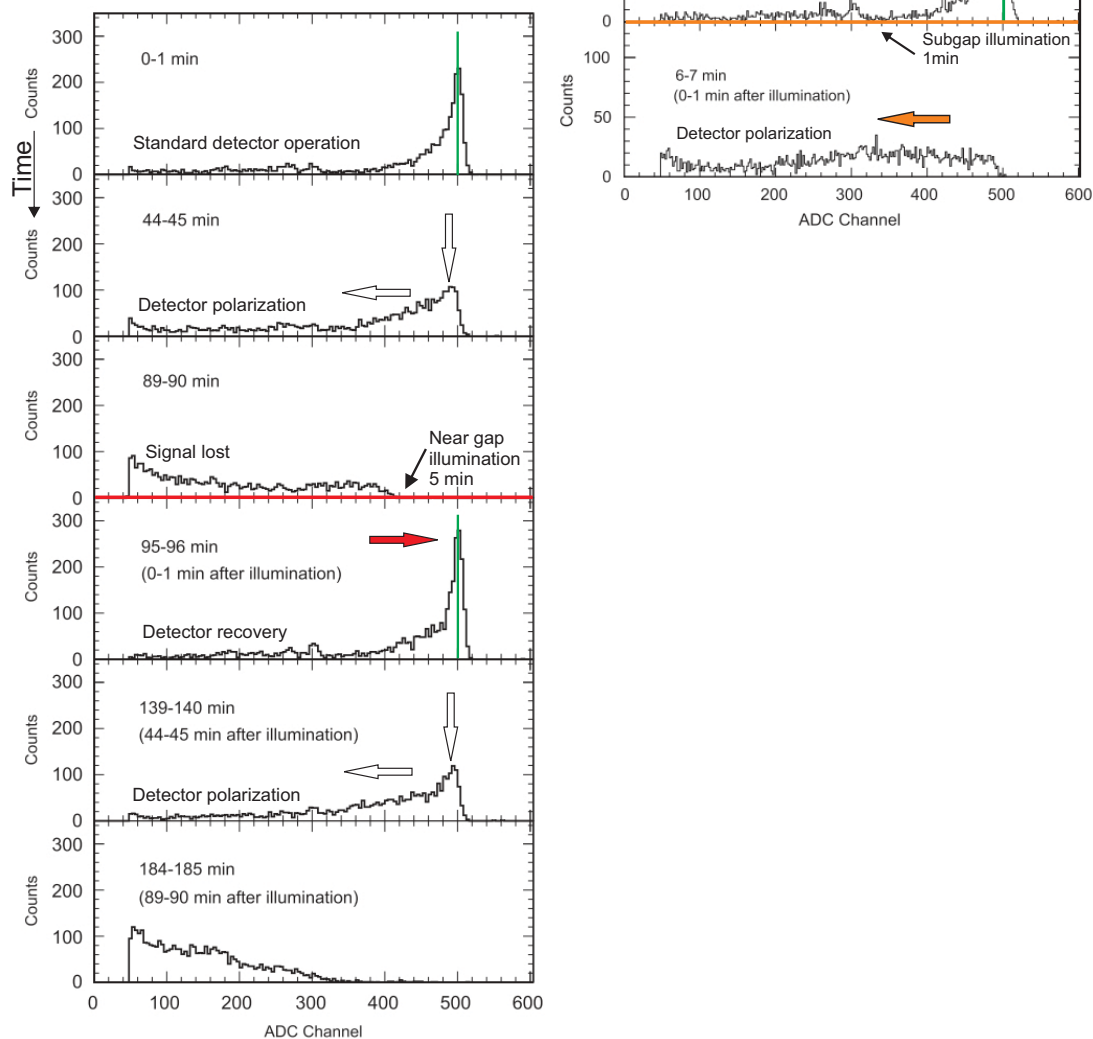
A. Derivation of non-vanishing and independent electro-optic Pockels coefficients for zinc-blendes

In this appendix we will demonstrate how the number of independent non-vanishing Pockels coefficients could be reduced using symmetry operations of the crystal class.

According to the Neumann principle, symmetry of a tensor quantity is the same or higher towards the crystal symmetry. Since zinc-blende structure belongs to F$\bar{4}$3m spatial group, the structure remains unchanged under symmetry operations of the class $\bar{4}3m$. Those symmetry operations are identity E, three two-fold axes C_2, eight three-fold diagonal axes C_{3d}, six diagonal mirror planes σ_d and six four-fold inversion axes S_4.

Generating elements for the class $\bar{4}$3m are S_4 and C_{3d}. For each side of cube, one S_4 axis exists. We will denote them S_{4x}^+, S_{4x}^-, S_{4y}^+, S_{4y}^-, S_{4z}^+, S_{4z}^-. Axes with plus/minus superscript correspond to opposing sides and holds $(S_{4x}^+)^{-1} = (S_{4x}^-)$, etc. Thus, only three positive matrices are quoted

$$S_{4x} = \begin{pmatrix} \bar{1} & 0 & 0 \\ 0 & 0 & \bar{1} \\ 0 & 1 & 0 \end{pmatrix}, \ S_{4y} = \begin{pmatrix} 0 & 0 & \bar{1} \\ 0 & \bar{1} & 0 \\ 1 & 0 & 0 \end{pmatrix}, \ S_{4z} = \begin{pmatrix} 0 & \bar{1} & 0 \\ 1 & 0 & 0 \\ 0 & 0 & \bar{1} \end{pmatrix} \tag{A.1}$$

and negative matrices are inverse.

Since a cube has eight vertices, there are eight types of three-fold diagonal axis. We will symbolize them

$$(111), \ (\bar{1}\bar{1}\bar{1}), \ (\bar{1}11), \ (1\bar{1}\bar{1}), \ (1\bar{1}1), \ (\bar{1}1\bar{1}), \ (11\bar{1}), \ (\bar{1}\bar{1}1).$$

Axes of opposite vertices are conjugated, e.g. $(111) \sim (\bar{1}\bar{1}\bar{1})$. Matrices of conjugated axes are mutually inverse, $(C_{3d}^{111})^{-1} = C_{3d}^{\bar{1}\bar{1}\bar{1}}$. A half of eight matrices are expressed as

$$C_{3d}^{111} = \begin{pmatrix} 0 & 0 & 1 \\ 1 & 0 & 0 \\ 0 & 1 & 0 \end{pmatrix}, \ C_{3d}^{\bar{1}11} = \begin{pmatrix} 0 & 0 & \bar{1} \\ \bar{1} & 0 & 0 \\ 0 & 1 & 0 \end{pmatrix}, \ C_{3d}^{1\bar{1}1} = \begin{pmatrix} 0 & 0 & 1 \\ \bar{1} & 0 & 0 \\ 0 & \bar{1} & 0 \end{pmatrix}, \ C_{3d}^{11\bar{1}} = \begin{pmatrix} 0 & 0 & \bar{1} \\ 1 & 0 & 0 \\ 0 & \bar{1} & 0 \end{pmatrix}.$$
$$\tag{A.2}$$

For example, C_{3d}^{111} axis converts $x \to y$, $y \to z$, $z \to x$ (Fig. A.1). Transformation of Pockels tensor to a new reference frame via symmetry operation shows that some coefficient are zero or equal to others.

First of all, a three-rank tensor T_{lmn} transforms to T'_{ijk} in the primed-reference

Figure A.1: Unit cell of CdTe projected to basic directions. In direction [111] cadmium planes periodically alter with telluric planes forming two single sublattices. Their mutual displacement under exertion of the electric field creates the dipole moment responsible for the Pockels effect.

(100), S_4 (110), σ_d (111), C_{3d}
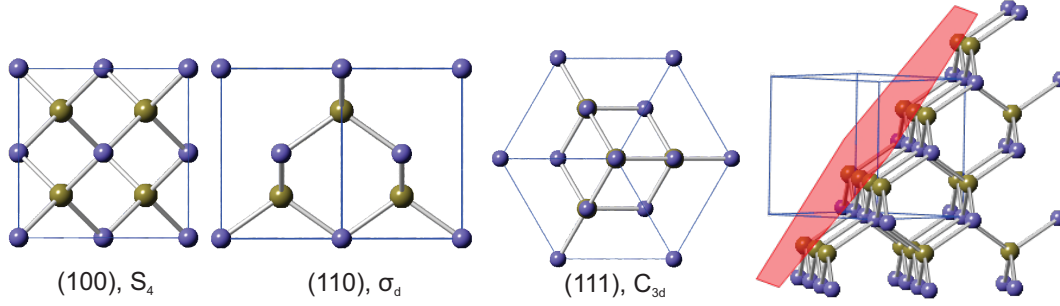
system according to formula

$$T'_{ijk} = \sum_{l,\,m,\,n} \kappa_{il}\kappa_{jm}\kappa_{kn}T_{lmn} \tag{A.3}$$

where $\kappa = (\boldsymbol{\kappa}_x, \boldsymbol{\kappa}_y, \boldsymbol{\kappa}_z)$ is the transformation matrix composed of direction cosines. As noted above, for Pockels tensor holds $R_{ijk} = R_{jik}$ due to the symmetry of the impermittivity tensor. For instance, the evaluation of the transformation for S_{4z}^{+} is stated below

$$
\begin{aligned}
R'_{111} &= \sum_{l,\,m,\,n} S_{1l}^{4z} S_{1m}^{4z} S_{1n}^{4z} R_{lmn} &&= \sum_{l,\,m} S_{1l}^{4z} S_{1m}^{4z}(S_{11}^{4z}R_{lm1} + S_{12}^{4z}R_{lm2} + S_{13}^{4z}R_{lm3}) \\
&= \sum_{l,\,m} S_{1l}^{4z} S_{1m}^{4z}(0 - R_{lm2} + 0) &&= \sum_{l} S_{1l}^{4z}(S_{11}^{4z}R_{l12} + S_{12}^{4z}R_{l22} + S_{13}^{4z}R_{l32}) \\
&= \sum_{l} S_{1l}^{4z}(0 + R_{l22} + 0) &&= (S_{11}^{4z}R_{122} + S_{12}^{4z}R_{l22} + S_{13}^{4z}R_{l22}) \\
&= -R_{222}.
\end{aligned}
\tag{A.4}
$$

After calculation of other R_{ijk} in the same spirit, we obtain that non-vanishing Pockels coefficients for S_4 class are

$$R_{113} = -R_{223},\ R_{132} = R_{231},\ R_{131} = -R_{232} \text{ and } R_{123}. \tag{A.5}$$

Three-fold diagonal axes make null R_{113} and R_{131} and set $R_{132} = R_{213}$, resp. $R_{213} = R_{123}$. All together

$$
\begin{array}{ccccccccc}
\cancel{R_{111}} & \cancel{R_{112}} & \cancel{R_{113}} & \cancel{R_{221}} & \cancel{R_{222}} & \cancel{R_{223}} & \cancel{R_{331}} & \cancel{R_{332}} & \cancel{R_{333}} \\
R_{231} & \cancel{R_{232}} & \cancel{R_{233}} & \cancel{R_{311}} & R_{312} & \cancel{R_{313}} & \cancel{R_{121}} & \cancel{R_{122}} & R_{123} \\
R_{321} & \cancel{R_{322}} & \cancel{R_{323}} & \cancel{R_{131}} & R_{132} & \cancel{R_{133}} & \cancel{R_{211}} & \cancel{R_{212}} & R_{213},
\end{array}
\tag{A.6}
$$

we see that only six coefficients survive having the same value. The second and the third row in (A.6) are twin due to the substitution ijk for jik. In the two-suffix notation

$r_{41} = r_{52} = r_{63}$. The Pockels matrix gains the simple appearance

$$
r = \begin{pmatrix}
0 & 0 & 0 \\
0 & 0 & 0 \\
0 & 0 & 0 \\
r_{41} & 0 & 0 \\
0 & r_{41} & 0 \\
0 & 0 & r_{41}
\end{pmatrix}.
\tag{A.7}
$$

In similar way, we discover that the impermittivity tensor is in the system of crystallographic axis entirely diagonal and isotropic

$$
\eta = \begin{pmatrix}
1/n_0^2 & 0 & 0 \\
0 & 1/n_0^2 & 0 \\
0 & 0 & 1/n_0^2
\end{pmatrix}
\tag{A.8}
$$

where n_0 is an isotropic refractive index. A second-rank tensor transforms its components in a simpler way

$$
T'_{ij} = \sum_{l,\,m} \kappa_{il} \kappa_{jm} T_{lm} \,,
\tag{A.9}
$$

that may be represented as matrix multiplication $T' = \kappa T \kappa^{\mathsf{T}}$. Exemplary, one finds restrictions to impermittivity tensor from $\eta' = S_{4x}\, \eta \, S_{4x}^{\mathsf{T}}$ or $\eta' = C_{3d,111}\, \eta \, C_{3d,111}^{\mathsf{T}}$ In reference systems that transform the one to the each other, the tensor property must be expressed in the identical form, therefore the initial and the primed impermittivites are equivalent $\eta = \eta'$.

B. Pockels biaxial refringence for non-oriented CdTe crystals

In the following text, we discuss a general case of transmittance of the Pockels cell taken from the experimental layout in Fig. 5.2. So far, it was assumed and detaily explained in chapter 4 that the electric field vector is oriented in direction (111).

In addition, we will take into account the situation when the external electric vector is arbitrarily deflected from the normal of the (111) crystal plane. This happens when a specimen is cut out from an ingot in a way when facets of the cuboid do not follow low index crystal planes (100), (110), (111), etc. Electrodes evaporated onto the opposite sides of specimen cannot exert E-field in the well-defined way. Formula (5.6) derived in chapter 5 becomes only approximative description of the real case.

Let us revisit the concept of the optical indicatrix constructed earlier in chapter 4. For the external electric vector pointing at right angle to crystal plane (111), the index sphere is reshaped to an ellipsoid with axis of revolution in coincidence with the electric vector. Secular matrix M_N from eq. (4.19) consists of a-diagonal and off-diagonal b-triangle. For a general vector $\boldsymbol{E}$ the matrix M_N gains more complex appearance

$$M_N = \begin{pmatrix} a & b & c \\ b & a & d \\ c & d & a \end{pmatrix}. \tag{B.1}$$

Diagonalization of M_N leads to principal axes system where the electric vector $\boldsymbol{E}$ does not follow neither of new axes. Thereby, there is no compact expression for transmittance T utilizing the crossed-polarizer technique. The whole procedure of derivation of T is carried out numerically and demonstrated on the representative sample B39UA2.

Figure B.1: Schematic depiction of the experimental set-up framework S_E and crystallographic system S_C. Pockels testing light enters the front side of the block.
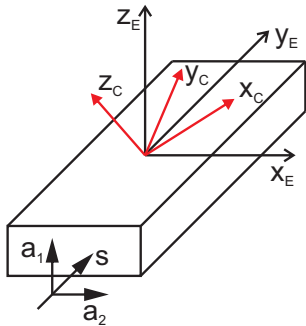
As stated earlier, three different coordinate systems are involved in the problem. Firstly, it is the reference system of the experimental arrangement S_E associated with the crystal block itself where axes are parallel to the crystal edges (Fig. B.1). Secondly, there is a crystallographic system S_C where axes are collinear with edges of a cubic unit cell in the direct space. Thirdly, an important role plays the system S_I represented by principal axes of the index ellipsoid. For succeeding description, expressions in the laboratory system are denoted by subscript E, in the crystallographic system by C and in the system of optical indicatrix by I.

The experimental set-up frame is fixed by the crystal cut. Information about crys-

tallographic system comes from X-ray diffraction measurement using the Laue method. Full orientation of the crystallographic system of specimen B39UA2 with respect to the system of crystal's block is given by three vectors

$$\hat{\boldsymbol{x}}|_{EC} = (0.46869, -0.83871, 0.27731)^{\mathsf{T}}$$
$$\hat{\boldsymbol{y}}|_{EC} = (-0.86105, -0.36378, 0.35505)^{\mathsf{T}} \qquad (\text{B.2})$$
$$\hat{\boldsymbol{z}}|_{EC} = (0.20335, 0.39366, 0.89648)^{\mathsf{T}}$$

where notation $|_{EC}$ means that vector $\hat{\boldsymbol{x}}|_{EC}$ expresses crystallographic x-axis in the laboratory framework. Vectors are columnar and of the unit length.

The closest normal vector with integer Miller indices is $(311)|_C$ and has coordinates $(-0.07469, 0.00268, 0.997204)^{\mathsf{T}}|_E$ and declination $29.5°$ from $(111)|_C$ and $4.3°$ from $(001)|_C$.

An arbitrary vector $\boldsymbol{v} \in \mathbb{R}^3$ symbolized in the crystallographic system as $\boldsymbol{v}|_C = (v_x|_C, v_y|_C, v_z|_C)^{\mathsf{T}}$ has an equivalent representation in the laboratory system using the basal triplet stated above

$$\boldsymbol{v}|_E = (v_x|_E, v_y|_E, v_z|_E)^{\mathsf{T}} = \hat{\boldsymbol{x}}|_{EC}\, v_x|_C + \hat{\boldsymbol{y}}|_{EC}\, v_y|_C + \hat{\boldsymbol{z}}|_{EC}\, v_z|_C\,. \qquad (\text{B.3})$$

The coordinates of $\hat{\boldsymbol{x}}|_{EC}$ has a geometrical meaning of direction cosines between x-axis in S_C and triplet S_E axes. In chapter 4, they were labeled as κ_{ij}. Let us define the transformation matrix $Q_{E\leftarrow C}$ between reference systems S_E and S_C that converts laboratory-framed coordinates into crystallographic coordinates

$$Q_{E\leftarrow C} = (\hat{\boldsymbol{x}}|_{EC}, \hat{\boldsymbol{y}}|_{EC}, \hat{\boldsymbol{z}}|_{EC})\,. \qquad (\text{B.4})$$

Vectors are ordered as columns constituting the matrix. Inverse transform is mediated by $Q_{C\leftarrow E} = [Q_{E\leftarrow C}]^{-1}$ defined as an inverse matrix to $Q_{E\leftarrow C}$. In order to transform the electric vector[1] $\boldsymbol{E}|_E = (E_x, E_y, E_z)^{\mathsf{T}}$ to the crystallographic system, the vector must be multiplied from the left side by $Q_{C\leftarrow E}$

$$\boldsymbol{E}|_C = Q_{C\leftarrow E}\boldsymbol{E}|_E\,. \qquad (\text{B.5})$$

After plugging $\boldsymbol{E}|_C$ to M_N in (4.17), we are prepared for the diagonalization process outputting eigenvalues and conjugated eigenvectors. Eigenvectors specify the system of principal axes S_I. They are mutually perpendicular, independent on the amplitude E of the electric vector $\boldsymbol{E}$, and are represented in the crystallographic system

---

[1]This transform was not necessary for uniaxial case (111) where $\boldsymbol{E}|_C = \frac{1}{3}E(1,1,1)$ was a priori known in the crystallographic system.

$$\hat{\boldsymbol{x}}|_{CI} = (0.718590, 0.210010, 0.6629663)^{\mathsf{T}}$$
$$\hat{\boldsymbol{y}}|_{CI} = (-0.690783, 0.325625, 0.645591)^{\mathsf{T}} \qquad \text{(B.6)}$$
$$\hat{\boldsymbol{z}}|_{CI} = (-0.802981, -0.921881, 0.379062)^{\mathsf{T}}\,.$$

Eigenvalues are interpreted as inverse squares of ellipsoid semi-axes or as principal im-impermittivities η_x, η_y, η_z. They naturally vary with the strength of E-field if the Pockels cell exhibits voltage modulation. Sorting eigenvectors together creates transformation matrix from the indicatrix system to the crystallographic one

$$Q_{C \leftarrow I} = (\hat{\boldsymbol{x}}|_{CI}, \hat{\boldsymbol{y}}|_{CI}, \hat{\boldsymbol{z}}|_{CI})\,. \qquad \text{(B.7)}$$

The composed transformation matrix from the laboratory to the indicatrix system is then product of matrices $Q_{E \leftarrow I} = Q_{E \leftarrow C}\, Q_{C \leftarrow I}$. Backward transform is given by the inverse matrix $Q_{I \leftarrow E} = [Q_{E \leftarrow I}]^{-1}$.

The normal vector of wave propagation $\boldsymbol{s}$ is chosen in the laboratory system (Fig. B.1) that it incidents to the side of the crystal at the right angle $\boldsymbol{s}|_E = (0, 1, 0)^{\mathsf{T}}$. Testing Pockels light has two transversal polarization modes to $\boldsymbol{s}$, vertical $\boldsymbol{a}_1|_E = (0, 0, 1)^{\mathsf{T}}$ and horizontal $\boldsymbol{a}_2|_E = (1, 0, 0)^{\mathsf{T}}$. Their conversion to the indicatrix system is performed as

$$\boldsymbol{s}|_I = Q_{I \leftarrow E}\, \boldsymbol{s}|_E,$$
$$\boldsymbol{a}_1|_I = Q_{I \leftarrow E}\, \boldsymbol{a}_1|_E, \qquad \text{(B.8)}$$
$$\boldsymbol{a}_2|_I = Q_{I \leftarrow E}\, \boldsymbol{a}_2|_E\,.$$

Our further goal is to find out phase velocities for the distinguished polarizations $\boldsymbol{a}_1$, $\boldsymbol{a}_2$. Therefore, we will follow the geometric construction previously depicted in the Fig. 4.1. Mathematically, it signifies to conduct intersection between the ellipsoid and the plane with the unit normal vector $\boldsymbol{s}|_I$. The line of the section is an ellipse and we are interested in the direction vectors and lengths of its semi-axes. Formally, this task is smartly and comprehensively introduced in the paper [26] based upon general properties of a dot product. For improvement of clarity, a dot product of two vectors will be denoted for a while through parenthesis $(\boldsymbol{v}_1, \boldsymbol{v}_2)$.

Optical indicatrix fulfills the equation

$$\eta_x\, x^2|_I + \eta_y\, y^2|_I + \eta_z\, z^2|_I = 1\,. \qquad \text{(B.9)}$$

The intersecting plane containing an arbitrary point Z is described in the parametric form

$$Z = t\, \hat{\boldsymbol{t}}|_I + u\, \hat{\boldsymbol{u}}|_I \qquad \text{(B.10)}$$

where t, u are real parameters and $\hat{\boldsymbol{t}}, \hat{\boldsymbol{u}}$ are unit vectors; within them the plane is spanned. The entire procedure of intersection takes place in the indicatrix framework. Thus extension $|_I$ is temporarily omitted for a simpler notation. A pair of $\boldsymbol{a}_1$, $\boldsymbol{a}_2$ might

serve as $\hat{\boldsymbol{t}}, \hat{\boldsymbol{u}}$ or any other couple as $\hat{\boldsymbol{u}} = \frac{1}{\sqrt{s_x^2+s_y^2}}(-s_y, s_x, 0)^{\mathsf{T}}$, $\hat{\boldsymbol{v}} = \hat{\boldsymbol{u}} \times \boldsymbol{s}$ that makes orthogonal triplet with $\boldsymbol{s}$.

For purely technical intention, let us define auxiliary diagonal matrix

$$D = \operatorname{diag}(\sqrt{\eta_x}, \sqrt{\eta_y}, \sqrt{\eta_z}) \,. \tag{B.11}$$

Vectors $\hat{\boldsymbol{t}}, \hat{\boldsymbol{u}}$ become equally directed with semi-axes of the ellipse of the intersection when they satisfied the criterion

$$(D\hat{\boldsymbol{t}}, D\hat{\boldsymbol{u}}) = \eta_x t_x u_x + \eta_y t_y u_y + \eta_z t_z u_z = 0 \,. \tag{B.12}$$

The length of semi-axes are then easily

$$n_{\boldsymbol{s},1} = \frac{1}{\sqrt{(D\hat{\boldsymbol{t}}, D\hat{\boldsymbol{t}})}}, \; n_{\boldsymbol{s},2} = \frac{1}{\sqrt{(D\hat{\boldsymbol{u}}, D\hat{\boldsymbol{u}})}} \,. \tag{B.13}$$

In order to fulfill requirement (B.12), it is necessary to carry out the rotation of $\hat{\boldsymbol{t}}, \hat{\boldsymbol{u}}$ about angle ω

$$\begin{aligned} \hat{\boldsymbol{t}}' &= \cos\omega \, \hat{\boldsymbol{t}} + \sin\omega \, \hat{\boldsymbol{u}} \,, \\ \hat{\boldsymbol{u}}' &= -\sin\omega \, \hat{\boldsymbol{t}} + \cos\omega \, \hat{\boldsymbol{u}} \,, \end{aligned} \tag{B.14}$$

where angle ω is determined by the formula

$$\omega = \frac{1}{2} \arctan \frac{2(D\hat{\boldsymbol{t}}, D\hat{\boldsymbol{u}})}{(D\hat{\boldsymbol{t}}, D\hat{\boldsymbol{t}}) - (D\hat{\boldsymbol{u}}, D\hat{\boldsymbol{u}})} \,. \tag{B.15}$$

Hence, canonical vibration modes for normal wave vector $\boldsymbol{s}$ are $\boldsymbol{b}_1 = \hat{\boldsymbol{t}}'$ and $\boldsymbol{b}_2 = \hat{\boldsymbol{u}}'$. The phase delay between these two polarizations becomes

$$\Delta\delta_{biax} = \frac{2\pi}{\lambda_0}(n_{\boldsymbol{s},1} - n_{\boldsymbol{s},2})L \,. \tag{B.16}$$

For our particular example we receive

$$\begin{aligned} \hat{\boldsymbol{s}}|_I &= (-0.386073, -0.666257, -0.638004)^{\mathsf{T}} \\ \hat{\boldsymbol{b}}_1|_I &= (0.177783, 0.624921, -0.760176)^{\mathsf{T}} \\ \hat{\boldsymbol{b}}_2|_I &= (0.905174, -0.406910, -0.122816)^{\mathsf{T}} \,. \end{aligned} \tag{B.17}$$

Bearing in mind the Jones formalism established in chapter 5, we will recall orthogonal projectors of the polarizer and analyzer

$$\boldsymbol{P}|_E = \frac{1}{\sqrt{2}}(1, 0, 1)^{\mathsf{T}}, \; \boldsymbol{A}|_E = \frac{1}{\sqrt{2}}(-1, 0, 1)^{\mathsf{T}} \,. \tag{B.18}$$

Nevertheless, Jones vectors are currently made of three components where the second one is redundant and completes dimensions to $\mathbb{R}^3$. Canonical vibrations must be firstly

Figure B.2: Front side projection of laboratory framework with directions of polarizer and analyzer. Jones vectors $\hat{a}_1$, $\hat{a}_2$ are canonical vibration modes for (111) orientation and equally decompose P polarization. Vectors $\hat{b}_1$, $\hat{b}_2$ are new polarization modes for normal wave direction s obtained from biaxial ellipsoid.
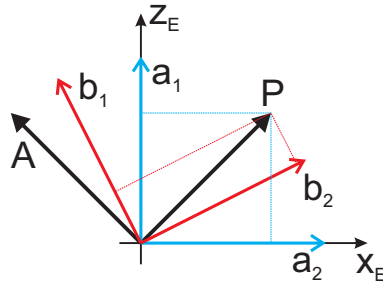
transformed to the laboratory system for further crossed polarizer analysis. It is done as

$$\hat{b}_1|_E = Q_{E \leftarrow I}\hat{b}_1|_I, \quad \hat{b}_2|_E = Q_{E \leftarrow I}\hat{b}_2|_I \tag{B.19}$$

with a result

$$\hat{b}_1|_E = (-0.059458, 0.008777, 0.998192)^{\mathsf{T}}$$
$$\hat{b}_2|_E = (0.997807, -0.000336, 0.066185)^{\mathsf{T}}. \tag{B.20}$$

We see that the second component is not identically null. This numerical error will be discussed later.

Vibration modes $\hat{b}_1|_E$, $\hat{b}_2|_E$ and $\hat{y}|_E = (0, 1, 0)^{\mathsf{T}}$ set the fourth and the last orthogonal reference system S_V that will be marked by subscript[2] V. In fact, the triad $\hat{b}_1|_E$, $\hat{b}_2|_E$, $\hat{y}|_E$ represents new axes $\hat{x}|_{EV}$, $\hat{z}|_{EV}$, $\hat{y}|_{EV}$ of S_V expressed by coordinations of the laboratory system (Fig. B.2).[3] Corresponding transformation matrix $Q_{E \leftarrow V}$ is

$$Q_{E \leftarrow V} = (\hat{x}|_{EV}, \hat{y}|_{EV}, \hat{z}|_{EV}). \tag{B.21}$$

We will operate in the vibration-mode system from the reason that cross-polarizer analysis is trivial as documented in chapter. 4because the initial polarization mode of the Jones vector can be easily decomposed into fundamental modes b_1, b_2. Polarizer and analyzer projectors converted to the system S_V are

$$P|_V = Q_{V \leftarrow E}\, P|_E\,,$$
$$A|_V = Q_{V \leftarrow E}\, A|_E\,, \tag{B.22}$$

where $Q_{V \leftarrow E}$ is inverse to $Q_{E \leftarrow V}$. A scalar product of two vectors expressed in the same framework is an invariant independent upon the choice of a framework. Consequently, it is possible to acquire coordinates of $P|_V$ and $A|_V$ equivalently by more illustrative

---

[2]Modes $\hat{b}_1|_E$, $\hat{b}_2|_E$ are not exactly perpendicular to $(0, 1, 0)^{\mathsf{T}}|_E$ as they should have been. Discrepancy comes from a measurement uncertainty of X-ray diffraction.

[3]The vibration-mode system is related to the indicatrix system through the rotation around axis s_I about angle ω.

cosine projections

$$
\begin{aligned}
\boldsymbol{P}|_V &= ((\hat{\boldsymbol{x}}|_{EV}, \boldsymbol{P}|_E), 0, (\hat{\boldsymbol{z}}|_{EV}, \boldsymbol{P}|_E))^\mathsf{T}, \\
\boldsymbol{A}|_V &= ((\hat{\boldsymbol{x}}|_{EV}, \boldsymbol{A}|_E), 0, (\hat{\boldsymbol{z}}|_{EV}, \boldsymbol{A}|_E))^\mathsf{T} \\
&= ((\hat{\boldsymbol{z}}|_{EV}, \boldsymbol{P}|_E), 0, -(\hat{\boldsymbol{x}}|_{EV}, \boldsymbol{P}|_E))^\mathsf{T}
\end{aligned}
\tag{B.23}
$$

because $\boldsymbol{P} \perp \boldsymbol{A}$; numerically

$$
\begin{aligned}
\boldsymbol{P}|_V &= (-0.665733, 0, 0.753584)^\mathsf{T}, \\
\boldsymbol{A}|_V &= (-0.753584, 0, -0.665733)^\mathsf{T}.
\end{aligned}
\tag{B.24}
$$

The Jones vector of the Pockels testing light after passing polarizer becomes oriented in the same way $\boldsymbol{J}_P|_V = \boldsymbol{P}|_V$. Within the propagation of the wave through the crystal, transversal vibrations get mutually de-synchronized by the phase shift $\Delta\delta_{biax}$ from (B.16)

$$
\boldsymbol{J}_{cell}|_V = (J_{Px}|_V \exp(-i\Delta\delta_{biax}), 0, J_{Pz}|_V)^\mathsf{T},
\tag{B.25}
$$

Projecting $\boldsymbol{J}_{cell}|_V$ of transmitted light to the direction of analyzer $\boldsymbol{A}|_V$, we obtain final polarization

$$
\boldsymbol{J}_A|_V = (\boldsymbol{J}_{cell}|_V, \boldsymbol{A}|_V)\boldsymbol{A}|_V.
\tag{B.26}
$$

Overall transmittance is a ratio of parallel versus crossed intensity

$$
\mathsf{T}_{biax} = \frac{I_\perp}{I_\parallel} = \left[(\hat{\boldsymbol{b}}_1, \boldsymbol{P})(\hat{\boldsymbol{b}}_2, \boldsymbol{P}) \right]^2_E \times |1 - \exp i\Delta\delta_{biax}|^2 = \Upsilon \, |1 - \exp i\Delta\delta_{biax}|^2
\tag{B.27}
$$

where $\boldsymbol{b}_1$, $\boldsymbol{b}_2$ were substituted for $\hat{\boldsymbol{x}}|_{EV}$, $\hat{\boldsymbol{z}}|_{EV}$. The magnitude E of the E-field does not seem to affect eigenvectors received by the diagonalization procedure as well in (4.19) that is why the prefactor Υ remains constant. Moreover, we might assume a proportional relationship between the phase shift and the E-field $\Delta\delta_{biax} = \alpha_{biax}E$ analogically to (5.2) and (5.7) resulting in

$$
\mathsf{T}_{biax} = \Upsilon \, \sin^2(\alpha_{biax}E) = \Upsilon \, \sin^2\left(\frac{\pi}{2} \frac{E}{E_{\pi/2}} \right).
\tag{B.28}
$$

Factor Υ only modifies the interval of transmittance from $(0,1)$ to $(0,\Upsilon)$ and changes the value of overturn E-field $E_{\pi/2}$. Inverting expression (B.28), a formula for unreconnected E-field is obtained

$$
E = \frac{1}{\alpha_{biax}} \arcsin\sqrt{\frac{\mathsf{T}}{\Upsilon}} = \frac{2}{\pi} E_{\pi/2} \arcsin\sqrt{\frac{\mathsf{T}}{\Upsilon}}.
\tag{B.29}
$$

There are two parameters involved in the reconstruction of the electric intensity - correction factor Υ and biaxial version of $E_{\pi/2, biax}$.

Simulation predicts $E_{\pi/2} = 450\,\mathrm{V/mm}$ and $\Upsilon = 0.5$ for specification of the sample

B39UA2 $L = 7\,\mathrm{mm}$, $r_{41} = 5.5 \times 10^{-15}\,\mathrm{V/mm}$, $n_0 = 2.8$, $\lambda_0 = 980\,\mathrm{nm}$. If we compare this result with experimental values estimated from plot in Fig. 5.6 where $\Upsilon = 0.9$ and $E_{\pi/2} = 1250\,\mathrm{V/mm}$, we conclude concordance of the same order of magnitude.

The Pockels effect changes the refraction index at the order 10^{-5}-10^{-6}, corresponding undisturbed optical impermittivity CdTe is $\eta_0 = 1/2.8^2 = 0.128$ and the effect starts at its fifth order. Uncertainty in Pockels coefficient r_{41} of 10% modulates Υ approximately about 0.15, similarly as a 1 mm error in the crystal length does.

Besides this, uncertainty in determination of crystallographic directions raised from X-ray diffraction measurement is estimated as 3% that influence mainly the E-field direction $\boldsymbol{E}|_C$. Reflection spots from the Laue method are not sharp enough due to a mosaic essence of the crystal. Diffraction pattern has multiple close located peaks that merge together to the one outspread peak. The crystallographic basis introduced in (B.2) is not perfectly orthogonal. Diffraction also revealed that lattice constants are not equalled for all three dimensions. The Pockels effect changes the refraction index at the order 10^{-5}-10^{-6}, the corresponding undisturbed optical impermittivity CdTe is $\eta_0 = 1/2.8^2 = 0.128$ and the effect starts at its fifth order.

Analytical formulas for fundamental zinc-blende orientation (100), (011) are provided in the pioneering paper [27].

# C. Current for diode-like arrangement of metal-semiconductor contacts

In the upcoming paragraphs we will sketch out a theoretical model explaining current-voltage dependency of the general detector structure metal-semiconductor-metal [35]. In the chapter 6.4 it was considered that injection of electrons from the metal to the semiconductor is crucially responsible for the charge transport and the shape of IV curves. However, each carrier passes the M-S interface twice - at the arrival to the semiconductor and at the departure from it. The electron exiting the detector medium must overcome a barrier for upward-curved bands to get from the conduction band to the Fermi level of the metal. The hole leaving the crystal has an equivalent trouble for bands curved down. The conductivity of an intrinsic semiconductor has an ambivalent character, hence electron as well as hole currents must be taken into account together.

The process of carrier transport can be decomposed qualitatively to the elemental steps depicted in the substitutional scheme Fig. C.1. Interfaces M $\rightarrow$ S has a character of the rectifying emitter, whereas the junction S $\rightarrow$ M plays the role of a rectifying collector. A solitary branch is composed of two schottky diodes and a resistor R_B representing the intrinsic crystal bulk. Two parallel branches constitute separated conductive channels for electrons and holes. A homo-type structure of the detector (Au-Au, In-In) forms forward and reversed branches. For instance, a gold-gold couple is in the forward direction for holes and in the reverse for electrons. A hetero-type pair of electrodes (In-Au) arranges two branches with couples of Schottky diodes (collector-emitter) facing mutually back-to-back or head-to-head.

The bias in a single branch is split to the voltage drop at the bulk $U_B = R_B I$ and to the residual parts U_{d1} and U_{d2} where $U = U_{d1} + U_B + U_{d2}$ and I denotes the current flowing through the branch. If a diode is connected in the forward or reversed mode, it stands again the voltage U_d or to $-U_d$, respectively. Voltage drop at the ideal diode[1] is

---

[1]Let us consider the ideality factor to be 1.

Figure C.1: Model of Schottky diodes substituting metal-semiconductor interfaces. Inner resistor represents the bulk of the semi-insulting CdTe. The upper branch is a channel for electrons, holes flow through the bottom branch. An emitter E injects carriers from the metal to the semiconductor. A collector C drains carriers from the semiconductor to the metal. Their behaviour is rectifying. A gold electrode injects holes and blocks electrons. An indium electrode injects electrons and blocks holes.
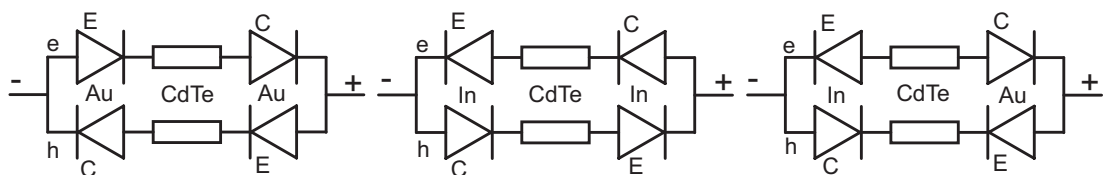
$u_d = \ln\left(\frac{I}{I_S} + 1\right)$ where the contracted notation of the reduced voltage $u_d = qU_d/k_BT$ was recalled. For the identically oriented diodes we obtains the condition for fixed bias u as

$$u - u_B = 2\ln\left(\frac{I}{I_{S1}} + 1\right) \tag{C.1}$$

and for the back-to-back arrangement

$$u - u_B = \ln\left(\frac{I}{I_{S1}} + 1\right) - \ln\left(-\frac{I}{I_{S2}} + 1\right) \tag{C.2}$$

where u_B denotes $\frac{q}{k_BT}R_BI$. Hereafter, the left hand side $u - u_B$ is denominated by u_L. The solution for the parallel diodes orientation is trivial

$$I = I_{S1}(e^{u_L/2} - 1). \tag{C.3}$$

Voltage u_L is equally divided between both diodes.

For back-to-back diodes, the situation is completed but still straightforward. After simple manipulation the expression (C.2) gets the form

$$e^{u_L} = \frac{I/I_{S1} + 1}{-I/I_{S2} + 1} \tag{C.4}$$

and further effort leads to the IV curve

$$I(u_L) = \frac{2I_{S1}I_{S2}\sinh(u_L/2)}{I_{S1}\exp(u_L/2) + I_{S2}\exp(-u_L/2)}. \tag{C.5}$$

The growth in current of the first diode is compensated by the cut-off of the second diode producing asymptotic plateau regions for $u_L \to \pm\infty$ with y-values I_{S1}, I_{S2} (Fig. C.2). If the difference in the rectifying property is eminent, for instance $I_{S1} \gg I_{S2}$, then the impact of the second diode on the net current could be neglected in the interval of $u_L \in (0, \infty)$ and we obtain a curve that is well approximated by the classical diode law (6.22) $I(u_L) \approx -I_{S2}[\exp(u_L) - 1]$.

Generally, a serial connection of a diode and resistor is analysed through the geometrical construction of a load line that represents linear dependency of the resistor $U_L = U - R_BI$. The intersection of the diode IV with the load line determines an operating point when u_L matches with the diode voltage u_d and an identical current I flows through both components. The IV curve of the whole branch is the set of pair values - bias U and current I. In other words, it means that the intercept of the load line is swept across the first and the third quadrant while the current I at the operating point is recorded. Total current is the sum of the currents coming from the electron and hole branches. The specific trend (convex, concave shape) of the IV curves depends upon saturation currents I_{S1}, I_{S2} and temperature [35].

Figure C.2: *Left* Method of a load line construction. *Right* Current-voltage curve of two diodes arranged back to back.
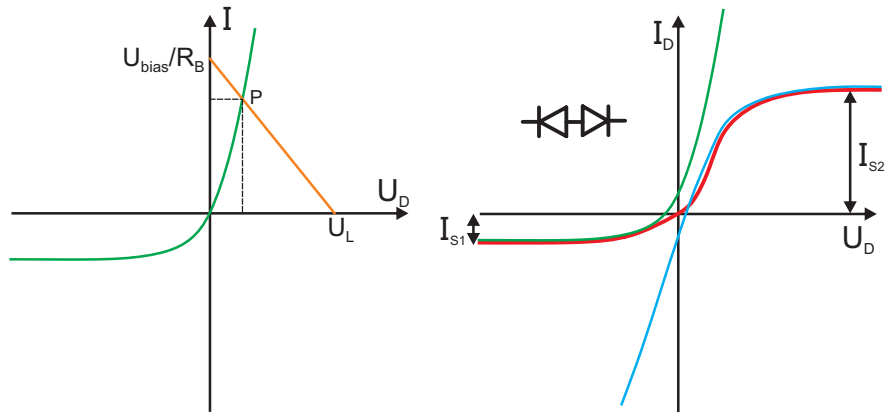
Table 7.1: Properties of CdTe, miscellaneous sources.

Intrinsic gap energy (T=0 K, 300K)	1.60(2-7) eV, 1.45-1.5 eV
Lattice constant	6.482 Å
Atom density	$1.47 \times 10^{22}\,\mathrm{cm}^{-3}$
Mass density	$6.20\,\mathrm{g/cm}^3$ (T =300 K)
Melting point	1092 °C
Mechanical hardness	$56\,\mathrm{kg/mm}^2$
Electron affinity	5.05 eV
Work function	5.1-5.4 eV
Static dielectric constant	10.2
Refractive index (T = 300 K)	$2.84 - 2.87\,(\lambda_0 = 1\mu\mathrm{m})$
Pockels coefficient	$5.5 - 6.8 \times 10^{-12}\,\mathrm{V/cm}\,(\lambda_0 = 1\mu\mathrm{m})$
Thermo-optic coefficient [24] $\mathrm{d}n/\mathrm{d}t$	$1.47 \times 10^{-4}\,\mathrm{K}^{-1}$
Heat capacity c_p	0.210 J/(g.K) ($T = 300\,\mathrm{K}$)
Thermal conductivity	$6.3\,\mathrm{W/(m.K)}(T = 300\,\mathrm{K})$
Linear thermal expansion coefficient	$5.0 \times 10^{-6}\,\mathrm{K}^{-1}$
Electron effective density of states in conduction band	$7.5 \times 10^{17}\,\mathrm{cm}^{-3}$
Hole effective density of states in valence band	$2 \times 10^{19}\,\mathrm{cm}^{-3}$
Effective electron mass	$0.096\,m_0$
Effective hole mass	$0.83\,m_0$
Mobility of electrons	$1000 - 1100\,\mathrm{cm}^2/(\mathrm{V.s})$.
Mobility of holes	$100 - 110\,\mathrm{cm}^2/(\mathrm{V.s})$
Mean electron lifetime	$3 \times 10^{-6}\,\mathrm{s}$
Mean hole lifetime	$2 \times 10^{-6}\,\mathrm{s}$
Electron $\mu\tau$	$3.3 \times 10^{-3}\,\mathrm{cm}^2/\mathrm{V}$
Hole $\mu\tau$	$2 \times 10^{-4}\,\mathrm{cm}^2/\mathrm{V}$
Diffusion coefficient of electrons	$25 - 28\,\mathrm{cm}^2/\mathrm{s}$
Diffusion coefficient of holes	$2.5\,\mathrm{cm}^2/\mathrm{s}$
Electron thermal velocity	$3.5 \times 10^5\,\mathrm{m/s}$ ($T = 300\,\mathrm{K}$)
Hole thermal velocity	$1.8 \times 10^5\,\mathrm{m/s}$ ($T = 300\,\mathrm{K}$)

Table 7.2: List of specimens involved to this work and their specifications. Composition CdTe:In, light n-type, resistivity $3 - 5 \times 10^9\,\Omega\mathrm{cm}$, $\mu\tau \approx 10^{-3}\,\mathrm{cm}^2/\mathrm{V}$ [22].

ID	Dimensions(mm)	Orientation	Contact metals	Method/Purpose
B39B5	$5 \times 5 \times 1.65$	(422)	Au/In	IR scanning
B39K4	$8 \times 5 \times 1.5$	(311)	none	Luminescence
B39UA2	$8 \times 5 \times 1.5$	(311)	Au(In)/Au(In)	Pockels
B39UB1	$8 \times 5 \times 1.5$	?	Au/Au	Photo p. 4
B39UB3	$8 \times 5 \times 1.5$	?	Au/Au	Voltage Dep.

Bibliography

[1] TOUŠEK J.: *Polovodičvé prvky III*, Karolinum, Univerzita Karlova, Praha, 1993, ISBN 80-7066-750-6

[2] FUNAKI Minoru, ANDO Yukio, TACHIBA Akira: *Development of CdTe detectors in Acrorad*, Acrorad Co., Ltd., e-mail: funaki@acrorad.jp

[3] FRANC J., DĚDIČ V., GRILL R., HAKL M.: *Flux-dependent electric field changes in semi-insulting CdZnTe*, Journal of Applied Physics D: Applied Physics, **46** (2013) 235306, doi:10.1088/0022-3727/46/23/235306

[4] Acrorad Co., Ltd.: `http://www.acrorad.co.jp/us`

[5] WALD F. V.: *Application of CdTe - A review*, Mobil Tyco Solar Energy Corporation, published by Revue de Physique Apliquée

[6] GRILL R., BELAS E., FRANC J., et al: *Polarization study of detect structure of CdTe radiation detectors*, Transactions on Nuclear Science, Vol. 58, No.6, (2011)

[7] FONTHAL G., TIRADO-MEJIA L., et al: *Temperature dependence of the band gap energy of crystalline CdTe*, Journal of Physics and Chemistry of Solids 61, 579–583, (2000)

[8] VARSHNI Y. P.: *Temperature dependence of the energy gap in semiconductors*, Physica 34, 149 (1967)

[9] CHELIKOWSKYL J. R., COHEN M. L.: *Nonlocal pseudopotential calculations for the electronic structure of eleven diamond and zinc-blende semiconductors*, Phys. Rev. B 14, 556 (1976)

[10] ŠEDIVÝ Lukáš: *Diffusion of native defects and impurities in CdTe/CdZnTe*, Diploma Thesis, Institute of Physics, Charles University, Prague, 2011, in czech

[11] IVANITSKA V. G., MORAVEC P., FRANC J., et. al.: *Chemical Polishing of CdTe and CdZnTe in iodine-methanol etching solutions*, Journal of Electronic Materials, Vol. 40, No. 8, (2011), doi: 10.1007/s11664-011-1649-2

[12] FRANC J., KUBÁT J., GRILL R., et. al.: *Evaluation of the quality of semi-insulting CdTe for radiation detectors by measurement of lux-ampere characteristics*, Nuclear Instruments and Methods in Physics Research, A 633(2011), S97-S99

[13] PROCHÁZKA Jan: *Photoluminescence of CdTe crystals*, Disertation Thesis, Institute of Physics, Charles University, Prague, 2012, in czech

[14] PELANT Ivan, VALENTA Jan: *Luminescence Spectroscopy of Semiconductors*, Oxford Press, New York, 2012, ISBN 978-0-19-958833-6

[15] PELANT Ivan, VALENTA Jan: *Luminescenční spektrografie I- Objemové krystalické polovodiče*, Academia, 2006, ISBN: 80-200-1447-0

[16] HORODYSKÝ P., HLÍDEK P.: *Free-exciton absorption in bulk CdTe: temperature dependence*, Physica Status Solidi (b) 243, No. 2, 494–501, (2006), doi: 10.1002/pssb.200541402

[17] ZÁZVORKA J., FRANC J., HLÍDEK P.: *Photoluminescence spectroscopy of semi-insulting CdZnTe and its correlation to resistivity and photoconductivity*, Journal of Luminescence, 143, 382-387 (2013)

[18] HORODYSKÝ Petr: *Optical properties of $Cd_{1-x}Zn_xTe$* , Disertation Thesis, Institute of Physics, Charles University, Prague, 2006

[19] SCHOCKLEY W., READ W. T.: *Statistics of the recombination of holes and electrons*, Physical Review, Vol. 87, No. 5, (1952)

[20] BUGÁR Marek: *Dynamics of structural defects in CdTe-based semiconductors*, Disertation Thesis, Institute of Physics, Charles University, Prague, 2011

[21] FARELLA I., MONTAGNA G., COLA A.: *Study of instability phenomena in CdTe diode-like detectors*, Transactions on Nuclear Science, Vol. 56, No. 4, (2009)

[22] DĚDIČ Václav: *Influence of Deep Levels on Charge Transport in CdTe*, Disertation Thesis, Institute of Physics, Charles University, Prague, 2014

[23] NARASIMHAMURTY, T. S.: *Photoelastic and Electro-Optic Properties of Crystals*, Plenum Press, New York , 1981, ISBN 978-1-4757-0027-5

[24] WEBER Marvin, et al.: *Handbook of optical materials*, CRC Press, 2003, ISBN 0-8493-3512-4

[25] PALIK Edward: *Handbook of Optical Constants of Solids*, Academic Press, Boston, 1985

[26] KLEIN Peter Paul: *On the Ellipsoid and Plane Intersection Equation*, Applied Mathematics 3, 1634-1640, (2012)

[27] NAMBA Susumu: *Electro-optical effect of Zincblende*, Journal of the Optical Society of America, Vol. 51, No. 1, (1961)

[28] DĚDIČ V., FRANC J., ELHADIDY H.: *Study of deep levels in high resistivity CdZnTe by discharge current measurement*, 14-th international workshop on radiation imaging detectors, IOP publishing

[29] Capacitor fringing calculator : `http://chemandy.com/calculators/rectangular-capacitor-calculator.htm`

[30] COLA A., FARELLA I.: *The polarization mechanism in CdTe Schottky detectors*, Applied Physics Letters **94**, 102113, (2009); doi: 10.1063/1.3099051

[31] TOYAMA Hiroyuki, HIGA Akira, et al. : *Analysis of polarization phenomena and deep acceptor in CdTe radiation detector*, Nuclear Scince Symposium Conference, 2006

[32] CROWELL C. R., SZE S. M.: *Current transport in metal-semiconductor barriers*, Solid State Electronics, Vol. 9, p. 1035-1048, Pergamon Press, (1966)

[33] FRANC J., DĚDIČ V., SELLIN P. J.: *Radiation induced control of electric field in Au/CdTe/In structures*, Applied Physics Letters, **98**, 232115, (2011)

[34] SACHTLER W. M. H., HOLSCHER A. A.: *The work function of gold*, Surface Science, **5**, 221-229, (1966)

[35] ELHADIDY H., SIKULA J., FRANC J.: *Symmetrical current–voltage characteristic of a metal–semiconductor–metal structure of Schottky contacts and parameter retrieval of a CdTe structure*, Semiconductor Science & Technology, **27**, 015006, (2012), doi:10.1088/0268-1242/27/1/015006

[36] X-Ray mass attenuation coefficient for CdTe: `http://physics.nist.gov/PhysRefData/XrayMassCoef/ComTab/telluride.html`

[37] COLA A., FARELLA I.: *Electric Field and Current Transport Mechanisms in Schottky CdTe X-ray Detectors under Perturbing Optical Radiation*, Sensors 13, 9414-9434, (2013), doi:10.3390/s130709414

[38] PREKAS G., SELLIN P. J.: *Investigation of the internal electric field distribution under in situ x-ray irradiation and under low temperature conditions by the means of the Pockels effect*, J. Phys. D: Appl. Phys. **43**, 085102 (6pp), (2010), doi:10.1088/0022-3727/43/8/085102

[39] SATO Goro, FUKUYAMA Taro, et al: *Study of polarization phenomena in Schottky CdTe diodes using infrared light illumination*, Nuclear Instruments and Methods in Physics Research A, **652**, p. 149-152, (2011)